12-14-2015

In Situ IR Spectroscopic Investigation of Noble Metal Catalysts Related to the Reduction of Automotive Exhaust Emissions

Zhiyong Wang
University of South Carolina - Columbia

IN SITU IR SPECTROSCOPIC INVESTIGATION OF NOBLE METAL CATALYSTS RELATED TO THE REDUCTION OF AUTOMOTIVE EXHAUST EMISSIONS

by

Zhiyong Wang

Bachelor of Chemical Engineering
Dalian University of Technology, 2010

Submitted in Partial Fulfillment of the Requirements

For the Degree of Doctor of Philosophy in

Chemical Engineering

College of Engineering and Computing

University of South Carolina

2015

Accepted by:

Jochen Lauterbach, Major Professor

Jason Hattrick-Simpers, Committee Member

John Weidner, Committee Member

Kevin Huang, Committee Member

Lacy Ford, Senior Vice Provost and Dean of Graduate Studies

DEDICATION

To my mom Fengbao Pang,

without whose love and support this work would not have been possible.

ACKNOWLEDGEMENTS

There are a lot of people who need to be recognized for their contributions to this work. First and foremost, I would like to thank both of my advisors, Dr. Jochen Lauterbach and Dr. Jason Hattrick-Simpers, without whose guidance and support this would be impossible. They have always gotten me back to the right track when I was distracted and given me encouragement when I was on the right path. I feel so lucky that I could work with two experts in different areas, one in catalysis area with excellent physics background and one in material science area. From both of them I learned how to pursue high-quality scientific research and how to become an independent scientist. I also want to express my special thanks to Dr. Jochen Lauterbach for his invitation to his house every Christmas, where I could enjoy delicious food and hang out with so many friends.

I would like to thank the other two members of my thesis committee, Dr. Kevin Huang and Dr. John Weidner. I know both of you are really busy, and your comments and thoughtful suggestions during my research are truly appreciated.

I need to especially thank my college Dr. Cun Wen, who always inspired me with different questions during my research. His depth of knowledge and dedication in science admire me a lot. He is also a good friend who can share your good times and bad times. I believe in the near future, a rising star will appear in catalysis community.

I want to thank my college Chao Wang for sharing his ideas, in both research and personal life. I want to thank Dr. Erdem Sasmaz for his suggestions and discussions about

my research. I would also like to thank other SAGE members, including Dr. Chris Metting, Michael Kai Mayeda, Jonathan Kenneth Bunn, and Kate Mingle, etc. They are not only good partners to have in research, but also good friends to enjoy life with.

I would also like to thank all of my friends during my stay in Columbia, including Qiang Gao, Long Cai, Meng Guo, Jingjie Wu, Fan Wu, Shuai Tan, Xiaojing Sun, Tingting Yang, Jingyi Huo, Hong Liu, Weijian Diao, Yunya Zhang, Tianyuan Xie, Yiling Dai, Yating Mao, Qiuli Liu, Zhuonan Song, Yiying Wang, Lei Wang, Song Gao, Jingsheng Zhang, Xiao Li, etc. Thanks to all of you for making my life in Columbia colorful and memorable.

Finally, and most importantly, I want to thank my family, especially my mom, who always support me and give me the strength to face every challenge I meet in my life. I could not have made through this without your love and supports.

ABSTRACT

The reduction of automotive exhaust emissions has been one of the hottest topics in catalysis community since 1970s. Thanks to the development of three-way catalysts, main auto-exhaust pollutants, such as carbon monoxide, nitrogen oxides and unburned hydrocarbons, can be removed simultaneously. Nowadays, diesel engines and lean-engines become more and more popular due to their high fuel-efficiency and low CO_2 emissions. Unfortunately, conventional three-way catalysts are not effective at reducing the NO_x emissions from these engines due to the excess oxygen in the exhaust stream. Platinum catalysts were found to be highly active for selective NO reduction with hydrocarbons in excess oxygen and has good thermal stability and sulfur resistance. However, discrepancies still exist in the reaction mechanism of NO reduction with hydrocarbons on platinum catalysts. In this thesis, fundamental surface science studies were performed with in situ IR spectroscopic techniques combined with mass spectrometry, aiming to gain some new insight into the catalysis related to auto-exhaust emission control. Three catalysts system were explored, including model catalysts Pt(100) single crystal and Ru/Al_2O_3 thin film supported nanoparticles, and practical catalyst Pt/Al_2O_3 with various particle sizes.

On Pt(100) single crystal surface, CO adsorption was investigated from ultra-high vacuum condition to elevated pressures with mass spectrometry and polarization

modulation infrared reflection absorption spectroscopy (PM-IRAS). Different adsorption behaviors were observed for CO adsorption on Pt(100) at different pressures. Heating the sample at high pressure (>2 Torr) could cause carbon island formation on the surface, based on the IR spectra and temperature programmed desorption results. It was demonstrated that PM-IRAS is highly effective at detecting surface species under reaction conditions and can be applied to bridge the "pressure gap" between surface science and industrial catalysis. To bridge the "materials gap", model thin film supported catalysts are desired and were prepared via wet deposition method in this work.

Thin film of aluminum oxide supported Ru nanoparticles were synthesized and characterized with different techniques. Thermal oxidation of aluminum substrate could form γ-alumina thin film, and it was suitable for IR spectroscopic studies. Magnetron sputter deposition was also attempted for epitaxial alumina thin film synthesis and more research would be required to get ideal results. Colloidal method was successfully applied to synthesize Ru nanoparticle of different sizes with polyvinylpyrrolidone as the protective agent. After ethanol cleaning, extracted Ru nanoparticles were deposited onto alumina support followed by UVO cleaning. X-ray photoelectron spectroscopy characterization indicated that Ru nanoparticles were deposited successfully onto the support with about 0.67% weight loading. More tests are to be carried out on the model supported catalyst before it is loaded into the vacuum chamber for systematic studies.

On Pt/Al_2O_3 catalysts with different particle sizes, selective reduction of NO with propene were investigated at various reaction conditions using diffuse reflectance infrared fourier transform spectroscopy combined with mass spectrometry. It was found that higher NO conversions with much higher TOFs were obtained on the catalysts with

larger Pt particles, on which a relative higher NCO/CN ratio was observed in the meantime. From the systematic studies on Pt catalysts with different pretreatments, it was proposed that better activity on catalysts with larger Pt particles were attributed to the more abundant terrace sites rather than corner or edge sites on larger Pt particles. These terrace sites have better activity for NO dissociation, thus can enhance the formation of reactive intermediates such as isocyanate during the reaction. In addition, it was found that the activation of the hydrocarbon species by oxygen was a crucial step toward the formation of the isocyanate species, thus could influence the catalyst activity for NO reduction.

TABLE OF CONTENTS

LIST OF TABLES

LIST OF FIGURES

CHAPTER 1

Introduction

1.1 Reduction of automotive exhaust emissions

Catalysis related to the reduction of automotive exhaust emissions has been one of the most interested and developed areas in science community since 1970s when the United States Air Act was passed due to the increasing public concern of the deteriorating air quality. As a result, the three-way catalyst (TWC) technology was developed and implemented successfully in 1979 to reduce the exhaust emissions and is still found in almost all modern catalytic converters [1]. As its name implies, the TWC can remove the three main pollutants in the exhaust simultaneously, carbon monoxide (CO), nitric oxide (NO) and unburned hydrocarbons (HC), by using a catalyst composed of platinum (Pt), palladium (Pd) and rhodium (Rh) metals supported on alumina (Al_2O_3) support. Current TWCs typically consist of a thin layer of a porous material coated on the channel walls of a ceramic (usually cordierite) honeycomb-shaped body with the channels axially orientated in the direction of flow of the exhaust gas [1]. The porous material is composed of high-surface-area γ-Al_2O_3 (70-80%) and other metal oxides, such as cerium oxide (CeO_2), barium oxide (BaO) and nickel oxide (NiO). The noble metals (Pt, Pd and Rh) only consists a small fraction (1-2%) of the "washcoat" [1].

The principle reactions occurring on the TWCs are:

Oxidation: $CO+O_2 \rightarrow CO_2$

$HC + O_2 \rightarrow CO_2 + H_2O$

Reduction: $2\ CO + 2\ NO \rightarrow 2\ CO_2 + N_2$

$HC + NO \rightarrow CO_2 + H_2O + N_2$

Whereas Pt and Pd are good for the oxidation reactions, and Rh is more efficient in NO_x elimination than other metals due to its superior activity in NO dissociation [1-3].

As the need of transportation vehicles increases in the developed and developing countries, more stringent regulations are designed to control the auto-exhaust emissions. According to the Tier 3 program designed to reduce air pollution from passenger cars and trucks by the U.S. Environmental Protection Agency (EPA), the estimated emission reduction of CO is 2% (278,879 tons) by 2018 and 24% (3,458,041 tons) by 2030, while the targeted reduction of NO_x emission is 10% (264,369 tons) by 2018, and 25% (328,509 tons) by 2030. As environmental regulations get more and more stringent, better technologies that can reduce automotive exhaust emissions more efficiently become urgent. In addition, the increasing concerns about CO_2 emission which can cause global climate change have stimulated the interest of improving the fuel efficiency of internal combustion engines. Diesel engines or lean-burn engines have become more and more popular due to their high fuel-efficiency and low CO_2 emissions. However, the exhaust from these engines consists of large amount of oxygen (5-10%), and conventional TWCs become ineffective at NO_x reduction since the reducing agents (H_2, CO and HC) present in the exhaust stream are rapidly oxidized by the excess O_2.

Several promising strategies for NO_x reduction under oxidizing conditions have been explored in the past decades, including NO_x decomposition, NO_x storage-reduction (NSR), and selective catalytic reduction (SCR) of NO_x [4-6]. Specifically, due to its great performance for NO_x abatement in excess oxygen, supported Pt catalyst has received considerable attention in the catalysis community [2, 5-11]. Significant efforts have been put into the investigation of HC-SCR reaction on Pt catalysts with various oxide supports, different Pt loading and dispersion, and different promoters [7-21]. As a result of these efforts, two distinct reaction mechanisms have been proposed for NO reduction by propene in excess oxygen on alumina-supported Pt catalysts: (1) NO decomposition and subsequent oxygen removal by the hydrocarbon reductant [7-11]; (2) NO reduction via the formation of an intermediate isocyanate surface species [18-21]. In the first mechanism, it was proposed that oxygen could compete for the reduced platinum sites with NO and the reductant was in charge of cleaning off the oxygen atoms on platinum surface. On the other hand, in the second mechanism, it was believed that the oxygen was to activate the hydrocabons which could promote the formation of intermediate isocyanate species. Despite the discrepancy of reaction mechanisms existing in literature, the size effect of Pt particles on the HC-SCR of NOx is still unclear due to the lack of in situ spectroscopic investigations. For example, how does the surface species change with the particle size? What are the most important intermediate species? How does the particle size influence the reactive intermediate species and the catalyst activity under reaction conditions? It is clear that more work needs to be carried out to understand the mechanism of NO decomposition and reduction under various operating conditions.

In this thesis, in situ IR spectroscopic techniques were utilized to investigate the HC-SCR reactions on Pt catalysts of different sizes, aiming to provide better understanding of the surface chemistry. Besides the studies on supported Pt catalysts, fundamental surface chemistry investigations were also carried out in a high-pressure compatible ultra-high vacuum (UHV) system over model catalysts, such as Pt(100) single crystal and thin film supported ruthenium (Ru) nanoparticles. The advantage of these surface science studies is that, on model catalysts with well-defined structures, the elemental steps of the interested reactions can be understood at a molecular level with controlled reaction conditions. A customized polarization-modulation infrared reflection absorption spectroscopy (PM-IRAS) system combined with a mass spectrometry (MS) were utilized for this purpose and more explanation of the system will be given later.

1.2 Pressure gap and materials gap

One of the goals in heterogeneous catalysis research is to understand the reaction mechanisms at a molecular level, providing guidance for better technical catalysts design. However, modern industrial catalysts are typically active metal particles dispersed on high surface area porous material, which are not suitable for molecular-level characterizations by conventional microscopic or spectroscopic techniques. To overcome this difficulty, model catalysts with well-defined structures (usually metal single crystals) have been introduced and investigated under controlled reaction conditions. Especially, with the development of UHV technology in the later 1960s, more surface science techniques are available for detailed characterization of these model catalysts. The

mechanism of some catalytic reactions has been elucidated form UHV experiments, namely the oxidation of carbon monoxide (CO) [22], and the synthesis of ammonia (NH_3) [23], etc. However, it has been argued that whether the mechanism working in UHV conditions on single crystal surfaces can extend to practical catalysis condition with supported catalysts.

This so called "pressure gap" has been reported for different reactions [24-27]. For example, for the oxidation of CO over the transition metals of Pt, Pd, Rh, Ru, and iridium (Ir), Ru catalyst displays less activity than the other metals under UHV conditions, but it becomes the most active one at high pressures. This reactivity change was found due to the formation of a thin layer of Ru oxide, which could only form at elevated pressures but not under UHV conditions [25]. Besides the "pressure gap", there is also the "materials gap" originating from the fact that metal single crystals cannot account for two important aspects of practical catalysts: the metal particle size and the support effect. It has been reported in different reactions that the particle size affects both the reactivity and the selectivity of a catalyst. For instance, during ammonia synthesis on Ru catalysts, the catalyst with 5 nm nanoparticles has the highest reactivity due to its highest B-5 sites concentration on the surface, and the reactivity decrease as Ru particles get larger or smaller [28]. In addition, catalyst support is not always just a mechanical support, but also can change the reactivity of the catalyst. The support can modify the electronic properties of the metal particles, or provide oxygen storage, or cause strong metal support interaction [29, 30]. It has been reported that CeO_2, which has high lattice oxygen storage and accessibility of lattice oxygen, can significantly enhance the Pd/CeO_2 catalyst for low temperature CO oxidation [29, 30].

To bridge the "pressure gap" and "materials gap", reactions are required to be carried out from UHV to elevated pressure conditions on model supported catalysts, which are very similar to those industrial catalysts. Thus high-pressure compatible UHV systems equipped with surface sensitive characterization techniques (functional at elevated pressures) are necessary for systematic reaction studies. To achieve this purpose, a lot of efforts have been put into designing UHV compatible high pressure reaction cell, which is capable of carrying out surface cleaning and analysis, as well as kinetic measurements at elevated pressures [31-36]. On the other hand, synthesis and reaction studies of model catalysts ranging from single crystal to model supported nanoparticles for different reaction systems have also showed significant progress[37-49].

In the past decades, several in-situ high-pressure-capable surface characterization tools have been developed successfully, e.g. high pressure X-ray diffraction (XRD) (~5 bar) [50]; high pressure X-ray photoemission spectroscopy (XPS) (~100 mbar) [32]; atom-resolved environmental transmission electron microscopy (ETEM) (~20 mbar) [51, 52]; and high pressure scanning tunneling microscopy (HP-STM) (~10^3 Torr) [34, 53]. In addition to these instruments, two other surface sensitive techniques, namely sum frequency generation (SFG) vibrational spectroscopy [26, 53-55] and PM-IRAS [55-61] can be applied from UHV to atmospheric pressures. Compared with SFG, PM-IRAS technique has several advantages. First, PM-IRAS has wider frequency range (800–4000 cm^{-1} vs. >1600 cm^{-1}) allowing additional detection of deformation modes and fingerprinting signatures. Second, PM-IRAS has a shorter acquisition time (several minutes vs. 20-30 minutes) and better resolution (<1 cm^{-1} vs. ~5 cm^{-1}), thus a better signal-to-noise (S/N) ratio. Regardless of the operation difficulty, SFG also needs

significant maintenance. So it is quite beneficial to perform in situ spectroscopic studies with PM-IRAS measurement from UHV to elevated pressure conditions. The “pressure gap” and “materials gap” could be bridged simultaneously with the application of PM-IRAS and model catalysts, including metal single crystals and model thin film supported nanoparticles.

1.3 Thesis objective and scope

In this thesis, CO adsorption and dissociation on Pt (100) surface were performed from UHV to elevated pressure conditions using PM-IRAS, trying to reveal the pressure effect on CO dissociation on Pt surface. It was proven that PM-IRAS is a powerful technique that can be used to bridge the “pressure gap”. To bridge the “materials gap”, different preparation methods were attempted for the synthesis of model thin film supported Ru nanoparticle catalysts. In addition, the particle size effect of Pt catalysts for the HC-SCR of NO was investigated with in situ diffuse reflectance infrared fourier transform spectroscopy (DRIFTS) combined with MS.

Briefly, the materials and methods as well as the characterization and detection techniques used in this thesis were introduced in Chapter 2. In chapter 3, CO adsorption on Pt(100) was investigated in detail with PM-IRAS system from UHV to elevated pressures. Even though this system has been investigated a lot at UHV condition in the past, it still provided very valuable insights into CO dissociation at high pressures on Pt(100) surface, specifically the carbon island formation at high pressures and high temperatures. Besides the investigations on metal single crystal surfaces, spectroscopic

studies on model supported nanoparticle catalysts were also attempted. In chapter 4, the synthesis and characterization of model supported catalysts Ru/Al_2O_3 were described, including the alumina oxide film making, Ru nanoparticle synthesis and deposition of Ru nanoparticles on the oxide support. It was demonstrated that the wet deposition of Ru nanoparticles onto oxide thin film support could be applied to make model catalysts that are suitable for surface science studies. In chapter 5, selective catalytic reduction of NO with hydrocarbons was investigated on Pt catalysts with different particle sizes to resolve the discrepancies existing in literature and some valuable insight in the reaction mechanism was obtained. Finally, the main conclusions of this thesis were summarized and the outlook for the future work was made in chapter 6.

CHAPTER 2

Materials and Methods

In this chapter, the catalysts investigated in this thesis will be introduced first: including metal single crystals Pt(100), model thin film supported nanoparticles catalyst Ru/Al_2O_3 (the detailed synthesis procedure for model catalyst Ru/Al_2O_3 will be covered in Chapter 5), and powder catalysts Pt/Al_2O_3. Secondly, different catalyst characterization methods are presented, such as chemisorption, transmission electron microscopy (TEM), X-ray diffraction (XRD), Raman spectroscopy, scanning electron microscopy (SEM) and X-ray photoelectron microscopy (XPS). At the end, detailed introduction of the reaction studies techniques will be given, including mass spectrometry (MS), polarization-modulation infrared reflection absorption spectroscopy (PM-IRAS) and diffuse reflectance infrared fourier-transform spectroscopy (DRIFTS).

2.1 Catalysts preparation

2.1.1 Metal single crystal sample Pt(100)

The Pt(100) single crystal sample has been used in our group for different projects before [62, 63]. The thickness of the sample is 1 mm and the diameter is about 8 mm. Typically, Pt single crystal sample was cleaned via Ar^+ sputtering and high temperature annealing followed by oxidation in O_2 environment. In this work, the Pt(100) single

crystal surface was cleaned multiple times before each experiment through the following procedures: 1) annealing at 1273 K under vacuum for 3 min, 2) sputtering in 6 x 10^{-6} Torr Ar at 5 keV for 10 min, 3) annealing at 1273 K under vacuum for 3 min, 4) oxidizing at 773 K in 10^{-6} Torr O_2 for 10 min. This procedure was repeated until satisfactory surface reactivity for the CO oxidation reaction was confirmed. The reactivity experiments were performed at 473 K and 10^{-6} Torr with a ratio of CO/O_2=1/9, and the production of CO_2 was monitored using the MS. Repeatable vibrational band with certain exposures after cleaning was also applied to confirm the sample cleanliness.

2.1.2 Thin film supported Ru/Al_2O_3 model catalyst

In this work, model supported catalyst Ru/Al_2O_3 was composed of Ru nanoparticles deposited on Al_2O_3 thin film. Different from conventional synthesis of model catalysts in UHV chamber via physical vapor deposition (PVD) or chemical vapor deposition (CVD), Both Ru nanoparticles of different sizes and Al_2O_3 thin films were made outside the experimental vacuum chamber and pretreated before loaded into the reaction system. The Ru nanoparticles were synthesized via colloidal method in ethylene glycol (EG) with poly-vinylpyrrolidone (PVP) as the stabilizing agent. After synthesis, the nanoparticles were cleaned with ethanol or acetone, centrifuged and dispersed in acetone for use. The size and morphology of Ru nanoparticles were characterized with TEM. The Al_2O_3 thin films were made with two different methods: magnetron sputter deposition and thermal oxidation of Al substrate. The sputter deposition of Al_2O_3 was performed in an AJA sputter system located in lab 119B in Horizon 1 building at the

University of South Carolina, while thermal oxidation of Al substrate was carried out in a tube furnace in lab 130 in Horizon 1 building. The crystal structure and surface morphology of Al_2O_3 thin films were characterized with XRD, Raman spectroscopy, TEM and SEM/EDX. Detailed procedures of Ru nanoparticle synthesis and Al_2O_3 thin film making will be introduced in Chapter 5. After depositing Ru nanoparticles onto Al_2O_3 thin film support, the model catalysts were pretreated in a ultra-violet Ozone cleaner to remove possible organic residuals remaining on the surface. The catalysts were then characterized with XPS for Ru concentration on the surface. Prior to load the sample into the PM-IRAS vacuum system, preliminary test were performed outside the vacuum chamber in a DRIFTS instrument with CO adsorption experiment.

2.1.3 Supported Pt/Al_2O_3 catalyst

The Pt/Al_2O_3 catalysts were prepared with wetness impregnation method, which is probably the most widely accepted method in order to synthesize supported catalysts. Generally, it is composed of mixing the porous support material with a solution (referred to as the precursor solution) that contains the metal ion or ions to be deposited on the support surface. The key aspect of the incipient wetness method is that the volume of the precursor solution matches the pore volume of the support material. Capillary action draws the solution into the pores of the support and the metal ions are constrained inside. The liquid is then evaporated from the pores by heating above the boiling point of the liquid solution. Besides the metal ions, the precursor solution usually contains counter ions (such as nitrate, acetate, or chloride) that must be removed from the catalyst. These

counter ions removal is typically achieved by calcination in air at a high temperature, usually higher than any temperature the catalyst will be exposed to under normal operating conditions. Thus, the calcination step also acts to stabilize the catalyst and minimize any changes, such as sintering, that may occur under operating conditions.

In this work, The Pt/Al_2O_3 catalysts were prepared by incipient wetness impregnation of the γ-Al_2O_3 support (Alfa Aesar) with an aqueous solution of tetraammineplatinum dichloride monohydrate $Pt(NH_3)_4Cl_2 \cdot H_2O$ (Alfa Aesar). Following the wetness impregnation, the samples were dried at 120 °C for 12 h and then calcined at temperature above 500 °C at various heating rates or different length of calcination time to obtain a wide range of particle size.

2.2 Catalysts characterization techniques

2.2.1 Chemisorption

Chemisorption is a practical technique widely used to determine the exposed surface area of the active metal component in the catalyst. It is based on the concept that certain probe molecules (e.g. CO or H_2) will bind strongly and preferentially to the active metal in the sample. The process of chemisorption experiment is typically performed by dosing a known quantity of a probe gas to the sample. The amount of probe gas taken up by the sample is proportional to the surface area of the exposed metal. Based on the chemisorption data and the metal loading content, the metal dispersion can be obtained.

In this research, the Micromeritics Auto Chem II 2920 was used to measure the dispersion of the Pt/Al_2O_3 catalysts. Generally, a catalyst sample of known mass is loaded into a U-shaped quartz tube of known volume which is then attached to the apparatus. The sample then must be pretreated to remove any residual adsorbed molecules (such as water vapor) and to clean and reduce the surface of the active metal. This is typically performed by heating the sample in vacuum and then exposing it to several alternating cycles of O_2 and H_2. At last, the sample is cooled to room temperature in vacuum and then exposed to pulsed probe gas (typically CO or H_2) in a carrier gas. During the pulse gas dosing process, the thermal conductivity of the gas was continuously monitored by a thermal conductivity detector (TCD). The probe gas in the first pulse may be completely adsorbed on catalysts and the detector only detects the carrier gas. After several pulses when the catalyst is saturated, the TCD signal will get stable indicating the chemisorption process is finished. The metal dispersion and exposed metal surface area are then calculated based on the gas uptake data.

2.2.2 Transmission electron microscopy (TEM)

TEM was applied to characterize the size and morphology of Ru nanoparticles and Pt/Al_2O_3 catalysts, as well as the crystal phase of Al_2O_3 film studied in this work. As its name implies, in TEM a beam of high-energy electrons is focused onto a thin sample and transmitted through it. As the beam interacts with the sample, some electrons are deflected by the nuclei and electron clouds of the atoms within the sample while other electrons are transmitted straight through the sample. The transmitted electrons are then

diverged and focused onto a fluorescent screen or a digital camera for image observation. Typically, the actual resolution of a conventional TEM is about 1.0 nm, while high resolution TEM can get down to atomic resolution.

In this research, the TEM images and diffraction patterns were obtained on a Hitachi H8000 transmission electron microscope, located in the Electron Microscopy Center at the University of South Carolina. In this instrument, a LaB_6 single crystal was used as the electron emission source in the electron gun. When a high voltage is applied (typically ~100-200 kV) the gun will, given sufficient current, begin to emit electrons either by thermionic or field electron emission into the vacuum. This extraction is usually aided by the use of a Wehnelt cylinder. Once extracted, the condenser lenses of the TEM will allow for the formation of the electron probe to the desired size and location for later interaction with the sample. After the beam passes through the sample, it is diverged by the objective electromagnetic lens onto a CCD camera where the image of the sample or the diffraction pattern is viewed directly. As a requirement for most electron microscope system, the column containing the electron beam must be kept at high vacuum ($< 10^{-6}$ Torr) to minimize interference and scattering from the environment.

The TEM instrument can be operated in different modes for different applications. The most common mode of operation is the bright field imaging mode. In this mode, thicker regions of the sample, or regions with higher atomic density will appear dark, while regions with no sample or with lower atomic density will appear bright-hence the term “bright field”. It can also be operated at diffraction mode, where the electron beam undergoes Bragg scattering and disperses electrons into discrete locations in the back focal plane. By adjusting the magnetic lenses such that the back focal plane of the lens

rather than the imaging plane is placed on the imaging apparatus, a diffraction pattern can be generated. Typically only parts of the sample that are causing the electrons to scatter to the selected reflections will end up projected onto the imaging apparatus. This produces an image that consists of a pattern of dots in the case of a single crystal, or a series of rings in the case of a polycrystalline or amorphous solid material. For this work, the size and morphology of Ru nanoparticles were checked with "bright field" mode, and the crystal structure of Al_2O_3 film was characterized with diffraction mode.

TEM samples are typically prepared on 3.0 mm diameter grids made of copper, nickel, gold or molybdenum. The grids are typically coated with a very thin supporting layer of carbon, which is fairly transparent to the electron beam due to its low atomic density. In this research, 400-mesh copper grids coated with thin carbon film (Pacific Grid Tech) were used. In addition, the girds were only handled with specialty antimagnetic stainless steel tweezers (Ted Pella, Inc.). Ru nanoparticles were rinsed and dispersed in acetone or ethanol solvent before dropping to the TEM grids. Usually two drops of the suspension were added to TEM grids and dried in air for an hour, after which time the sample was ready for use in the microscope. Similar procedure also worked well for Al_2O_3 film sample except the rinse step was performed with water droplet after the sample was dropped onto the TEM grids, which is to avoid severe film breaking during the rinse. The powder catalysts Pt/Al_2O_3 were characterized in a high resolution TEM (JEOL 2100 F) with dark field mode to obtain high quality images.

2.2.3 X-ray diffraction (XRD)

The crystal structure of Al_2O_3 thin films made from sputter deposition was characterized by XRD. After the discovery of X-rays by German physicist Rontgen in 1895, it has enabled scientists to probe crystalline structure at atomic level. X-ray diffraction has become one of the most important characterization techniques in solid chemistry and material science. In general, based on the elastic scattering of X-rays from the electron clouds of the individual atoms in materials, a diffraction pattern containing the information about the size and shape of the unit cell in crystalline material being analyzed will be produced. Bragg diffraction model was often introduced to obtain an intuitive understanding of XRD. In this model, a given reflection is associated with a set of evenly spaced sheets running through the crystal, usually passing through the centers of the atoms of the crystal lattice. The orientation of a particular set of sheets is identified by its three Miller indices (h, k, l), where each index denotes a plane orthogonal to a direction (h, k, l) in the basis of the reciprocal lattice vectors. Assuming X-rays are scattered specularly (mirror-like) from each plane, the scattered X-rays from adjacent planes will combine constructively (constructive interference) when the angle θ between the plane and the incident X-ray results in a path-length difference equal to an integer multiple n of the X-ray wavelength λ: $2d*\sin\theta = n\lambda$ (Bragg's Law, where d is the spacing between two parallel planes). For different materials, the constructive interferences will take place on different angles with different intensities, and the final diffraction pattern, usually recorded as the X-ray intensity (counts or counts/second) versus the angle 2θ, serves as a "fingerprint" of different materials. To confirm whether a desired material is successfully made, usually a search/match analysis is performed using the JCPDS data

base. In specific, experimental XRD patterns are compared to reference patterns to determine what phases are present, and a small amount of mismatch in peak position and intensity is acceptable experimental error. In other words, the experimental data should contain all major peaks listed in the reference pattern, while the minor reference peaks could be lost in the background noise. For a new material synthesized, one needs to do peak indexing to get more information about the material, such as the unit cell, lattice parameters and symmetry. Typically, the higher the symmetry of the crystal material, the easier it is to index the pattern and the fewer peaks there are in the pattern. Two full pattern fitting methods are often used: the Rietveld method and the Le-Bail and Pawley fitting methods. The Rietveld method uses fundamental calculations from crystal structure models to produce the calculated diffraction pattern, while the Le-Bail and Pawley fitting methods use unit cell models combined with empirical fitting of peak intensities. More information of XRD configuration and pattern analysis could be found in the textbook [64].

In this research, the XRD patterns were taken on a Rigaku Miniflex XRD instrument with a Cu/K-alpha1 X-ray source at wavelength 1.54059 Angstroms, located in lab 129 in Horizon 1 building at the University of South Carolina. Typically, the sample was scanned from 20 to 80 degree at a scan speed of 0.5 degree/min. For samples deposited on Si(100) wafer, an aluminum filter was used to reduce the signal intensity to avoid possible damage to the detector. After measurements, the patterns were compared with standard gamma-Al_2O_3 or alpha-Al_2O_3 reference patterns.

2.2.4 Raman spectroscopy

The structure of Al_2O_3 thin films was also characterized with Raman spectroscopy, which is based on inelastic scattering (or Raman scattering) of a monochromatic light, usually a laser in in the visible, near infrared, or near ultraviolet range. Typically, a sample is illuminated with a laser beam. Electromagnetic radiation from the illuminated spot is collected with a lens and sent through a monochromator. Elastic scattered radiation at the wavelength corresponding to the laser line (Rayleigh scattering) is filtered out, while the rest of the collected light is dispersed onto a detector by either a notch filter or a band pass filter. Unlike elastic Rayleigh scattering which is used to determine the shape and weight of macromolecules, Raman scattering is inelastic scattering with much lower intensity: approximately 1 in 10^7 scattered photons. The scattered photons either gain or lose some of their energy during the inelastic scattering process, corresponding to anti-stocks and stocks scattering (stocks scattering is the main part). The energy difference is equal to the energy of a transition the molecule undergoes in response to the collision with the photon, thus providing the electronic, rotational or vibrational information of the material. A Raman spectrum is usually presented with Raman scattering intensity as a function of the Raman shift (due to the energy change). In contrast to Raman scattering, sometimes, fluorescence or luminescence emission can take place when the energy of the excitation photon gets close to the transition energy between two electronic states. When fluorescence is generated, it is often much more intense than Raman scattering, hiding Raman features. Proper choose of the laser source can avoid the strong fluorescence effect on the material of interest due to the intrinsic difference between Raman scattering and fluorescence emission. The Raman spectrum generally

does not depend on the laser excitation, since it measures the energy gain or loss of the incident laser. However, fluorescence is dependent on the laser source. If the excitation photon does not provide sufficient energy to the molecule, the required transition to generate fluorescence will not take place.

In this research, the Raman spectra of Al_2O_3 thin films was taken in a Raman spectrometer in Dr. Williams's group lab 3B19 in Swearingen building at the University of South Carolina. This instrument has a HeNe laser with wavelength of 632.8 nm. The fluorescence effect is strong for sapphire with HeNe laser and this phenomenon was applied to check if there was alpha-Al_2O_3 in the sample.

2.2.5 Scanning electron microscopy (SEM)

The surface topography and chemical composition of materials can be characterized with SEM in nano scale. Basically, it scans the sample with a beam of high-energy electrons, which interact with the atoms that make up the sample, then pass through the electromagnetic lens and reach the detector to produce an image or a spectrum that contains information about the sample's surface topography, composition, and other properties. There are different types of signals in SEM: secondary electrons (SE), back-scattered electrons (BSE), Auger electrons, X-rays photons, transmitted electrons and specimen current. The secondary electrons, defined as electrons with energy less than 50 eV, are created by inelastic electron scattering in the material. These electrons mainly come from the surface of the material (5 nm metals, 50 nm insulators). In the most common or standard detection mode, called secondary electron imaging or

SEI, the SEM instrument can produce very high-resolution images of a sample surface, revealing the surface details with a resolution less than 1 nm in size. With the highly narrow electron beam, SEM micrographs can get a large depth of field yielding a characteristic three-dimensional appearance useful for understanding the surface structure of a sample. Back-scattered electrons are beam electrons that are reflected from the sample by elastic scattering, and they are often used in analytical SEM along with the spectra made from the characteristic X-rays. Because the intensity of the BSE signal is strongly related to the atomic number (Z) of the specimen, BSE images can provide information about the distribution of different elements in the sample. Besides, characteristic X-rays are also emitted when the electron beam removes an inner shell electron from the sample, causing a higher energy electron to fill the shell and release energy. These characteristic X-rays can be used to identify the composition and concentration of elements in the sample, and this technique is usually known as Energy-dispersive X-ray spectroscopy (EDX or EDS).

In this research, the surface topography and elemental composition of Al_2O_3 thin films and Ru/Al_2O_3 model catalysts were characterized on a Zeiss Ultraplus Thermal Field Emission Scanning Electron Microscope, located in the Electron Microscopy Center at the University of South Carolina. This SEM instrument has the capability for EDS and EBSD with different detectors: In-lens detector, EsB detector, AsB detector, Everhart-Thornley detector, and a CCD camera with infrared illumination. It is equipped with a Nabity e-beam lithography system, as well as a charge compensator for non-conductive specimen imaging. The sample was typically hold on an aluminum stub using vacuum-clean conductive tape and positioned on the sample holder which could hold 9

samples at once. To avoid electron charge on the sample surface, low electron energy beam was usually used for imaging measurement. Sometimes conductive tape or gold coating was also applied to mitigate the electron charge effect.

2.2.6 X-ray photoelectron spectroscopy (XPS)

X-ray photoelectron spectroscopy (XPS), also known as electron spectroscopy for chemical analysis (ESCA), has been widely used to investigate the elemental composition empirical formula, chemical state and electronic state of the elements existing in a material. The modern application of XPS owes much of its development to Kai Siegbahn and his co-workers at the University of Uppsala, Sweden. Kai Siegbahn was awarded the 1981 Nobel Prize for his contributions. Typically, in XPS measurements, a material is irradiated by a beam of X-rays and the kinetic energies and number of electrons escaped from the material are measured. Based on photoelectric effect, when a material absorb a photon with an energy in excess of the binding energy (E_B) of the electron inside the material, a photoelectron will be emitted, having an energy equal to the energy difference between the initial states and final states of the atom. Since deep core electrons do not participate in bonding, the kinetic energy (E_K) measured after the photoemission process is unique for different element. To a first approximation, the energy of core electrons is independent of the environment of the atom. Thus, XPS is useful for elemental analysis of a sample. The relationship between the photon energy, hv, and the electron binding energy, E_B, is given by Einstein equation:

$$E_B=hv-E_K-\phi$$

In the equation above, the binding energy E_B is referred to the vacuum level, and ϕ is the work function dependent on the spectrometer and the material. The work function is an adjustable instrumental correction factor that accounts for the few eV of kinetic energy given up by the photoelectron as it is absorbed by the detector. It is a constant that rarely needs to be adjusted in practice. For calibration purpose, usually a clean gold sample with a binding energy of 84.0 eV (Au $4f_{7/2}$) is used, due to the easy preparation and maintenance of clean surfaces of gold. Frequently, the X-ray source used in XPS instrument is a dual anode X-ray gun (Al Kα hν= 1486.7 eV, Mg Kα hν= 1253.6 eV). For conductive samples, chemical equilibrium established by flow of charge (electrons) between analyzer and sample; Fermi level is equalized and becomes the reference, and XPS is independent of the sample work function. However, for nonconductive samples, chemical equilibrium cannot be established since charge cannot flow between analyzer and sample; Fermi level is not equalized and becomes an invalid reference, and the work function of the sample needs to be considered. Positively charged surface will absorb electrons to reduce positive charge, this process will keep going on until the surface potential is equal to electron potential so that low energy electron will bounce back, at this point the whole surface will reach a uniform potential. Once surface is overcompensated for the charge in the XPS measurement, it will become negatively charged, which causes the BE value to shift to low BE side. Usually, low energy electrons are used to neutralize the surface charge. For Al_2O_3 samples, since it is nonconductive, this charge compensation was performed before the measurement.

As mentioned, the binding energy of an electron is equal to the energy difference between the initial and final states of the atom, approximately. The real case is, during the

electron excitation and relaxation process, the electron will interact with other neighboring atoms, causing a binding energy shift in the final spectrum. There are different effects that affect the binding energy, including initial state effects resulting in a chemical shift, and final states effects causing satellite features. The initial states effect are caused by chemical bonding, which influences the electronic configuration in and around the atom, thus the energetic shift caused by initial states is known as a chemical shift. The chemical shift mainly depends on the oxidation state of the atom. In general, the binding energy increases (kinetic energy decreases) as the oxidation state increases. The final state effects include extra-atomic relaxation, multiplet splitting, shake-up, and shake-off events. Shake-up event is the most common effect observed, and usually the satellite peaks due to shake-up transition lies on the high binding energy side of a direct photoemission transition.

In this research, the XPS spectra of Ru/Al_2O_3 model catalysts were taken on a Kratos Axis Ultra DLD instrument equipped with a monochromated Al Kα X-ray source and a hemispherical analyzer, located in lab 3B15 in Swearingen Building at the University of South Carolina. Usually, a survey scan was performed for general composition characterization in a relatively short time, normally less than 30 min. If necessary, a detailed scan with high resolution was further carried out in a specific binding energy region, normally 20 eV range, for the oxidation state identification of a known element.

2.3 Reaction studies techniques

2.3.1 Mass spectrometry

In this research, the gas phase concentration of reactants and products was measured using MS. The operation principle of MS is based on the fact that charged particles can be separated and identified by their mass-to-charge ratio. Typically, the sample is first ionized, these ions are then passed through the mass filter, and the separated ion species are detected by a Faraday cup or electron multiplier. Due to the short mean free path of ions analyzed in MS, high vacuum ($< 10^{-6}$ Torr) is required for successful operation.

A mass spectrometer consists of three components: an ion source, a mass analyzer, and a detector. The ion source is in charge of sample ionizations in MS, and there are different ionization methods such as electron ionization, chemical ionization, electrospray ionization and matrix-assisted laser desorption/ionization, depending on the form and nature of the sample. For gas sample ionization, the most popular method, also the one used in this research, is electron ionization. In this method, a filament (e.g. oxide coated Iridium) is heated to emit electrons. When the gas is introduced to the ionization chamber, the electrons begin to excite the molecules of the sample, resulting in fragmentation and ionization of the sample molecules. The ionized particles are then accelerated by an anode into the mass analyzer. Sometimes, the ionization chamber also contains a grid or cage to modify the path of the emitted electrons, in order to maximize the number of collisions with the sample molecules. It is not uncommon to see different ionization efficiency with different configuration from system to system.

Mass analyzer can also be performed by several different methods, including sector field mass analyzer, time-of-flight analyzer, quadrupole mass filter and ion traps. The most commonly used analyzer, also the one used in this research, is the quadrupole mass analyzer. The name of quadrupole is derived from the fact that an electric field is created between four opposing electric poles. In quadrupole mass analyzer, there are four cylindrical electrodes arranged in a square pattern. Each opposing rod pair is connected together electrically, and a radio frequency (RF) voltage is applied between one pair of rods and the other. A direct current (DC) voltage is then superimposed on the RF voltage. When charged particles pass through the longitudinal axis in the center of the quadrupole, the path of an ion passing though the filter is deflected by the potential field created by the rods. The combination of the RF and DC signal causes the path of particle to oscillate. Thus only ions of a certain mass-to-charge ratio will reach the detector, while other ions have unstable trajectories and will collide with the rods.

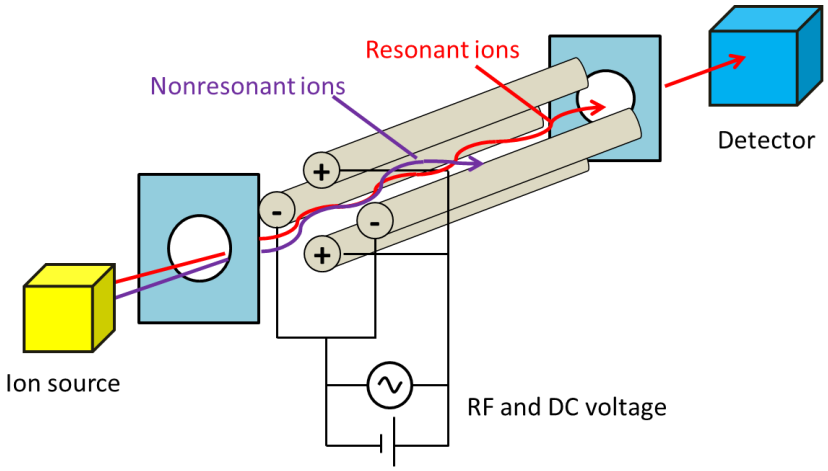

Figure 2.1: Representative diagram of a quadrupole mass spectrometer

Detector used in mass spectrometer varies from Faraday cup, electron multiplier, negative-ion detector, to channel electron multiplier array and electro-optical ion

detection, etc. The most common and simplest detector for mass spectrometer is Faraday cup. In a Faraday cup detector, positive ions impinging on the collector, usually an electrode in a Faraday cage, are neutralized by electron drawn from ground after passage through a high-ohmic resistor. An ion current generated from this neutralization process will be measured and amplified before sending to the recorder. The current is directly proportional to the number of ions and number of charges per ion. In other words, a Faraday cup is a charge detector. The response of the Faraday cup is independent of the energy, the mass or the chemical nature of the ions. It is simple, inexpensive and reliable. The principle disadvantage is that it has a relatively long time constant in the amplification system due to the use of a high-ohmic resistor. Another popular type of detector is electron multiplier based on the secondary electron emission effect of dynodes. Typically, the electron multiplier is horn-shaped, and the inside is covered with a special material (e.g. copper-beryllium dynode) that emits a secondary electron when struck by a single ion. Each time the ions collide with the wall, additional secondary electrons are expelled, resulting in amplification. Electron multiplier detector has a fast response with high operational gain of 10^5-10^8. However, it does have some drawbacks: (1) the gain is dependent on usage and operation conditions; (2) it exhibits some mass discrimination due to the dynode dependence on the velocity, mass and charge of the incident particles; and (c) it could easily get saturated and overloaded when the output current exceeds 10^{-8} amps. Usually, electron multiplier are operated at high vacuum conditions ($<10^{-6}$ Torr) with fast scan speed and low noise level; while Faraday cup can be operated at low vacuum conditions ($<10^{-4}$ Torr) with acceptable response time.

In this research, a quadrupole mass spectrometer (Hiden, Model HAL 201 RC) was applied to analyze the gas products during reaction. Both Faraday cup and electron multiplier detectors were available for different analyzing conditions. The MS was interfaced to a PC (OS Windows 7) through a serial cable connection that allowed data to be collected in MASsoft 7 Professional software. There are four scan modes available for different purposes: profile mode, bar mode, multiple ion detection (MID) mode, and leak detection mode. Profile mode was usually used for electron multiplier signal calibration once a while, and leak detection mode was often used to check possible leaks of the vacuum chamber. Bar mode and MID mode were used most of the time in this research. In bar mode, the concentration of all possible mass fragments was obtained. It could identify new species in the sample quickly and provide guidance for further monitoring. It was also often operated after backeout of the vacuum chamber to see if the baking was satisfying. More commonly, the MS was operated in MID mode with electron multiplier detector, where the concentrations of several assigned masses (or more precisely, mass-to-charge ratios) were all monitored as a function of time. It is important to point out that, in the interface unit of this MS, there were two auxiliary connection ports available for external signal detection in addition to standard MS signals measurements. This allowed continuous monitor of the sample temperature in real time via the external communication with the temperature control unit. Temperature programmed desorption/oxidation/reduction experiments could be performed very efficiently, and real-time temperature reading made the data analysis more accurate and straightforward. The resolution of this MS was 1 amu, and the range was 1-200 amu. During experiments, the pressure was set to $1x10^{-7}$ Torr by fine adjustment of the leak valve which was attached

close to the MS in the bottom chamber. The primary disadvantage of using MS to monitor gas phase concentrations is the potential overlap of different species. For example both CO and N_2 have an atomic weight of 28 amu. Thus, the chemical identity of certain species cannot be known unambiguously using this technique. Fortunately, most of the gases analyzed in this research did not have the same atomic weight.

2.3.2 Polarization Modulation Infrared Reflection Absorption Spectroscopy (PM-IRAS)

Another major technique used in this research is PM-IRAS, which can detect vibrational bands of the molecules adsorbed on catalysts surface from UHV condition to elevated pressures, thus provides the detailed information of surface species during experiments, such as adsorption sites, geometries and possible intermediates involved in the reaction. To understand PM-IRAS technique, a fundamental understanding of Fourier transform infrared spectroscopy (FTIR) would be necessary.

2.3.2.1 Fourier Transform Infrared Spectroscopy (FTIR)

The principle of infrared spectroscopy is based on the vibrational excitation of molecules by absorption of infrared light. In general, infrared radiation is passed through a sample, and some of the infrared radiation is absorbed by the sample while the rest is passed through (transmitted). The resulting spectrum represents the molecular absorption in characteristic wavenumber regions, creating a fingerprint of the sample. No two unique molecular structures produce the same infrared spectrum, which makes infrared

spectroscopy a widely used material characterization technique in different areas, such as environmental, food and drugs, energy and fuels.

Infrared spectroscopy is typically based on a Michelson interferometer, as shown in Figure 2.2. The interferometer consists of a beam splitter, a fixed mirror, and a moving mirror that translates back and forth, very precisely. The beam splitter is made of a special material (usually thin film of germanium on KBr substrate) that transmits half of the radiation striking it and reflects the other half. Radiation from the source strikes the beam splitter and separates into two beams with the same intensity. One beam is transmitted through the beam splitter to the fixed mirror and the second is reflected off the beam splitter to the moving mirror. The fixed and moving mirrors reflect the radiation back to the beam splitter. Again, half of this reflected radiation is transmitted and half is reflected at the beam splitter, resulting in one beam passing to the detector and the second back to the source. The intensity of the beam reaching the detector is the combination of the beams from the fixed mirror and the moving mirror. When the moving mirror moves a distance of X, the beam reflected back from the moving mirror will travels a longer distance of 2X than the beam reflected back from the fixed mirror. This path difference is known as the retardation δ, or optical path difference (OPD). When the retardation is zero, the two beams reaching the detector will have the same phase, thus constructive interference. The beam intensity detected will be at its maximum. When the retardation becomes $\delta=\lambda/2$, the two beams will be 180º out of phase, thus destructive interference and minimum intensity. For an infinitely narrow line source, the beam intensity will change as a function of the OPD, resulting in a cosine wave-like interferogram. The spectrum can be generated from the inteferogram based on Fourier transform calculation.

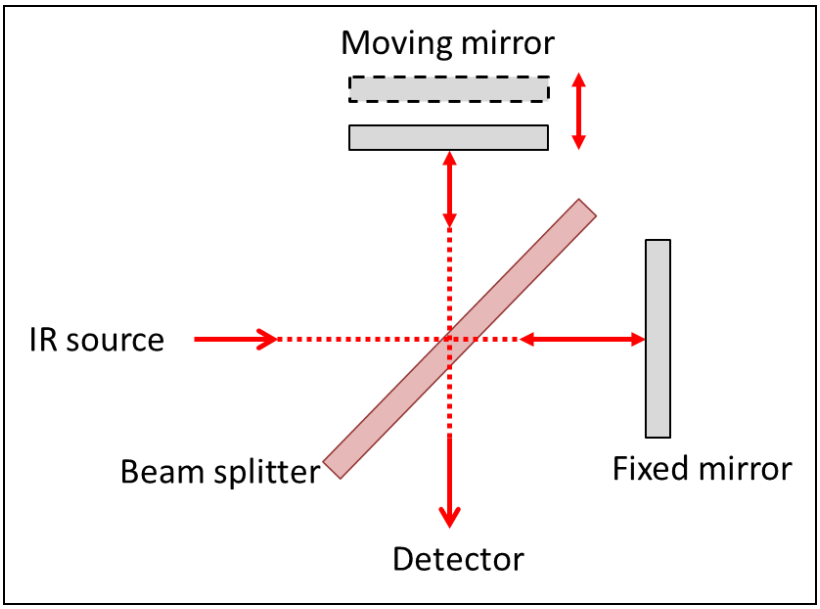

Figure 2.2: Representative diagram of a Michelson Interferometer

In practice, modern FTIR instrument will have a continuous source. Thus the final interferogram will be the summation of all cosine waves of all frequencies in the source. A typically interferogram from the continuous source is shown in Figure 2.3 (a), where the intensity reaches its maximum at zero retardation with all cosine waves in phase, and drops quickly as we move from the centerburst to either direction due to the destructive inferences of all cosine waves. After fourier-transform, the corresponding IR spectra could be obtained as shown in Figure 2.3 (b). Theoretically, a single scan would be enough to generate an interferogram, but the noise level would be really high. Typically, multiple scans would be performed during measurements to gain a good signal-to-noise ratio (SNR). There is an empirical equation for the SNR:

$$SNR=\sqrt{t}*\Delta v*E$$

Where t is the scanning time, Δv is the resolution chosen for the scan, and E is the energy throughput. Typically, higher number of scans (the longer the scan time) or lower resolution is used to obtain satisfactory SNR. Due to the ease of use, high sensitivity and excellent linearity, deuterated triglycine sulfate (DTGS) detector is commonly used in FTIR instrument. When sample measurements must be made at high speed or when IR throughput is low, the highly sensitive mercury cadmium telluride (MCT) detector provides the ability to scan faster than a DTGS detector while maintaining a constant IR response. More introduction of FTIR could be found in literature [65-67].

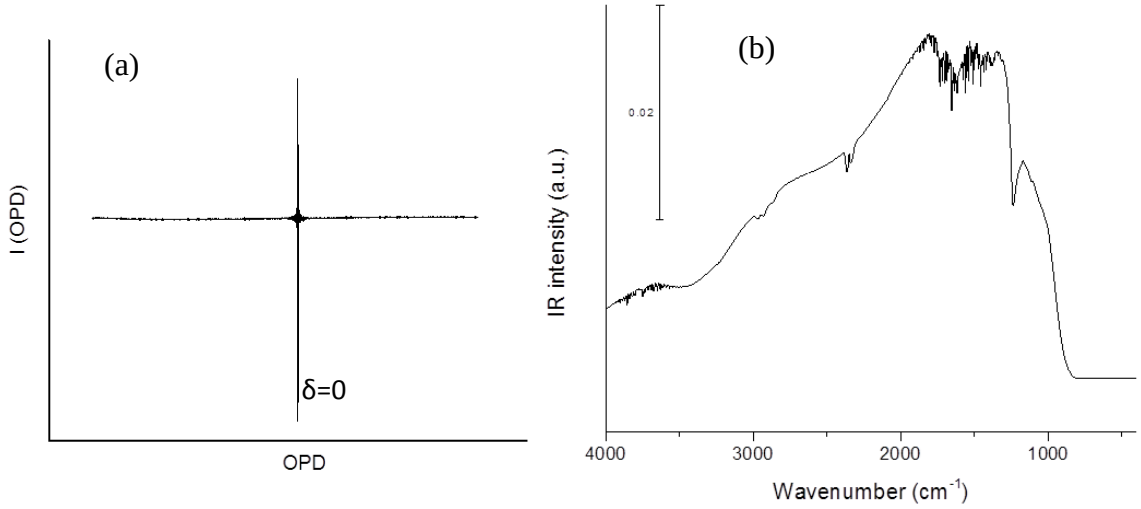

Figure 2.3: For a glow bar IR source with continuous frequency: (a) the interferogram, (b) the single channel absorption spectrum (measurements performed with PM-IRAS setup).

2.3.2.2 Infrared Reflection Absorption Spectroscopy (IRAS)

Comparing to other vibrational spectroscopic techniques, such as high resolution electron energy loss (HREELS) and surface enhanced Raman spectroscopy (SERS),

IRAS has a very high sensitivity (1/1000 monolayer CO), a high resolution (1 cm^{-1}), and has no pressure restriction as for HREELS ($<10^{-6}$ Torr) [68]. It has become one of the most powerful surface characterization techniques since its introduction in 1960s. IRAS is based on the interaction of the electric field of the light with the molecule (more precisely the dipole moment) adsorbed on sample surface. According to the surface selection rule, only the *p*-polarized light can be absorbed by the molecules on the surface, and the adsorbed molecules need to have a net dipole perpendicular to the surface [69]. The first requirement is due to the different phase change of the electric field for different polarized light on the surface. As shown in Figure 2.4, for *s*-polarized light (with electric field perpendicular to the plane of incidence), the electric field at the surface suffers a phase shift of 180º for all angle of incidences, thus no essential electric field to interact with the dipole moment of a vibrational modes in parallel to the surface. On the other hand, for *p*-polarized light (with electric field in the plane of incidence), the phase shift changes with the angle of incidence and the electric field intensity reaches maximum at near grazing incidence. The second requirement originates from the fact that an image dipole can be induced once a molecule adsorbs to the metal surface. As shown in Figure 2.5, the net dipole will be enhanced if the molecules adsorbs perpendicularly to the surface, while the dipole moment is eliminated when the molecule is parallel to the surface, resulting in no interaction with the electric filed of the light.

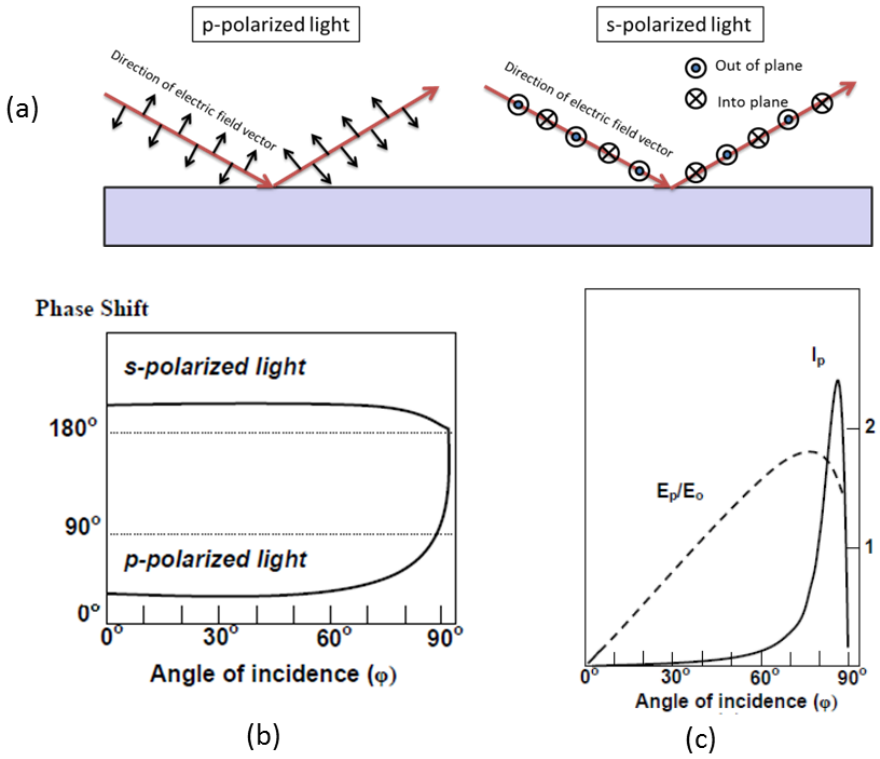

Figure 2.4: (a) The electric field vectors of *p*- and *s*-polarized infrared radiation on a metal surface. (b) Phase shift as a function of the angle of incidence. (c) Intensity of *p*-light as a function of incidence angle. (Figure 2.4 (b-c) are adapted from Ref [69].

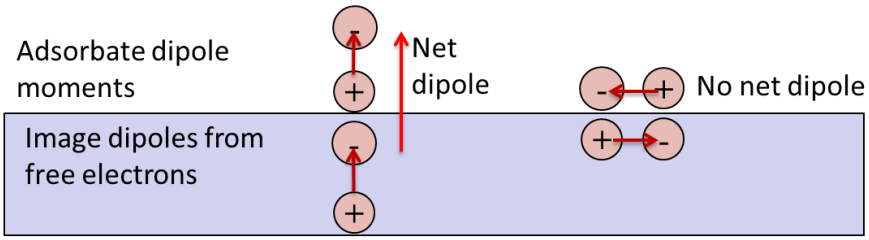

Figure 2.5: Net dipole moment of adsorbates on a metal surface with different orientation

Therefore, in a typically IRAS measurement, a *p*-polarized infrared beam impinges on a sample at near grazing incidence angles and excites the adsorbates on the sample surface, and the reflected beam will be detected to generate the absorption

spectrum. This allows for the precise measurement of position, intensity and coverage-dependent shift of vibrational bands, thus providing information about lateral interactions between adsorbed molecules and their orientation. Extensive IRAS studies on metal single crystal surfaces and model supported catalysts have provided invaluable information of different catalytic reactions [25, 60, 69-75].

2.3.2.3 PM-IRAS principle

The IRAS is virtually independent of pressure. However, the IR absorption signal on the surface is very week at elevated pressures, even at a near-grazing incidence angle. At high pressures, the signal from the adsorbates on model catalyst surface (usually with an area less than 1 cm^2) is orders of magnitude smaller than the gas phase signal and can easily get obscured. Take carbon monoxide as an example, which is the most preferred probe molecule in surface science, the signal of adsorbed CO molecules easily gets obscured by the gas phase signal at pressure above 10^{-3} mbar. Figure 2.6(a) exhibits the IRA spectrum of 100 Torr CO adsorption on Pt(100) at 325 K. It is obvious the signal from linear CO molecules adsorbed on Pt(100) surface (2100 cm^{-1}) is overwhelmed by the gas phase CO absorption (2143 cm^{-1}). To identify the adsorbates or intermediates on catalyst surface during reactions and elucidate elementary steps involved, it is crucial to remove the gas phase signal interference.

Therefore, to discriminate the surface adsorbate signal from the gas phase signal, detection techniques that can remove gas phase interference at high pressures are required for the investigations of different catalytic systems. The inclusion of polarization

modulation during IRAS measurements can achieve this goal successfully by subtracting out the gas phase signal, as shown in Figure 2.6(b). PM-IRAS can detect sub-monolayer coverages from UHV to atmospheric pressure and is thus able to interconnect classical surface science studies at more industrially-relevant conditions through the study of adsorbed or reacting molecules on catalyst surfaces. The PM-IRAS technique was applied for the first time in 1996 by Beitel *et al.* for *in situ* heterogeneous catalysis study on model catalyst systems, e.g. CO adsorption on Co(0001) surface under 1-600 mbar of pressure at temperatures between 300 and 550 K [76].

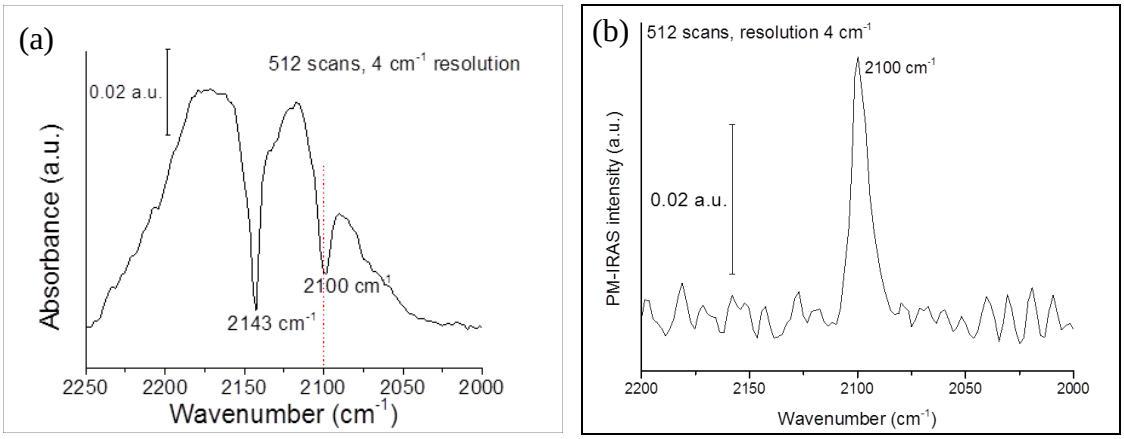

Figure 2.6: (a) IRA spectra, and (b) PM-IRA spectra of 100 Torr CO adsorbed on Pt(100) at 325 K.

According to the metal surface selection rule described, both *p*- and *s*-polarized light are absorbed by gas phase molecules, while only *p*-polarized light is absorbed by molecules adsorbed on the metal surface (the effective surface intensity of *s*-polarized infrared light on a metal surface is basically zero and no surface absorption occurs). Thus,

if the light can be modulated between *p*- and *s*- polarization at a high frequency and the signals are collected simultaneously, a (p-s) spectrum that represents the vibrational feature of the surface species can be obtained in a real-time manner, virtually independent of the environmental conditions.

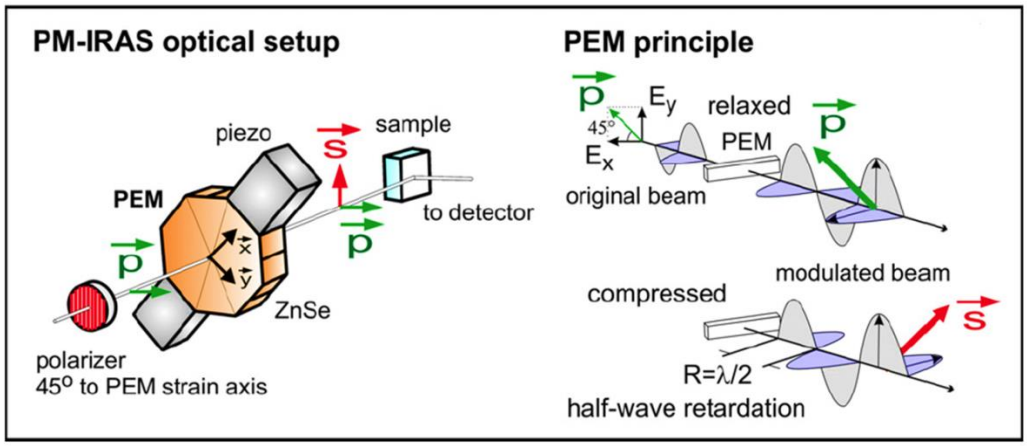

Figure 2.7: Operation principle of PEM (adapted from Ref [55])

This polarization modulation is typically achieved by using a photoelastic modulator (PEM), which produces oscillating birefringence at a fixed frequency. The operation of PEM is based on the photoelastic effect, describing the birefringence of a crystal material (e.g. ZnSe) as being proportional to mechanically stress (compress or stretch) forced on it. During operation, the two orthogonal components of the *p*-polarized light, as shown in Figure 2.7, will translate in a sinusoidal way along the axis of the PEM being stressed, resulting in a phase retardation between these two components. When the peak retardation is set to one half of the light wavelength (half-wave retardation mode), the PEM rotates the light polarization by 90º. Thus the modulated light impinging on the

sample can be switched at a frequency of 50 kHz between *p*- and *s*- polarizations. Since this polarization switch occurs twice within each PEM oscillating cycle, the sampling frequency is 100 kHz. Consequently, both spectra of *p*- (surface and gas phase) and *s*- (gas phase) can be acquired nearly simultaneously, and the vibrational signature of the surface species can be obtained from the (*p*-*s*) spectra after demodulation process.

2.3.2.4 PM-IRAS optical setup

In this thesis, the polarization modulation optics and the IR spectrometer (Bruker Equinox 55) were located on a vibration-isolation table with pneumatic legs (Thorlabs) and purged with dry, CO_2-free compressed air (Parker 75-62 FTIR purge gas generator). As shown in Figure 2.8, the collimated IR beam exited the external window of the interferometer and was reflected by two Au-plated mirrors, one flat mirror and one parabolic mirror. The second parabolic mirror had a 15.75" focal length and was positioned 15.25" from the sample, so that the beam diameter was 1 mm rather than a point on the sample surface. After reflection from the mirrors, the IR beam passed through a wire-grid polarizer (Reflex Analytical Al/KRS-5), so that the transmitted IR radiation from the polarizer had only a *p*-polarized electric field vector. The linearly-polarized IR beam then passed through a photoelastic modulation (PEM) optical head (II/ZS50, 50 kHz, Hinds Instruments) with a zinc selenide crystal aligned 45^o from the sample surface normal. The PEM shifted the polarization of the IR beam by 90^o and modulated it between the *s*- and *p*-polarization at 50 KHz. The modulated IR beam then entered the high pressure cell through a KBr window and impinged on the sample at an

incidence angle of ~85^{o} from the surface normal. The reflected beam exited the high pressure cell through another KBr window, and then was collected by a focusing mirror onto the liquid nitrogen-cooled, narrow-band MCT detector. The signals from the PEM and MCT detector were fed to a lock-in amplifier, and the separated output signals from the lock-in amplifier were processed to yield the final surface spectra.

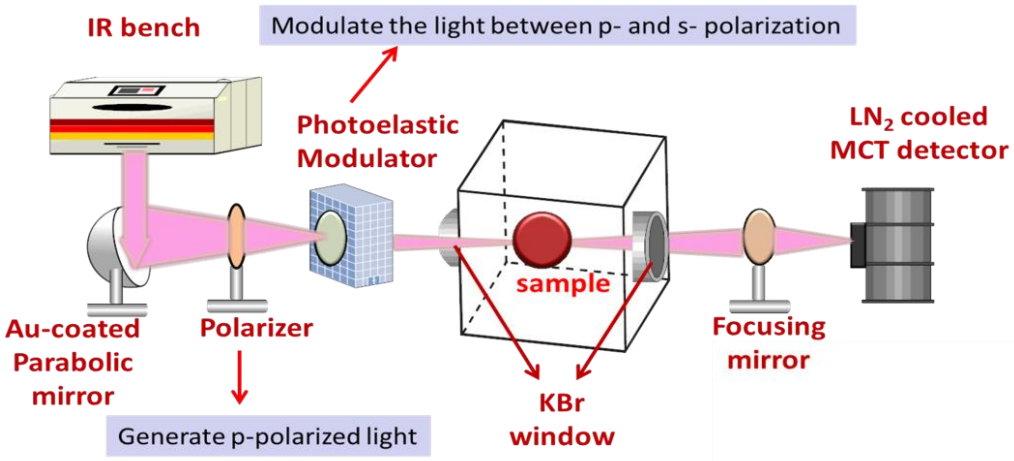

Figure 2.8: Optical view of PM-IRAS system

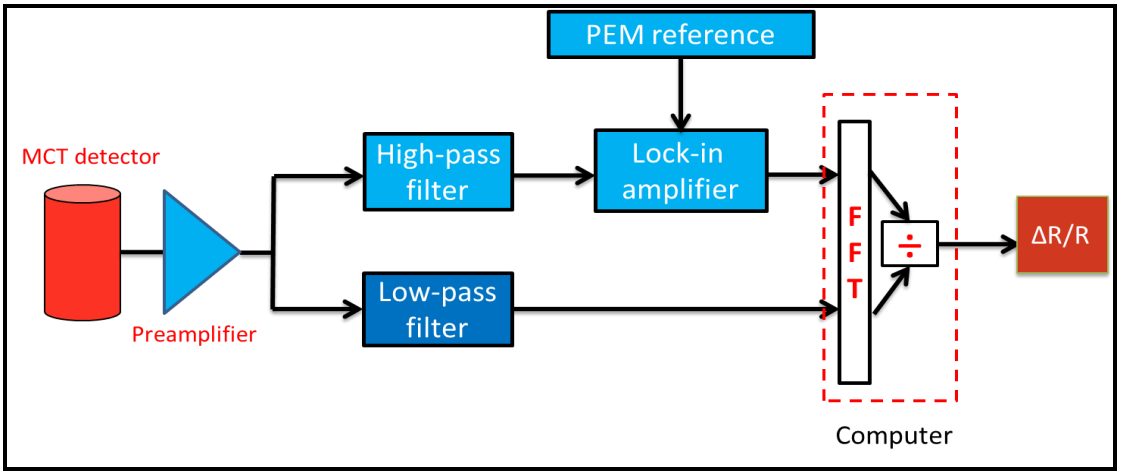

Figure 2.9: Signal processing of PM-IRAS (demodulation process)

In principle, there are two demodulations need to be processed before we obtain the differential signal (Rp-Rs) and average signal (Rp+Rs), since the IR beam has been Fourier-modulated by the IR interferometer at the beginning and polarization-modulated by the PEM before it impinges on the sample surface. Typically, the original output signal from the mercury-cadmium-telluride (MCT) detector is preamplified and then split into two different channels going through different demodulation process to gain the two desired spectra. The PEM usually has a frequency several times higher than the highest Fourier frequency of interest, and the doubly modulated signal can be first demodulated at the PEM 2f frequency by using a lock-in amplifier or a synchronous sampling demodulator, followed by the Fourier transformation, to gain the differential signal (Rp-Rs). As shown in Figure 2.9, the amplified signal goes through a high-pass filter which allows the high frequency modulated differential signal pass through, and demodulated by a lock-in amplifier referenced to the PEM 2f frequency. This demodulated signal is then sent to the FT-IR electronic for phase correction and fast Fourier transformation, generating the differential signal (Rp-Rs). In the other channel, the signal is passed through a low-pass filter to remove the high PEM frequency. This signal, now containing only the low frequencies, is digitized and recorded to produce an interferogram, which can be transformed in a single beam specta containing the average absorption of *p*- and *s*-polarized light in the system. After normalizing to the background spectra on the clean surface, the final spectra ($\Delta R/R$), containing only surface species information, is obtained.

Mathematically, the PM-IRAS spectrum, or the differential reflectance spectrum ($\Delta R/R$), can be calculated from the two spectra acquired simultaneously based on the equation proposed by Barner et al [77]:

$$\Delta R/R \approx [(1-\cos\varphi_0)/2-(\Delta I)/(I_a)x(\sin^2 \varphi_0)/8]\ x(\Delta I)/(I_a)$$

Where $\Delta I=I_p-I_s$, $I_a=(I_p+I_s)/2$, I_p and I_s are the intensity of p- and s- polarized light; φ_0 is the phase shift, which is linearly proportional to the modulation voltage in the PEM and inversely related to the wavelength λ of the IR light. In simplification, the equation can be expressed as:

$$\Delta R/R \approx J_2(\varphi_0)(R_p-R_s)/(R_p+R_s)$$

$J_2(\varphi_0)$ is a second order Besel function that describes the variation of the PEM modulation efficiency with wavenumbers. The $J_2(\varphi_0)$ function gives a typical sinusoidal baseline to the spectrum which can be eliminated by subtracting $\Delta R/R$ by a fitted polynomial algorithm. The differential reflectance spectrum can also be normalized by taking a background spectrum of the clean surface under identical experimental conditions. In this work, all the PM-IRAS spectra reported were normalized by using background spectra of the clean sample, typically with 512 scans to ensure a good signal-to-noise ratio. For further information about the theory and the electronics involved in the PM-IRAS method for obtaining the differential reflectance spectra, the reader is referred to the literature [56, 57, 62, 76-78].

2.3.3 Diffuse reflectance infrared fourier transform spectroscopy

While IRAS works great for highly reflective samples, diffuse reflectance is an excellent sampling tool for both powdered and crystalline materials in the mid-IR and near-IR spectral ranges. It can also be used for analysis of intractable solid samples. Diffuse reflectance relies upon the focused projection of the infrared beam into the sample where it is reflected, scattered and transmitted through the sample material. The back reflected, diffusely scattered light (some of which is absorbed by the sample) is then collected by an ellipsoid or paraboloid mirror and directed to the detector optics. Only the part of the beam that is scattered within a sample and returned to the surface is considered to be diffuse reflection. Sometimes, nonabsorbent material (such as KBr, KCl, etc) can be used to dilute the sample if it is too absorbent.

In this thesis, the DRIFT spectra were taken on a Bruker Equinox 55 FTIR instrument with a DTGS detector, located in Horizon 1 lab 131 at the University of South Carolina. The instrument is equipped with an *in situ* reaction cell that is capable of heating and cooling the sample at desired rates, where the sample can be treated at different temperatures or exposed to different reaction gases. Typically, a background scan was performed after necessary pretreatment of the catalyst, and the sample scan was carried out during the experiments by averaging 500 scans in the mid-IR range 4000-400 cm^{-1} with a resolution of 4 cm^{-1}.

CHAPTER 3

CO Adsorption on Pt(100) from UHV to Elevated Pressures

In this chapter, the adsorption of carbon monoxide on Pt(100) from UHV to elevated pressures was investigated. A red peak shift was observed during sample heating process in the interested pressure range of 10^{-4} Torr-100 Torr, due to the decrease of dipole coupling effects. At 10^{-4} Torr, the absorbance band of CO adsorbed on Pt(100) surface was detected at the same position for each temperature during heating and cooling process. In other words, the adsorption of CO on Pt(100) is reversible during heating-cooling process at 10^{-4} Torr. However, at 2 Torr-100 Torr, the absorbance band of CO adsorbed on Pt(100) could not recover to the same peak position after high temperature heating process. Further temperature programmed desorption studies and IR measurements revealed that CO adsorbed as islands on the carbon-covered surface and lead to the same vibrational band with different coverages on different annealed samples. Dipole-coupling simulation was performed for CO adsorption on Pt(100) with random- and island- geometries, and the experimental data matched well with the simulation result with island geometry.

3.1 Introduction

Carbon monoxide (CO) has been used as a probe molecule in most surface science studies, due to its structure simplicity and large dynamic dipole moment. It is also an important molecule involved in many applications. For example, CO is one of the main pollutants from automobile exhaust, which has been regulated since 1970s [1, 2]. In addition, CO can cause poisoning effect in proton exchange membrane fuel cell and has been investigated extensively [79, 80]. The mechanism of CO dissociation during Fischer-Tropsch synthesis for liquid fuel production has been debated for a long time and more efforts are still needed to resolve the discrepancies [58, 81-86]. The adsorption of CO, the co-adsorption of CO with other molecules (such as H_2, O_2, NO, etc), and the oxidation of CO on metal or metal oxides have been studied since 1900's [31, 62, 63, 87-102]. In this work, a brief introduction focusing on CO adsorption on Pt single crystal surfaces will be introduced followed by recent studies at elevated pressures.

The binding states, adsorption and desorption kinetics, and adsorbate densities of CO on various Pt single crystals, including Pt(111), Pt(100), Pt(110), Pt(211) and Pt(210), were investigated with mass spectrometry and Auger electron spectroscopy by McCabe and Schmidt [103]. It was found that multiple binding states were observed on all planes, and the saturation CO density at 300 K was highest on the (100), (210), and (211) planes and lowest on (110). The desorption obey first order kinetics for all states with activation energies of the most tightly bound states varying from 36 kcal/mole on (211) and (210) to 26 kcal/mole on (110) and (111) [103]. Chemisorption of CO on clean, unreconstructed Pt(100)-1x1 was investigated in detail by Broden, Pirug and Bonzel using LEED and XPS, and they reported that the surface structure changed from c(2x2), (√2x3√)R45° to

c(4x2) as the coverage increased from 0.5, 0.67 to maximum coverage of 0.75 [104]. The chemisorption of CO on Pt(001) and Pt(111) were also investigated by Crossley and King using IRAS and isotopic techniques, and clear evidence of island formation at low coverage on Pt(001) was obtained from the vibrational spectra over the temperature range from 160 k to 440 K. The average island dimension was estimated from a dipole coupling model and the island size decreased from ~70 molecules per island to ~10 molecules per island as the temperature increased form 160 K to 440 K [105]. Barteau and the co-workers studied the adsorption of CO, O_2 and H_2 on reconstructed Pt(100)-(5x20) in detail with flash desorption spectroscopy, XPS and LEED techniques [106]. They revealed that the adsorption and desorption characteristics of CO on Pt(100)-(5x20) was different from those on the Pt(100)-(1x1) surface, and the (5x20) surface could reconstruct to (1x1) surface upon CO adsorption and the surface only returned to (5x20) structure after the adsorbates were completely desorbed from the surface. This surface reconstruction phenomena were investigated in detail by Behm et al. [90] and Thiel et al. [91] using LEED, TDS and EELS techniques. They reported that the Pt phase transition (5x20) → (1x1) initiated at low CO coverage (θ=0.05) with island formation of adsorbed CO molecules and completed at ideal coverage (θ=0.5) with c(2x2) adlayer structure, the process could be described as a "nucleation and trapping" mechanism and the difference in the low coverage heats of adsorption of CO on the hex and (1x1) phase was the driving force of Pt phase transition during CO adsorption. Martin et al. [107] demonstrated using IRAS and LEED that the adsorption of CO on Pt(100)-hex and Pt(100)-(1x1) surface was significantly different and similar phase transition hex → (1x1) during CO adsorption on Pt(100)-hex was observed due to island formation of CO molecules.

CO adsorption on Pt was also investigated at elevated pressure conditions, and it has been revealed that CO adsorption and dissociation is different due to the pressure change. For instance, a large-scale surface reconstruction of stepped Pt crystals was reported at high pressure condition using scanning tunneling microscopy. It was observed that flat terraces of stepped Pt crystals broke up into nanometer size clusters (2 nm x 2 nm) upon exposure to CO at pressures above 0.1 Torr [108]. In addition, McCrea et al. [109] used sum frequency generation (SFG) to detect the formation of a compressed overlayer of CO molecules on Pt surfaces at 40 Torr. In their report the surface was observed to roughen by generating more step or kink sites, which was proposed to facilitate dissociation of CO. Their investigations revealed that CO molecules dissociated under 40 Torr on Pt(557), Pt(111) and Pt(100) single crystals at 548 K, 673 K and 500 K, respectively. Another study using *Ab initio* cluster model calculations supported their findings showing that CO dissociation is easier on Pt(100) than Pt(111), and high pressure is required for CO dissociation on both surfaces [110].

During the dissociation process it is possible for carbon to be trapped on Pt surface as graphitic species, effectively blocking potential binding sites. Carbon deposition on Pt has been reported when the samples are exposed to a carbon source such as CO, ethylene or propylene at temperatures above 673 K [111-118]. Formation of graphite islands has been observed on Pt samples at temperatures above 673 K [114-117] and their shape was highly influenced by the substrate structure. In particular, CO dissociation has been attributed to the formation of graphite islands in the kinked area of a rounded Pt single crystal at 850 K [113]. More recently, Nilsson *et al*. [118] demonstrated that continuous graphene sheets could grow on the hex-constructed Pt(100)

surface without lifting the reconstruction when Pt(100) was exposed to 100-200 L of either ethylene or propylene at 973 K.

However, to date, there have been very few detailed spectroscopic studies on CO adsorption on Pt(100) from vacuum condition to near atmospheric pressure. In addition, CO dissociation and carbon island formation effects on CO adsorption on Pt(100) at elevated pressures remains to be revealed. In this work, we performed systematic experiments to investigate adsorption of CO on a Pt(100) single crystal surface from 10^{-4} Torr to 300 Torr at different temperatures using PM-IRAS. Carbon islands formation at elevated pressure and temperature was deduced from TPD and IR measurements of CO adsorption on the carbon-deposited samples. The island formation of CO adsorbed on the annealed samples also matches well with the dipole coupling simulation results. Similar characterization method has been applied successfully in previous studies of CO adsorption and dissociation on metal surfaces [105, 119, 120].

3.2 Experimental methods

3.2.1 High-pressure-compatible UHV reaction system

The experimental system consisted of a UHV base chamber and a high pressure reaction cell, as shown in Figure 3.1. The base pressure of the system was $2x10^{-9}$ Torr. The high pressure cell (volume 1.25 liter) capable of handling a range of pressures from UHV to ambient conditions was separated from the base chamber by a gate valve (MDC 300004), which allows the base chamber to retain UHV conditions while the high pressure cell is pressurized. The two chambers were pumped either separately or together.

The base chamber was constantly pumped by a turbomolecular pump (Varian Turbo V 250, Macro Torr), which could also pump the high pressure cell when the gate valve was open. The upper chamber was equipped with a separate turbomolecular pump (Varian Turbo V 70LP, Macro Torr). During experiments, gases were introduced to either or both chambers, via a leak valve in the base chamber and a gate valve in the upper chamber. A three-dimensional translational stage (MDC PSMA-1512) equipped with compressible and flexible cooper bellows allowed for fine position control and provided an *in situ* sample transfer mechanism between the UHV chamber and high pressure cell. The base chamber included an Ar-ion sputter gun (Omicron ISE 5) for sample cleaning and a quadrupole mass spectrometer (MS) (Hiden HAL IV RC) for residual gas analysis.

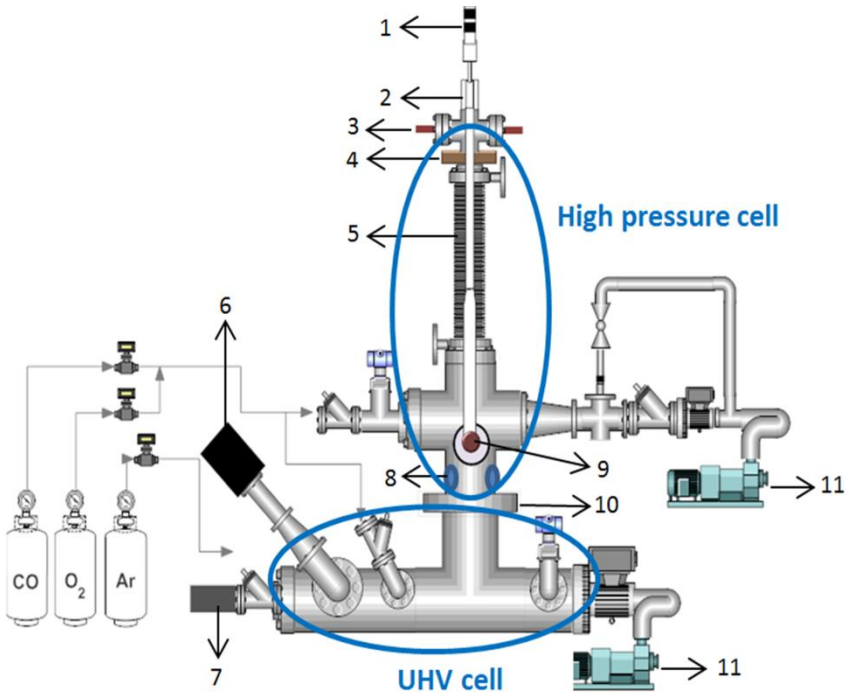

Figure 3.1: High-pressure compatible UHV reaction system: (1) Liquid nitrogen feed line for cooling; (2) Thermocouple feed through; (3) Copper feed through for heating; (4) Rotation stage (θ=0-360º); (5) Transitional stage (X, Y, Z); (6) Mass spectrometer; (7) Ion gun; (8) KBr window; (9) Sample, e.g. single crystal Pt(100); (10) Gate valve; (11) Pumping system (Turbo pump & roughing pump).

The model catalyst studied was vertically mounted inside the chamber. Two tantalum wires were spot welded to the back of the sample and used to suspend the sample from a copper sample holder that was electrically isolated from the rest of the internal system. Insulated copper ribbon connecting external electrical feedthroughs with the sample holder allowed the sample to be resistively heated up to 1500 K using a DC power supply (Lambda) by passing current through the tantalum wires. A K-type thermocouple was also spot-welded to the back of the sample for temperature measurement. Heating and cooling were computer controlled within ±0.5 K. A key advantage of the setup is that the thermocouple was in direct contact with the sample, providing exact measurement of the sample temperature. Similar systems often estimate sample temperature by using a thermocouple connected near the sample, for example to the sample holder, or by pyrometer.

As a benchmark test of the PM-IRAS system, serial CO-TPD experiments were performed once the Pt(100) was cleaned using the method described in Chapter 2. Typically, the clean sample was exposed to pure CO at 10^{-6} Torr condition for certain amount of time (1 Langmuir = 10^{-6} Torr * 1s) at 300 K, and then the system was pumped down to the base pressure of 10^{-9} Torr prior the IR and TPD measurements. After the PM-IRAS measurement in the upper chamber, the sample was transferred to the bottom chamber where the MS was located for TPD measurements. The sample was heated from 300 K to 700 K with a ramping rate of 3 K/s, and the desorbed molecules were monitored with MS. High pressure studies of CO adsorption and dissociation were all performed in the upper high pressure cell where the IR spectra were taken during the experiments.

3.2.2 Dipole-dipole coupling model

The vibrational frequency of adsorbed molecules on metal surface is known to be influenced by the mechanical coupling of the molecule to the substrate, the dipole-coupling effect due to the dipole-dipole, dipole-self-image and dipole-other-image interactions, and the chemical effects due to the formation of chemisorption bond [69]. Frustrated translation of CO molecules, usually referred to as the anharmonic coupling of the molecule with the substrate, can provide the dephasing mode during heating and cause a red shift of the vibrational band due to rapid energy exchange between the adsorbates and the substrate [121, 122]. In addition, several studies have shown that adsorption of CO on metal surfaces can be explained by the Blyholder model [123, 124], in which CO molecules bond to the metal via the 5σ CO orbital, with simultaneous backdonation of electrons from the metal into the 2π* CO orbitals. Since 2π* orbitals are antibonding with respect to the CO bond, the backdonation leads to a weakening of C-O bond, thus a lower CO stretching frequency. Recently, Curulla *et al.* [125] used the *ab initio* cluster model approach to study adsorption of CO on Pt(100) and found that the dipole-coupling effect, which is dependent on surface coverage, is the main cause of frequency shift in CO stretching vibrational modes.

In this work, a dipole-coupling model was applied to examine the coverage-dependent frequency shift of the absorption band. The relationship between vibrational frequency and surface coverage is shown in Equations 3.1 and 3.2 [99, 126]:

$$\left(\frac{\omega}{\omega_s}\right)^2 = 1 + \frac{\theta\alpha_v\Sigma_0}{1+\theta\alpha_e\Sigma_0} \qquad (3.1)$$

$$\Sigma_0 = \sum_{i \neq j} \frac{1}{r_{ij}^3} + \frac{1}{\left| r_{ij} + 2d\hat{z} \right|^3} - \frac{12d^2}{\left| r_{ij} + 2d\hat{z} \right|^5} \qquad (3.2)$$

As shown in Equation 3.1, the frequency of surface adsorbates, ω, with respect to the singleton frequency of an isolated CO molecule on the surface, ω_s, is a function of the adsorbate coverage, θ, and the dipole sum Σ_0 at a complete coverage. Here, α_e and α_v, are fitting parameters associated with the electronic and vibronic polarizabilities of the adsorbed molecules. The dipole sum Σ_0 can be calculated according to Equation 3.2, in which r_{ij} is the distance between dipoles in the plane of the surface and d is the distance between the center of the molecular dipole and the image plane of the surface. In this work, the distance d was set to 1Å according to the literature [99, 100]. Based on previous work, the singleton frequency for CO adsorbed on atop sites on Pt(100) was selected to be 2067 cm^{-1} [107, 125]. The electronic polarizability was chosen to be 2.54 $Å^3$ following the estimation by Scheffler [127]. The vibronic polarizability was set to 0.21 $Å^3$, which was consistent with estimations used in previous CO dipole-coupling models [100].

Dipole coupling simulations were performed using an algorithm programmed in Python that utilized the Numpy random module, and represented a Pt surface as a 60 x 60 array with periodic boundary conditions. The array spacing was equal to the lattice spacing of the Pt(100) surface and CO molecules were only allowed to adsorb onto atop sites. The initial CO molecule was placed randomly on the surface. After the first CO molecule adsorbed, the next molecules were placed either next to or away from existing molecules. Coverage was defined as the ratio of the number of adsorbed CO molecules to the total number of adsorption sites. The dipole sum, Σ_0 and the band position of the

system were calculated and recorded for different θ values. This process was repeated multiple times for both random and island adsorbate geometries.

3.3 Results and discussion

3.3.1 CO adsorption on Pt (100) at low pressure

The first investigation in the PM-IRAS system was CO adsorption on Pt(100) surface. Serial TPD experiments were carried out on Pt(100) at a ramping rate of 3 K/s. The sample was exposed to CO molecules at 10^{-6} Torr for different time length at 300 K, and desorption profiles were monitored via MS. The coverages of different exposures at 10^{-6} Torr were calculated by normalizing the integral area of TPD spectra at each exposure to that of saturation coverage at 1000 L CO exposure, which was reported as 0.75 based on TPD and LEED measurements [105, 106, 128]. The surface coverage was also calculated via the dipole-coupling model based on the vibrational frequency as described in the following section, and the saturation coverage at 1000 L exposure was calculated as 0.77. This result matches well with the reported saturation coverage of 0.75, indicating a good prediction of the dipole-coupling model.

Figure 3.2 shows the PM-IRAS and TPD measurements of CO on Pt(100) at 300 K as a function of increasing exposure. In the IR spectra, 1 L CO of exposure led to a C-O stretching band at 2075 cm^{-1}, corresponding to CO adsorbed on atop sites [107, 129]. Increasing CO doses leads to a blueshift to 2094 cm^{-1} and beyond a dose CO exposure of 50 L, the band position remained constant up to the saturation coverage. The stretching

band position at saturation coverage is consistent with the literature, as reported at 2095 cm^{-1} on Pt(100) [105, 107, 128].

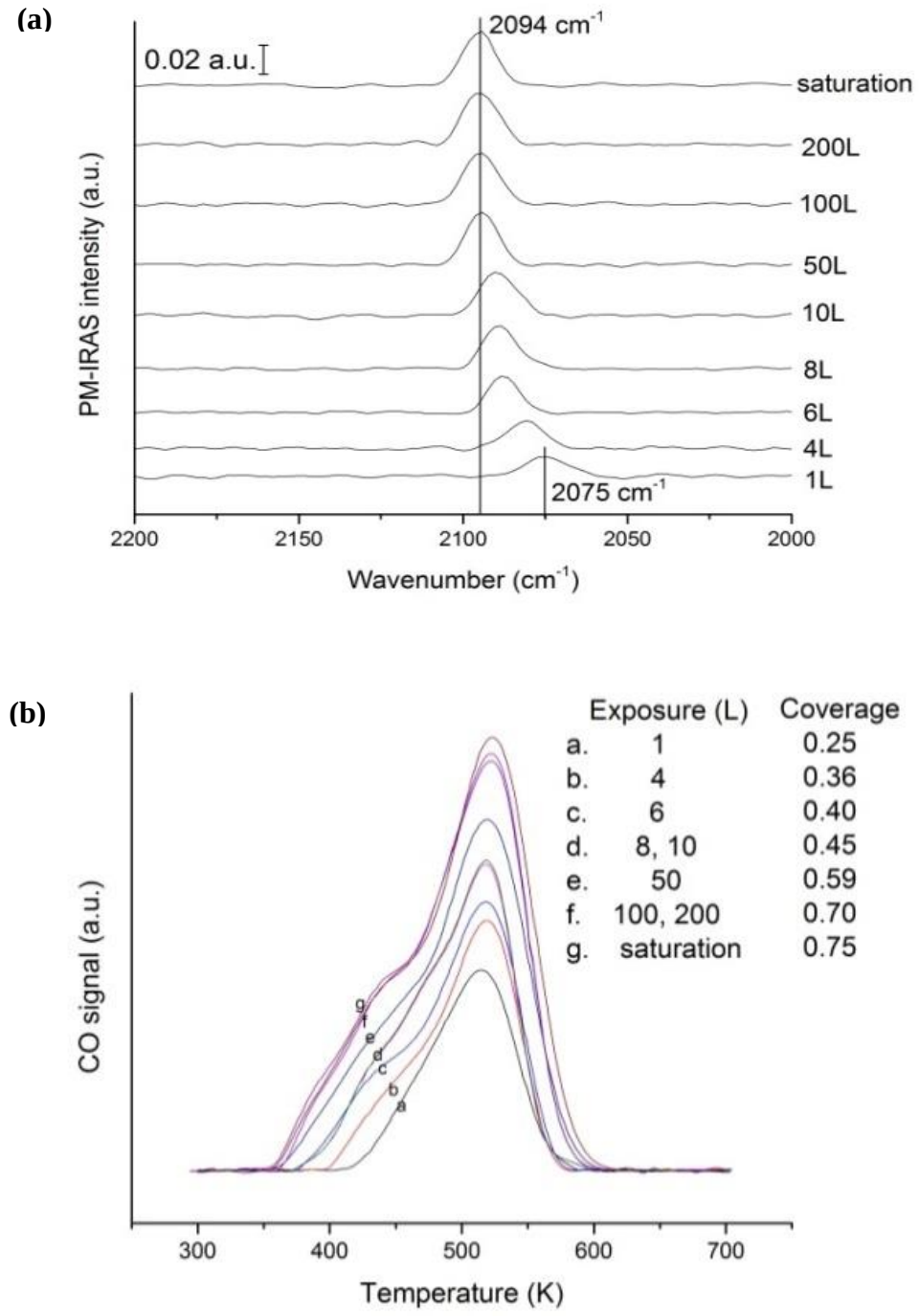

Figure 3.2: (a) IR spectra and (b) TPD profile of CO on Pt(100) after different exposures

The corresponding TPD spectra in Figure 3.2(b) indicate three characteristic CO desorption states. At 0.27 coverage, a single desorption peak was observed at 515 K which shifted to 522 K as the coverage increased to the saturation coverage. This peak is typically associated with CO on a p(1x1) Pt surface structure as previously observed via low-energy electron diffraction [106]. At coverages above 0.27, two additional desorption peaks developed at around 420 K and 470 K, which were associated with the high coverage structure (4x2)-CO [25] and repulsive interactions among the CO molecules, respectively [91]. The corresponding activation energies of desorption were calculated using the Redhead equation [130] as 32.1 kcal/mol, 28.8 kcal/mol and 25.6 kcal/mol for the TPD peaks located at 522 K, 470 K and 420 K, respectively. These activation energies match well with the literature, which are reported to be 31.6 kcal/mol at 522 K, 24-26 kcal/mol at 450 K and 23.6 kcal/mol at 400 K [91, 106].

3.3.2 CO adsorption on Pt(100) between 10^{-4} and 300 Torr

The pressure effect on CO adsorption was investigated from 10^{-4} Torr to 300 Torr. The vibrational spectra of CO adsorbed on Pt(100) at 325 K at different pressures are shown in Figure 3.3. The C-O stretching band was observed at 2096 cm^{-1} for a CO pressure of 10^{-4} Torr. Increasing the CO pressure to 1 Torr leads to a further blue shift of the IR band to 2099 cm^{-1}. The band position then remained constant at over a pressure range of 1-300 Torr. Only one C-O stretching band above 2090 cm^{-1} was observed at all pressures, which was associated with CO adsorbed exclusively on atop sites of Pt(100), with the axis of the adsorbed CO perpendicular to the Pt(100) surface [105, 125, 128].

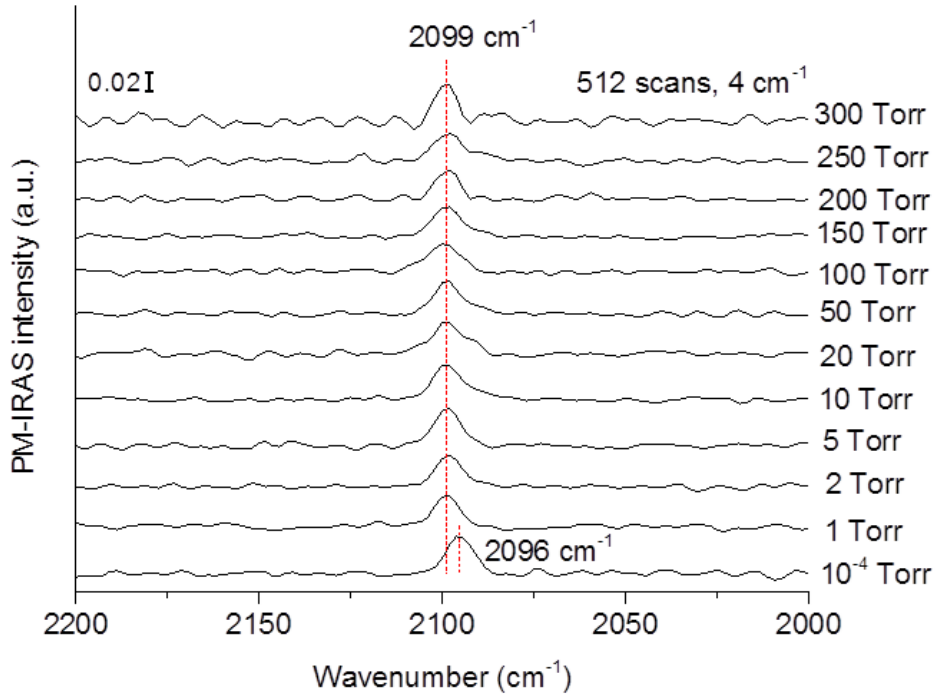

Figure 3.3: IR spectra of CO adsorption on Pt(100) from 10^{-4} Torr to 300 Torr

The temperature effect on CO adsorption was investigated at three different pressures, e.g., 10^{-4} Torr, 2 Torr, and 100 Torr, by performing heating and cooling cycles. In these experiments, the sample was heated from 325 K under flowing CO at constant pressure until CO completely desorbed from the surface, and then the sample was cooled back down to 325 K. As shown in Figure 3.4a, the C-O stretching band was located at 2096 cm^{-1} at 325 K and exhibited a red shift upon heating until its final disappearance at 625 K under 10^{-4} Torr CO. The sample was then cooled down, during which CO molecules readsorbed on the surface and the peak reappeared at 2080 cm^{-1} at 525 K. The red shift of the band position during the heating process was due to the decreased dipole coupling effect between the CO molecules remained on the surface. Upon cooling, CO molecules readsorb on the surface and the band position shifted to higher wavenumber with increasing dipole coupling effect. The band positions at each temperature below 525

K during the heating and cooling cycle were found to be the same and the initial C-O band position of 2096 cm^{-1} at 325 K was recovered after the cooling cycle, showing that the heating process had a reversible impact on the adsorption of CO at 10^{-4} Torr.

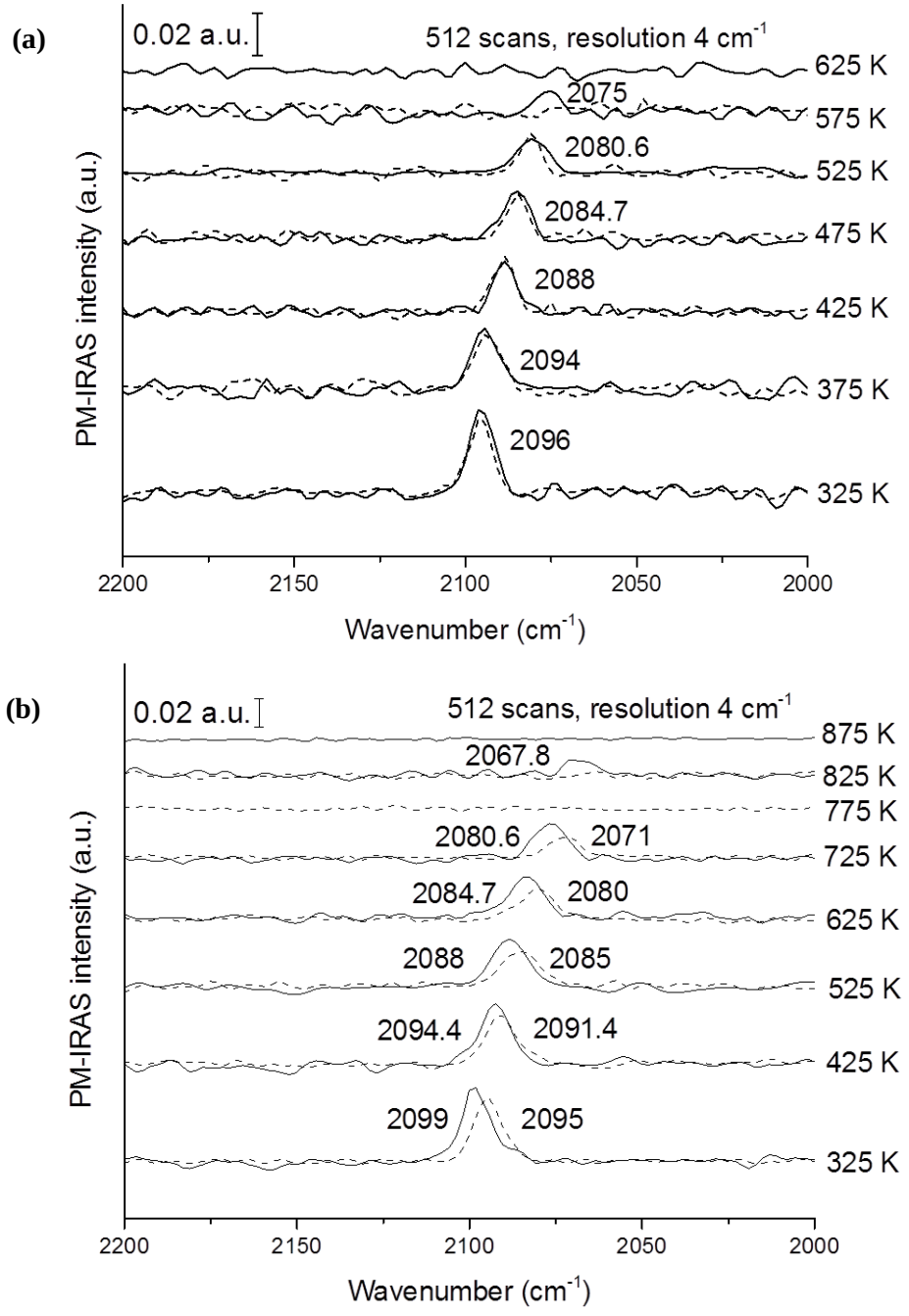

Figure 3.4: IR spectra of CO on Pt(100) during heating (solid line) and cooling (dash line) process at (a) 10^{-4} Torr CO, (b) 2 Torr CO

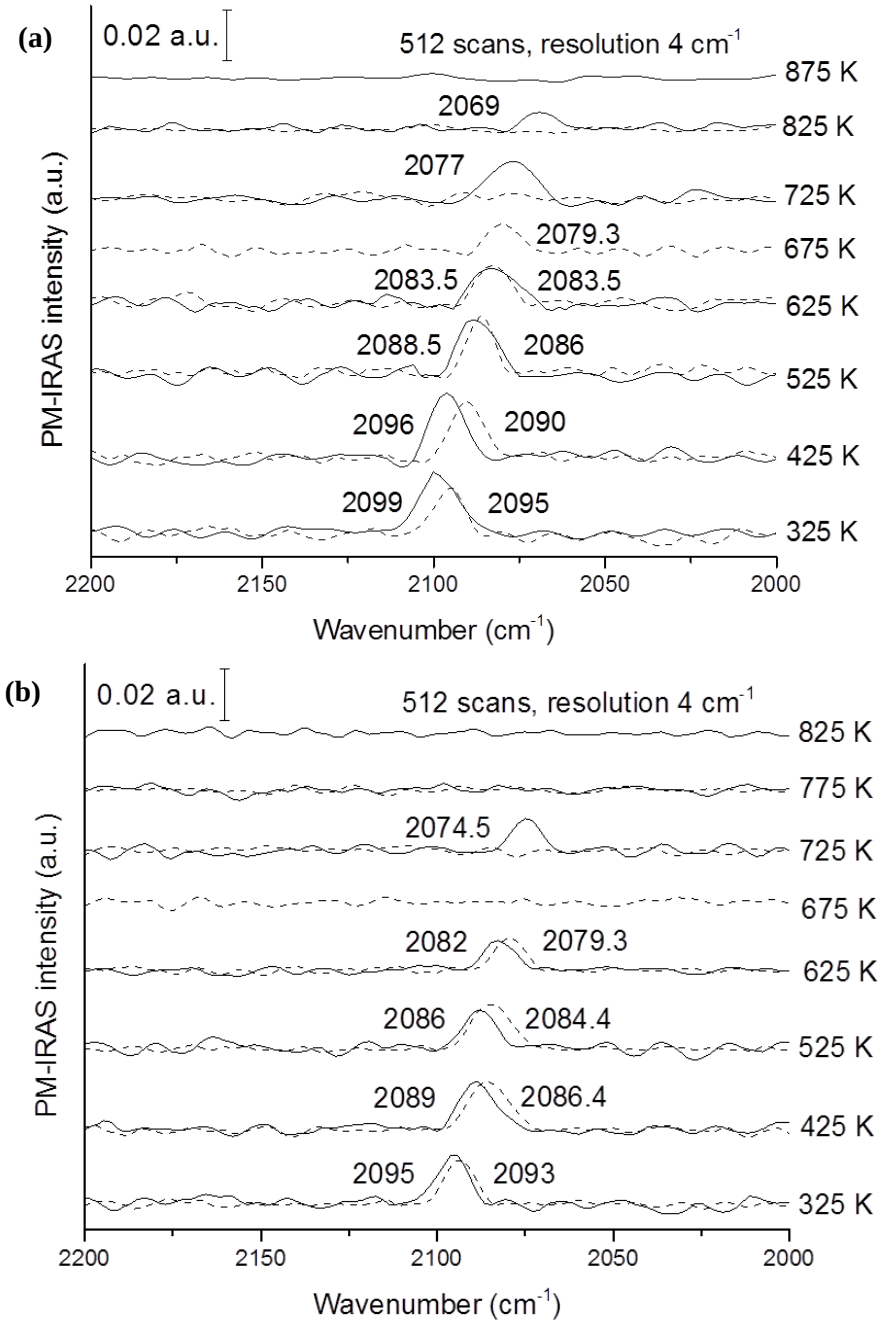

Figure 3.5: IR spectra of CO on Pt(100) at 100 Torr, (a) during first heating (solid line) and cooling (dash line) process (b) during repeated heating-cooling process after (a)

However, as the CO pressure was increased to 2 Torr, the sample temperature was found to have an irreversible impact on CO adsorption. As shown in Figure 3.4b, the C-O band was located at 2099 cm^{-1} at 325 K, 3 cm^{-1} higher than the band location at 10^{-4} Torr at the same temperature. Upon heating, the C-O band showed a red shift and disappeared at 875 K, a temperature 250 K higher than at 10^{-4} Torr. During the cooling process, the C-O band first reappeared at 2071 cm^{-1} at 725 K and blue shifted to 2095 cm^{-1} at 325 K. The C-O band location during cooling is consistently lower by 3-5 cm^{-1} if compared with the heating data. The cyclic adsorption behavior was probably due to CO dissociation at elevated pressure and temperature condition, causing carbon island formation on the surface and attenuated the dipole coupling effect of the readsorbed CO molecules during cooling.

Different IR spectra of CO during heating and cooling were also observed at 100 Torr. As shown in Figure 3.5a, the C-O stretching band was located at 2099 cm^{-1} at 325 K and it completely disappeared at 875 K upon heating. During cooling, the C-O band first reappeared at 2080 cm^{-1} at 675 K, and blue shifted upon further cooling to 2095 cm^{-1} at 325 K. A second heating and cooling cycle was subsequently applied. As shown in Figure 3.5b, the C-O stretching band now disappeared at 775 K upon heating and returned back at 625 K with a frequency of 2079 cm^{-1}. Further cooling resulted in a blue shift of C-O stretching band to 2093 cm^{-1} at 325 K, 2 cm^{-1} lower than that of the first heating and cooling cycle. This cyclic adsorption behavior due to carbon deposition on the surface was further investigated systematically with TPD and PM-IRAS, and the results will be discussed in detailed later.

3.3.3 Coverage-dependent frequency shift of the absorption band

Surface coverages of the adsorbed CO molecules at different temperatures for pressure range from 10^{-4} Torr to 300 Torr were calculated via the dipole-coupling model. The vibrational frequencies obtained at 10^{-4} Torr (2096 cm^{-1}) and 1-300 Torr (2099 cm^{-1}) corresponded to surface coverages of 0.85 and 1, respectively. Higher adsorbate pressures resulted in a surface coverage above the saturated surface coverage of CO (0.75) at 10^{-6} Torr [90, 103, 105]. In addition, surface coverage of the heating and cooling cycle experiments conducted at 10^{-4} Torr, 2 Torr and 100 Torr were calculated and plotted as a function of sample temperature.

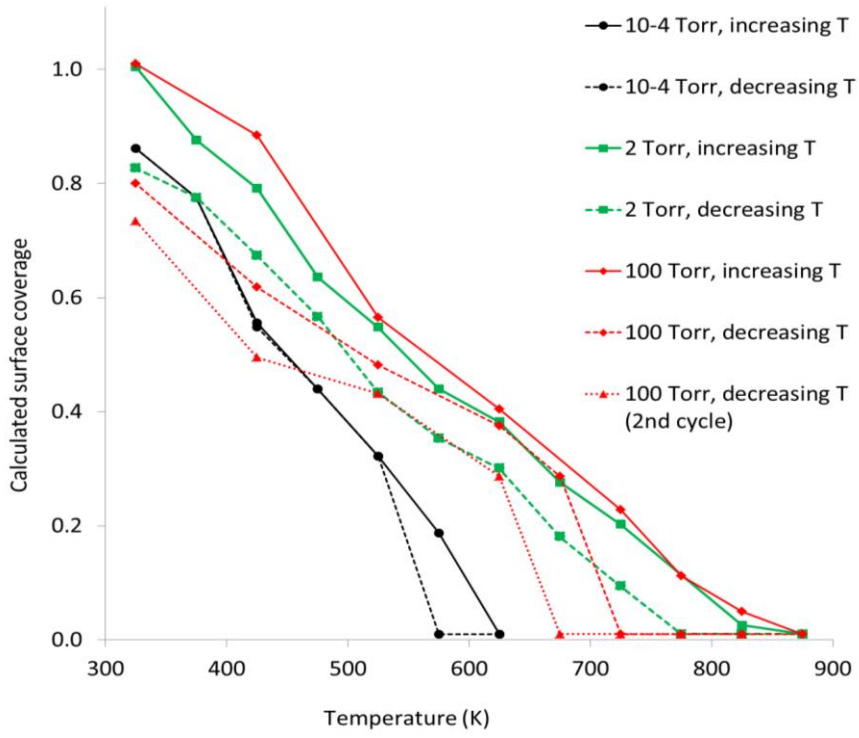

Figure 3.6: Surface coverages as a function of temperature at different pressures (calculation based on dipole coupling model with measured frequency)

As shown in Figure 3.6, the surface coverage decreased with increasing sample temperature at all pressures due to desorption of CO molecules from the surface. A decrease in the amount of CO molecules on the surface could mitigate the effect of dipole couplings, as supported by the red shift of the C-O stretching band. Previously, McCrea *et al*.[109] also observed a red shift for CO adsorption on Pt surface during heating, and they proposed that it was due to the anharmonic coupling between low frequency modes of the adsorbed molecules and the substrate. They ruled out the possible dipole coupling effect based on the small variation (<10%) of the C-O band amplitudes obtained from SFG spectra. However, Brandt *et al*.[131] pointed out that C-O band is dependent on both harmonic coupling between CO molecules, and the coordination number of Pt atoms on which CO molecules are adsorbed. In our case, there was more than 20% change of the C-O band amplitude, and reduction of dipole coupling effect was considered as the main reason of the red band shift. Upon cooling, CO molecules readsorbed on the sample and the surface coverage increased until it recovered at 0.85 with a vibrational frequency of 2096 cm^{-1}, indicating that the heating-cooling process did not affect CO adsorption on the Pt surface [91].

However, coverages calculated during the heating and cooling cycle did not follow the same trend at higher pressures. As shown in Figure 3.6, at 2 Torr and 100 Torr, the Pt(100) surface was found to be fully covered with CO at 325 K, and the surface coverage decreased with increasing the sample temperature. Upon cooling, initial surface coverage at 325 K could not be recovered at both pressures, suggesting that the adsorption sites on Pt(100) might have been blocked by possible carbon deposited via CO dissociation [132]. Furthermore, the surface coverage of CO was always found to be

lower in the cooling process in comparison to the heating process at higher pressures. The second heating and cooling cycle at 100 Torr increased the observed difference of band shift, indicating that the available top sites on Pt(100) decreased due to the carbon deposition at elevated pressure and temperature.

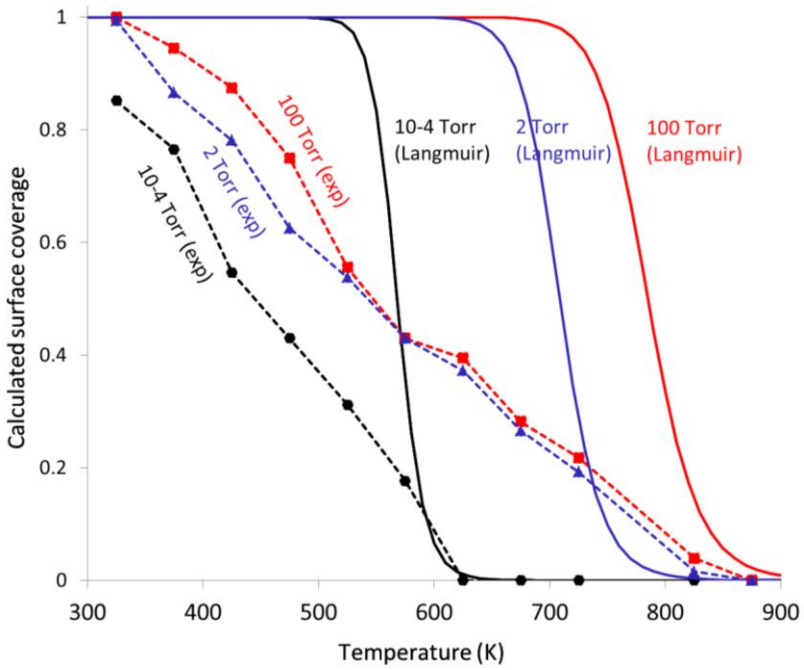

Figure 3.7: Surface coverages as a function of temperature, a comparison between dipole coupling model and classic Langmuir adsorption model

Adsorption-desorption equilibrium of CO was also interpreted with a Langmuir adsorption model [130]. As shown in Figure 3.7, CO was found to completely desorb from the surface at temperatures above 625 K, 800 K and 900 K at 10^{-4} Torr, 2 Torr and 100 Torr CO, respectively. The complete desorption temperatures, calculated via the Langmuir adsorption model, matched well with the temperatures determined from the experiments. However, it was clear that the Langmuir desorption trend of CO with

increasing temperature did not show a high degree of agreement with those obtained from the experiments, as shown in Figure 3.7. This mismatch is due to the fact that the Langmuir adsorption model does not take into account of the dipole-coupling and electron donation-backdonation effects [99, 124]. Hence, as the adsorbate pressure increases, e.g. at 100 Torr CO, the difference between CO desorption trends determined with Langmuir adsorption and dipole-coupling model can be more pronounced.

3.3.4 Effect of annealing on CO adsorption on Pt(100)

The cyclic adsorption behavior of CO on Pt(100) was further investigated by performing annealing experiments at 100 Torr CO. Three different maximum annealing temperatures, e.g., 775 K, 825 K and 875 K, were chosen, and the sample was kept at each annealing temperature for 10 min, 30 min and 1 h. After each annealing process, the chamber was pumped down to below $1x10^{-8}$ Torr with the sample temperature at 300-350 K, and then the sample was rapidly heated up to 800 K to ensure that no CO remained on the surface. Finally, the sample was exposed to 100 L CO at 300 K, and both PM-IRA and TPD spectra were collected and compared with measurements of a freshly cleaned sample. As shown in Figure 3.8-3.10, three characteristic CO desorption peaks were detected at 417-425 K, 470-479 K and 517-521 K on all the annealed samples. The area of each characteristic peak was found to decrease with annealing time and maximum annealing temperature, as shown in Table 3.1 after peak fittings for each spectrum.

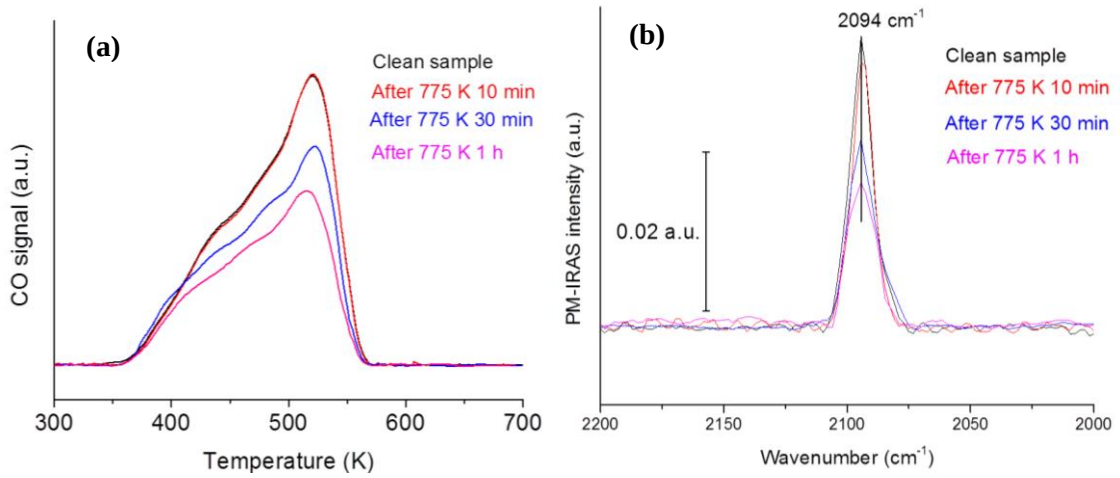

Figure 3.8: (a) TPD spectra of 100 L exposure to the annealed sample after 775 K heating in 100 Torr CO environment, (b) the corresponding IR spectra of 100 L CO on Pt(100)

Figure 3.8 shows the TPD and PM-IRA spectra collected after the annealing experiment at 775 K. After 10 min annealing time, the TPD spectra was found to be very similar to that of the clean sample. However, as the annealing time increased to 30 min and 1 h, the total area under the CO desorption trace was decreased by 21.3% and 36.2% relative to measurements of the clean sample, respectively. A similar trend was also observed in the corresponding IR spectra. It was found that the intensity of the C-O stretching band did not change significantly after 10 min of annealing. However, the peak intensities at 30 min and 1 h annealing times were found to decrease by 35.3% and 52.9%, respectively. Interestingly, no shift in the band position was observed in the IR spectra as the annealing time increased and its location remained constant at 2094 cm^{-1}. Experiment at a lower maximum annealing temperature of 725 K was also performed. Both TPD and PM-IRA spectra showed that CO desorption peaks and IR band were the same before and

after the 725 K annealing process for 1 h, indicating that CO dissociation at elevated pressures only occurred obviously at temperature above 725 K.

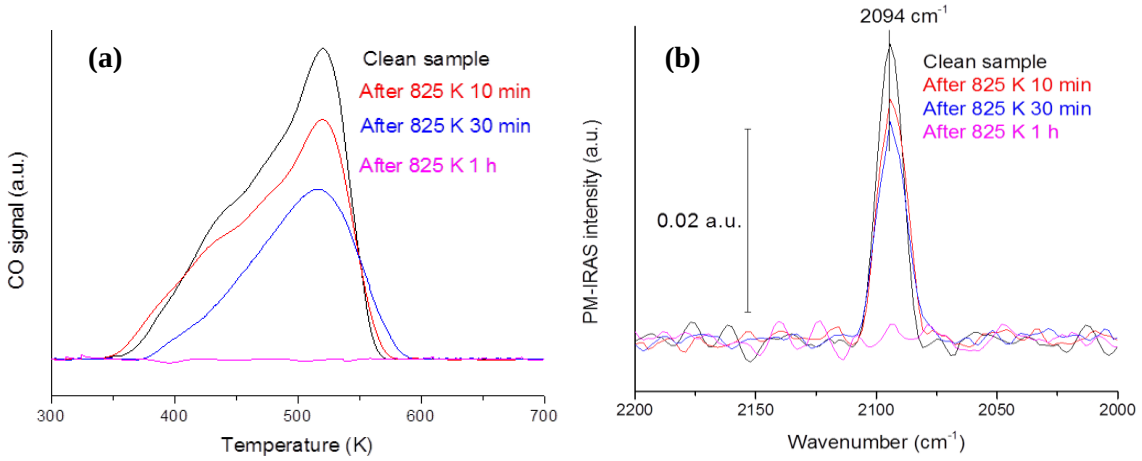

Figure 3.9: (a) TPD spectra of 100 L exposure to the annealed sample after 825 K heating in 100 Torr CO environment, (b) the corresponding IR spectra of 100 L CO on Pt(100)

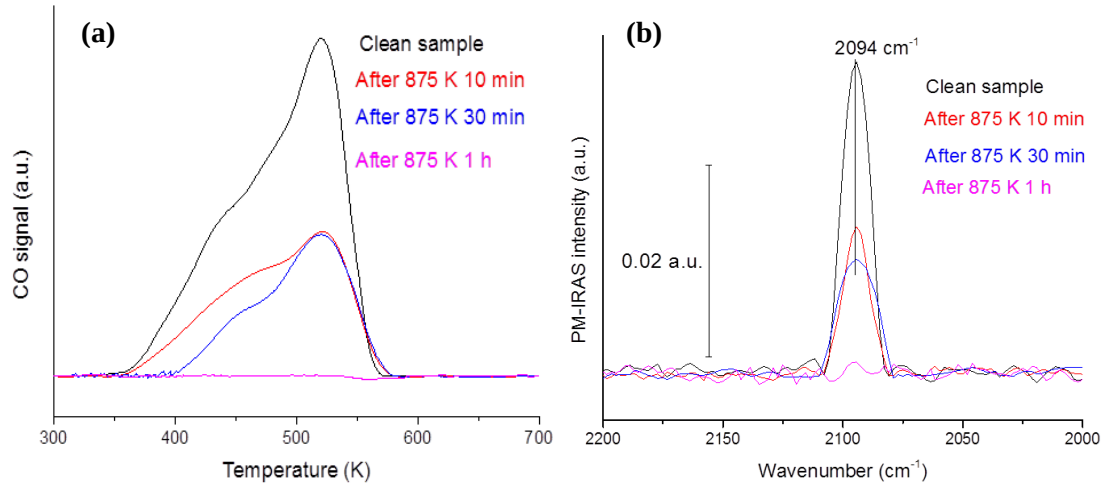

Figure 3.10: (a) TPD spectra of 100 L exposure to the annealed sample after 875 K heating in 100 Torr CO, (b) the corresponding IR spectra of 100 L CO on Pt(100)

Comparing to the results at 775 K, the decrease in TPD area was more pronounced at an annealing temperature of 825 K. As shown in Figure 3.9a, the total area

under the CO desorption trace was found to decrease by 13.5% and 42.5% relative to measurements of the clean sample after the 10 min and 30 min annealing times, respectively. As the annealing time was increased to 1 h, no CO was detected on the surface after 100 L CO exposure. These observations were in agreement with the corresponding PM-IRA spectra, as shown in Figure 3.9b. Intensities of the C-O stretching band were found to decrease by 25.3% and 33.3% after 10 min and 30 min annealing times relative to measurements of the clean Pt(100) surface, respectively. Although smaller peak areas in the IR and TPD spectra indicated substantially lower CO coverages, the C-O stretching band again did not red shift, and all the IR bands were located at 2094 cm^{-1}. Again, no IR band related to adsorbed CO was detected after 1 h of annealing, suggesting that the surface adsorption sites were completely blocked and CO could not adsorb on the surface.

As the annealing temperature increased to 875 K, the previously described effects become even more pronounced. The total area of the TPD spectra collected after 10 min and 30 min annealing times were found to decrease by 44.9% and 62.8%, respectively, as shown in Figure 3.10a. The corresponding IR spectra also indicated a strong decrease in the band intensity with increasing annealing time. As shown in Figure 3.10b, the band intensities were found to decrease by 52.9% and 61.5% without showing an obvious band position shift after 10 min and 30 min annealing times. After 1h annealing time, again no C-O stretching band was detected.

To assure no contamination was generated from the chamber during the annealing process, the clean sample was annealed at the base chamber pressure at 875 K for 1 h and then exposed to 100 L CO after cooling down to 325 K. Both PM-IRA and TPD spectra

of 100 L CO taken before and after the vacuum annealing process were found to be the same. In addition, possible contamination generated by metal carbonyls was investigated. An activated charcoal purifier was installed to the flow gas injection system and both heating and cooling cycle at 10^{-4} Torr and 100 L CO exposure after annealing at 875 K for 10 min was repeated. It was determined that both PM-IRA and TPD spectra taken with and without the purifier showed the same trends, indicating that possible metal carbonyls had negligible effects on CO adsorption.

Table 3.1 TPD spectra peak fitting results*

Desorption peaks from TPD spectra		peak at 417-425 K		peak at 470-479 K		peak at 517-521 K	
		Peak position	Area	Peak position	Area	Peak position	Area
775 K	clean-10 min	425	17.8	479.00	32.6	521.00	49.6
	30 min	420	15.4	477.00	27.3	521.00	35.7
	1 h	418	13.2	470.00	22.1	517.00	23.6
825 K	clean	422	17.8	479.00	32.6	521.00	49.6
	10 min	420	16.4	473.00	26.8	520.00	42.9
	30 min	417	7.7	472.00	19.7	518.00	29.9
875 K	clean	423	17.8	479.00	32.6	521.00	49.6
	10 min	421	9.0	473.00	17.0	521.00	23.7
	30 min	419	4.0	471.00	11.6	520.00	23.2

*The area of each peak is showing as percentage of the total area of TPD profile on the clean sample. For example: the area of peak at 420 K (after 775 K for 30 min)= (the intergral peak area of the peak at 420 K)/(the total intergral area of TPD profile on the clean sample)*100%.

3.3.5 Carbon deposition and carbon island formation

The cyclic adsorption behavior of CO observed on Pt(100) during the heating and cooling cycle experiments at pressures above 2 Torr indicated that CO dissociated at elevated temperature causing carbon deposition on the surface. Deposited carbon could block the adsorption sites and result in discrete CO molecules on the sample with weaker dipole coupling effect, thus lower vibrational frequency during cooling process [110,

132]. In particular, high adsorbate pressures (e.g. 2-100 Torr) were found to be required for carbon deposition, which is in agreement with the literature [109, 110, 132]. At high CO pressures, the Pt(100) surface can be roughened by the creation of more kink or step sites, which can facilitate CO dissociation. Carbon deposition rate might also increase significantly at higher CO pressures and temperatures, since the CO ligands on the roughened surface, Pt(CO)n, may not be stable and can initiate CO dissociation [110].

After carbon deposited on Pt surface, carbon atoms can diffuse to form islands at elevated temperature. This is verified from the constant IR absorption band and consistent thermal desorption peak positions of 100 L CO exposure to the annealed samples. From Figures 3.8-3.10, it is obvious to see the total coverage of CO on Pt surface decreased based on the area decrease in both TPD and PM-IRA spectra. However, the C-O stretching band after 100 L CO exposure remained constant after all annealing experiments, indicating that the local coverage of CO did not change on the annealed samples compared to the clean sample surface. These observations suggest that carbon deposited on the surface and diffused to form islands, which resulted in CO molecules to cluster together as close-packed islands. Our results indicated that close-packed island formation of CO mainly occurs at temperatures above 725 K with long annealing times at 100 Torr. Specifically, at 775 K, it took more than 30 min to produce significant amount of carbon islands on the surface, based on the TPD area decrease. While at 825 K, 10 min would be sufficient to grow comparable carbon islands. This is in agreement with literature, where carbon islands were reported to grow faster at high temperature than low temperature [115]. Previously, carbon accumulation was observed on Pt(100) at 500 K at pressure of 40 Torr CO [109], which temperature is much lower than 775 K in our case.

The difference in temperatures at which obvious carbon deposition occurs might be due to the difference in the number of defect sites (step or kink sites) on different samples, which could facilitate CO dissociation significantly [109, 128]. In addition, they only observed carbon species with Auger spectroscopy without any confirmation of carbon islands or not. Similarly, CO dissociation in the kinked area was observed on Pt(210) surface saturated with CO molecules, and 2D graphite islands appeared above 850 K [113]. Large graphite islands were observed on the Pt surface above 850 K due to diffusion of carbon atoms on the surface and explained by Ostwald ripening where formation of large graphite islands are more thermodynamically stable [113, 115].

On the other hand, dipole coupling simulations were performed to investigate the effect of adsorbate geometry on the observed coverage-dependent band shift. Four representative adsorbate geometries used in the simulations are shown in Figure 3.11. The maximum distance geometry and one-island geometry are the two extreme adsorbate geometries, and the random geometry and islands geometry represent the adsorbate geometries between these two extreme cases. In the maximum distance geometry, CO molecules repel each other and maximize the distance between one another. On the contrary, in one island geometry, CO molecules always adsorb next to the pre-adsorbed CO molecules forming a big island. For the random geometry, CO molecules were placed on the lattice randomly. For the islands geometry, CO molecules were allowed to cluster together such that formation of different close packed islands can take place. The stretching frequency of the ensemble was calculated as a function of coverage in small steps (0.05) up to a fully covered surface. For all the simulations, CO molecules were only allowed to adsorb onto on-top sites, and the coverage is defined as the number of

CO molecules on the surface divided by the total number of adsorption sites (platinum atoms). The surface is assumed energetically homogeneous for all the simulations.

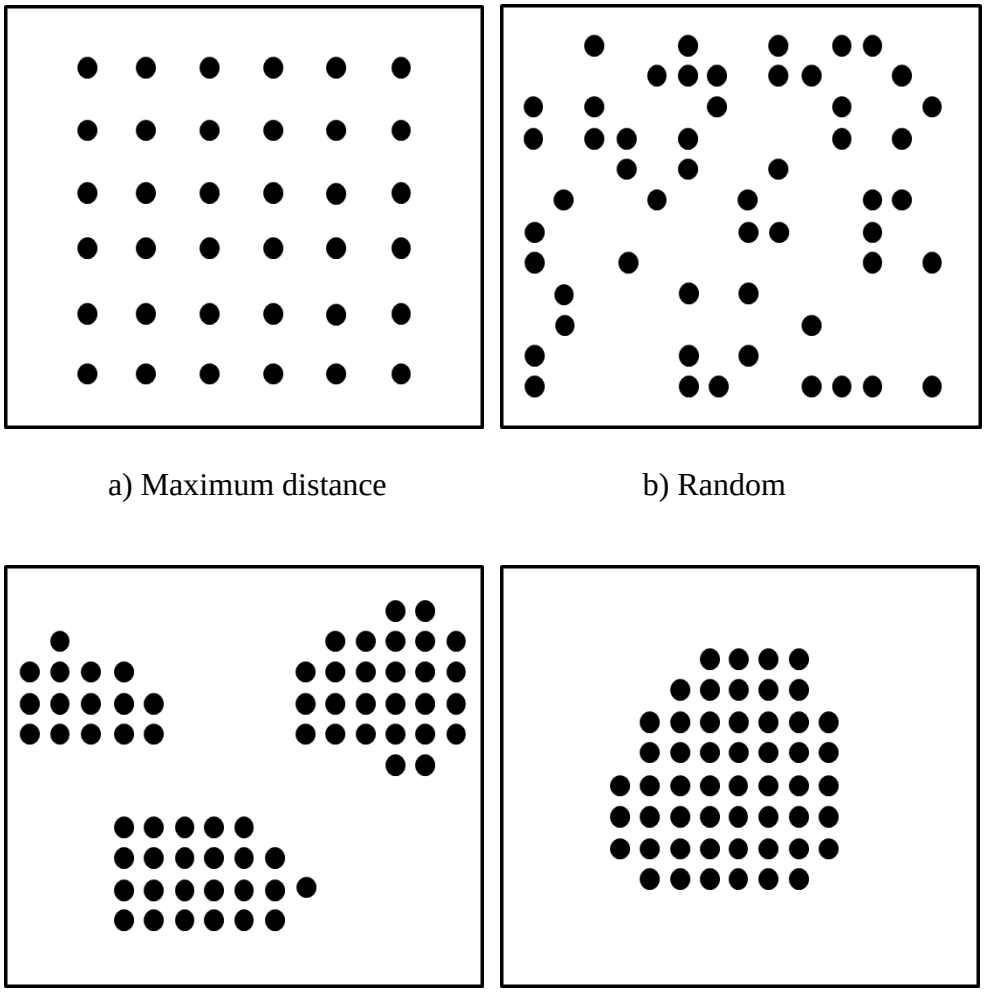

a) Maximum distance b) Random

c) Islands d) One-island

Figure 3.11: Examples of adsorbate geometries used in the dipole coupling simulations

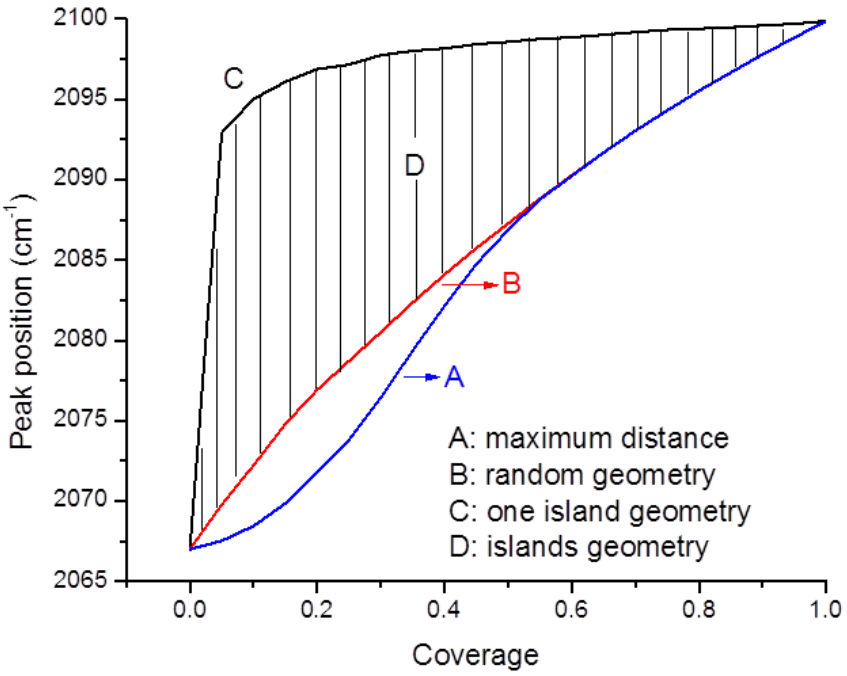

Figure 3.12: Dipole coupling simulations of CO adsorbed on Pt(100) with different geometries, region D represents all possible islands formations with different dimensions

Figure 3.12 shows the results the dipole coupling simulations. The maximum distance geometry (curve A) showed the slowest rise in peak position, and it converged with the random geometry after the surface coverage increased above 50%. Similar observation was also reported for CO adsorption on Pt(111) surface [100]. For the random geometry (curve B), the adsorption of CO molecules showed a nearly linear frequency dependence on coverage, which was also pointed out by Mahan and Lucas [126]. For one island geometry (curve C), there was a really sharp rise in peak positions up to 10% coverage and then a slowly increase as the surface became saturated. The formation of islands with different dimensions could also happen and the trend of frequency vs. coverage would locate in region D. In addition, more complicated adsorption patterns (e.g. mixture of islands and random geometries) of CO molecules on

the surface, which was not the focus of this work, could also form and could result in different frequency vs. coverage curves between random geometry and one island geometry. For all the simulations, the value of the vibrational polarizability was chosen to be 0.21 $Å^3$, and the singleton frequency was chosen to be 2067 cm^{-1} [107, 125].

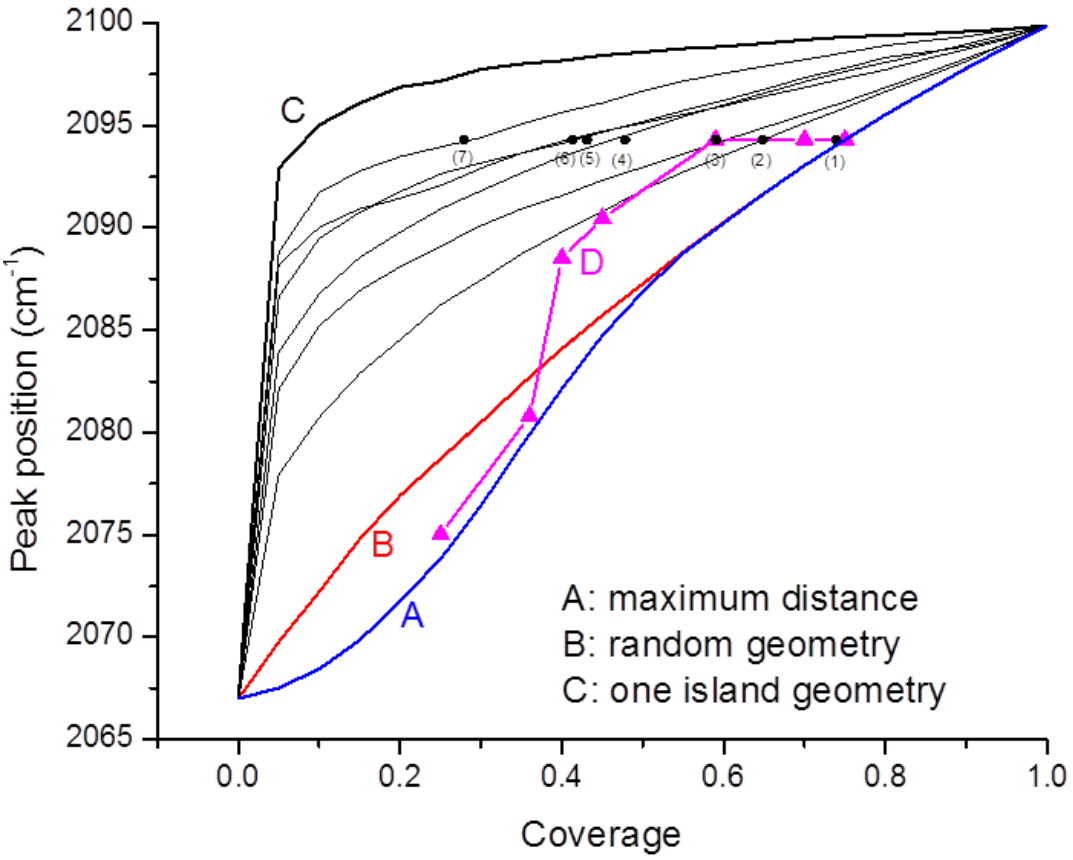

Figure 3.13: Peak position vs. coverage for CO adsorption on clean sample and annealed samples, as well as simulated CO adsorption with different adsorbate geometries. Curve D with triangular data points correspond to different exposure of CO on clean sample from 1 L (2075 cm^{-1}) to 1000 L (2094 cm^{-1}). Thermal desorption data points (filled circles) correspond to 100 L CO exposure on different samples (1), (3), (4) sample after 775 K annealing for 10 min, 30 min and 1h, respectively; (2), (5) sample after 825 K annealing for 10 min and 30 min; (6), (7) sample after 875 K annealing for 10 min and 30 min. All annealing was operated under 100 Torr CO condition to produce possible carbon deposition on the surface

Figure 3.13 shows the comparison of the experimental data and the simulation results. Curve D in figure 3.13 represents the experimentally measured vibrational frequencies of 1 L to 1000 L CO exposure on the clean Pt(100) surface as a function of the surface coverage. It was noticed that, at coverages below 0.4, the peak positions were observed between the predicted band positions of random geometry and maximum geometry, and then they were subject to island geometry at higher coverage. It is reasonable that CO molecules can adsorb randomly on distant sites of Pt surface at low CO coverage and approach island geometry as the coverage increases with more interactions between adsorbed molecules. Crossley et al. have also reported that CO molecules could adsorb on the Pt(100) surface as ordered islands as coverage increased above 0.16 [105]. They found that the island size could change from 66 CO molecules per island at 160 K to 11 CO molecules per island at 400 K, assuming that the (4x2) adsorbate structure formed within the islands [25, 104, 105]. On the other hand, the thermal desorption data for the annealed samples with carbon deposition are located in the islands region predicted from the dipole coupling model. As shown in Figure 3.13, the filled black circle data points (1)-(7) represent the vibrational frequency versus the surface coverage from the TPD results after 100 L CO exposure on the sample annealed at different temperatures and times. Although the peak positions after all annealing experiments remained constant at 2094 cm^{-1}, the relative coverages obtained from the corresponding TPD spectra on the annealed samples were found to decrease from the saturation coverage 0.77 to the lowest measured coverage 0.28 with increasing annealing temperature and time. Carbon islands formation on the annealed surface was proposed the main reason of such behavior, where the CO molecules could adsorb as islands with

similar local coverage (thus similar dipole coupling effect) and show the same vibrational frequency. It needs to be emphasized that the vibrational frequency mainly depends on the local coverage instead of the overall coverage because the long-range interaction of the adsorbates becomes negligible within the islands. Of course, the trend of islands geometry could vary with different total surface coverage of CO on the annealed samples, as seen from the individual curves that cross the thermal desorption data points (1)-(7) in Figure 3.13. Based on dipole coupling simulation, the representative images of CO islands formation on the annealed samples were obtained and shown in Figure 3.14. Each image only represents one of the possible islands geometries at the specified total surface coverage. It was demonstrated that, on the annealed samples with different carbon islands deposition, CO molecules could adsorb as islands with similar local structure.

The structure within the CO islands on the surface could be (4x2) as proposed by Broden et al [104]. Unfortunately, the detailed structure information in this work could not be confirmed directly due to the lack of structure characterization technique in the current system. At annealing temperature below 875 K with annealing time less than 1 h, the relative coverage is more than 0.45. After heating at temperature above 825 K for than 30 min in 100 Torr CO, the sample would be covered completely with carbon species and no CO adsorption could be observed. All these observations indicated that obvious carbon deposition occurred at high pressure conditions with long time heating at high temperature. It is confirmed from dipole coupling simulations that CO molecules could adsorb as islands on the annealed sample without changing local CO environment, resulting in a same vibrational frequency, 2094 cm^{-1}, at different total coverages.

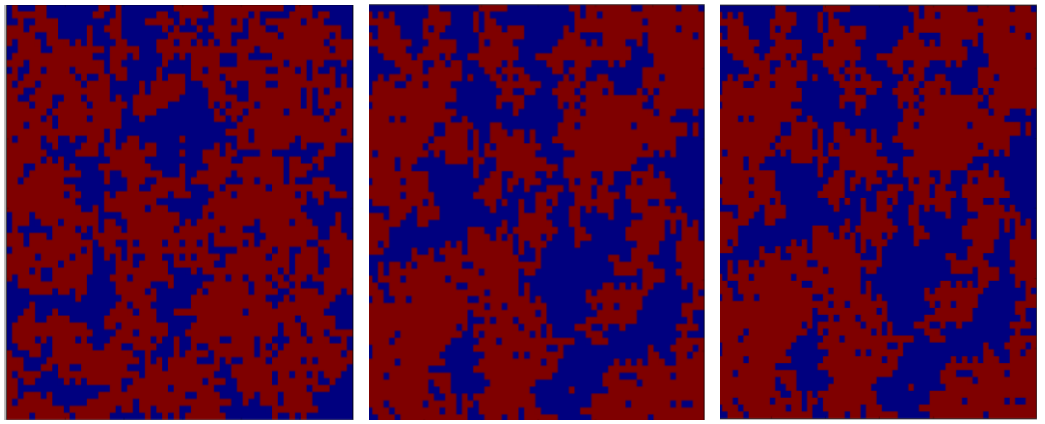

(1) θ=0.74 (2) θ=0.65 (3) θ=0.59

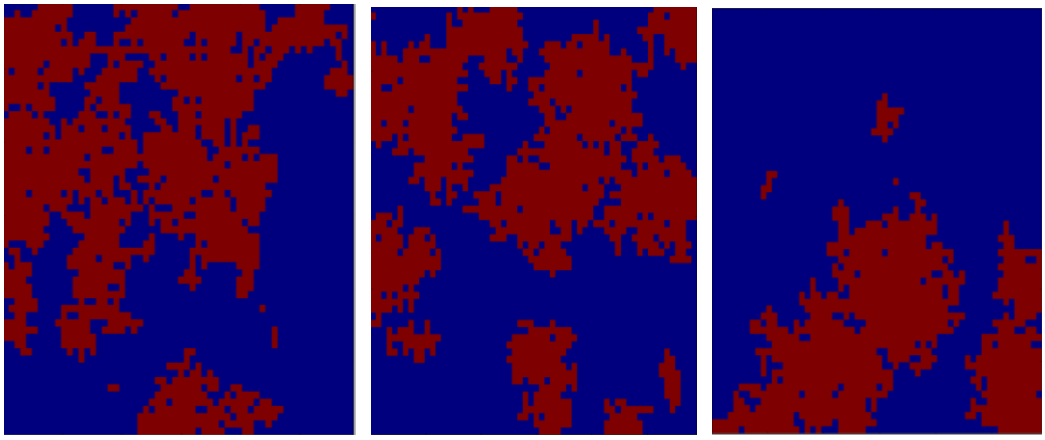

(4) θ=0.48 (6) θ=0.41 (7) θ=0.28

Figure 3.14: Representative images of the CO islands formations on the annealed samples with different surface coverages (red-CO molecules, blue-Pt substrate)

In summary, CO dissociation on Pt(100) could take place at elevated pressure condition (>2 Torr) after the sample was heated above 725 K. The deposited carbon atoms could diffuse on the surface and form islands via Ostwald ripening [113, 115], and eventually the surface could be covered by carbon islands without further CO adsorption. The whole process was proposed as the steps (a)-(d) shown in Figure 3.16.

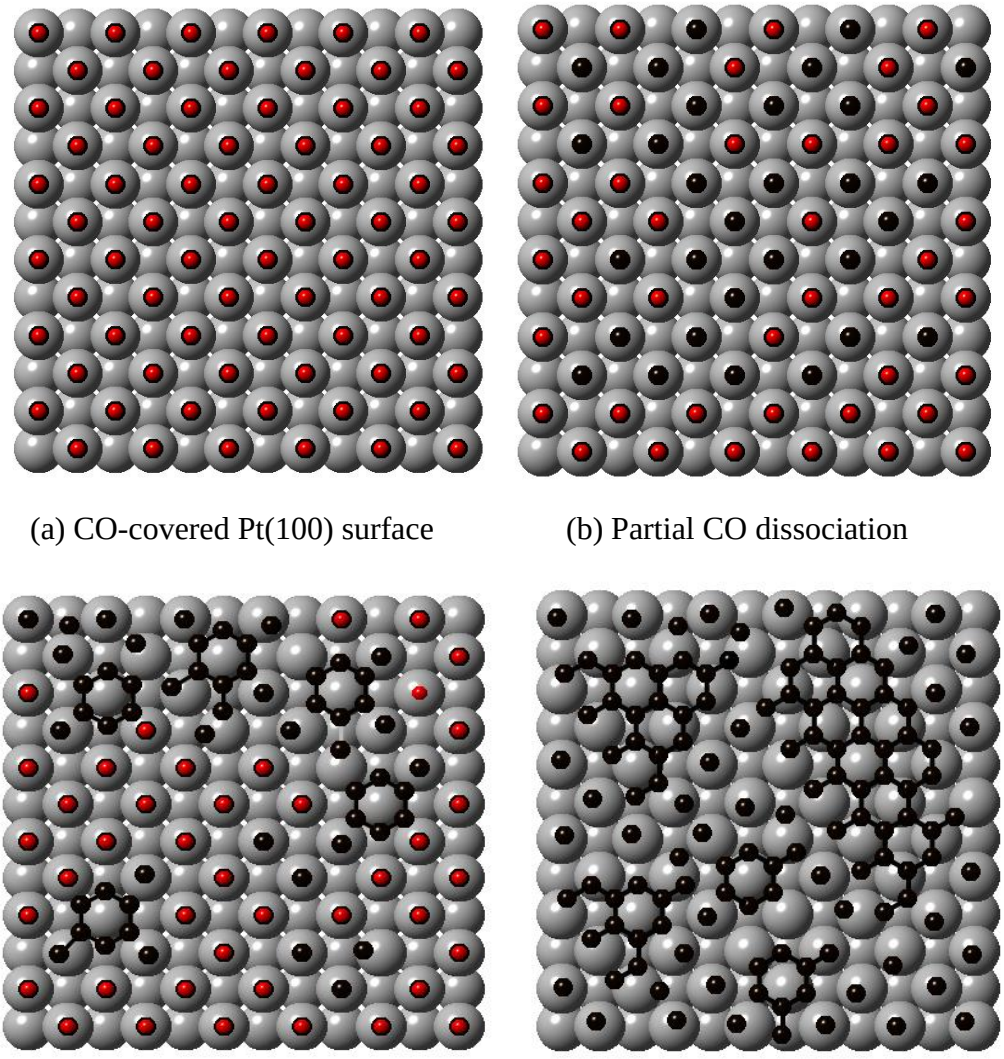

(a) CO-covered Pt(100) surface (b) Partial CO dissociation

(c) Carbon islands formation (d) Carbon covered Pt(100) surface

Figure 3.15: Representative process of carbon island growth on Pt surface after CO dissociation at elevated pressure (100 Torr) and high temperature (> 775 K), red-oxygen atoms, black-carbon atoms, grey-Pt substrate

At the beginning, the surface was completely covered with CO molecules at elevated pressure, as shown in Figure 3.15(a). After heating the sample at temperature above 725 K, CO dissociation occurred and the surface could be covered with discrete carbon atoms, resulting in weaker dipole coupling between the molecules adsorbed on the surface thus lower vibrational frequency. As time went on, e.g. more than 30 min at 775

K, carbon atoms grew into islands as shown in Figure 3.15(c). These carbon islands lead to the formation of CO islands when the annealed samples were exposed to 100 L CO. Thus, similar local coverage with these CO islands lead to the same vibrational frequency with similar dipole coupling interaction. When the sample was completely covered with carbon, no more CO could adsorb on the surface and no IR or TPD signal was observed.

3.4 Conclusions and summary

The adsorption of CO on Pt(100) was investigated from high vacuum condition to near-atmospheric pressures using a customized PM-IRAS experimental setup. The system was shown to be highly effective for detecting adsorbed surface species at near-ambient pressure conditions and can be applied to bridge the "pressure gap" between surface science and realistic industrial catalysis.

Based on experimental measurements, the saturation surface coverage of CO on the Pt(100) was calculated to be larger than 0.85 at the pressure range from 10^{-4} Torr to 300 Torr CO, which is much greater than the previously observed saturated surface coverage (0.75) under high vacuum conditions. As the sample temperature increased, a red shift of the C-O stretching band was observed due to weaker dipole coupling of fewer molecules on the surface. Heating and cooling cycles performed at pressures above 2 Torr revealed an irreversible adsorption behavior of CO due to the carbon deposition on the surface. A series of CO adsorption experiments were carried out on the sample after the sample was annealed at temperatures above 775 K in 100 Torr CO. Both TPD and PM-IRA spectra collected after 100 L CO exposure on the annealed sample indicated that

the amount of adsorbed CO molecule decreased with increasing annealing time. The C-O stretching band was found to remain at the same vibrational frequency during these experiments suggesting that CO molecules adsorbed as close-packed islands on the annealed sample with similar neighboring environment.

Dipole coupling simulations were performed to simulate the effect of adsorbate geometries on the absorbance band positions. It was determined that vibrational frequency of CO increased linearly with the surface coverage in the random adsorption geometry. In the case of the island geometry, the vibrational frequency showed a steep jump up to 10% coverage and then increased slowly as the surface approached saturation. A comparison of the experiment and simulation results revealed that CO molecules could adsorb as islands with different patterns due to the carbon deposition on the annealed sample. These findings can provide an insight into carbon deposition effects on the activity of Pt catalysts operating at high temperatures in a CO environment.

CHAPTER 4

Synthesis and Characterization of Ru/Al_2O_3 Model Supported Catalyst

It has been shown in Chapter 3 that PM-IRAS can be applied to bridge the "pressure gap" by performing experiments from UHV to elevated pressure conditions. To bridge the "materials gap", model supported catalysts which can mimic the industrial catalysts would be required. In this chapter, the synthesis and characterization of oxide film supported catalyst, Ru/Al_2O_3 are presented. First, a literature review of synthesis of model supported catalyst is introduced. Second, the synthesis and characterization of model catalysts used in this work are described in detail: (1) synthesis and characterization of Al_2O_3 thin film; (2) colloidal synthesis and characterization of size-varied Ru nanoparticles, (3) deposition of Ru nanoparticles onto Al_2O_3 support and characterization of supported Ru/Al_2O_3 catalyst. Some preliminary test on this model catalyst will be shown at the end.

4.1 Introduction

The "materials gap" originates from the fact that industrial catalysts, typically active metal particles on high-surface-area supports, have much more complicated structure than metal single crystals used in conventional surface science studies. The

small particle size and the high-surface area oxide make it typically very difficult to characterize or even detect the active metallic phase. Further complications may arise from oxide porosity and the presence of uncontrolled synthesis residues (which may either act as contaminants or promoters). Therefore, industrial catalysts are often not well suited for atomic scale studies. To overcome these limitations, metal single crystals with well-defined structure and composition are applied for surface reaction studies. However, the adsorption sites or reaction pathways may change dramatically on the industrial catalysts due to the effect of particle size or metal-support interaction. To bridge such "material gap", many studies have been carried out on model supported catalysts (e.g. nanoparticles on a thin oxide film deposited on a metal substrate), which not only can mimic the structure of industrial catalysts but also allows the use of various surface characterization techniques. With controlled catalyst structure and in situ surface species measurement, it becomes possible to elucidate the reactions mechanism at molecular or atomic level in a more industrial-relevant condition.

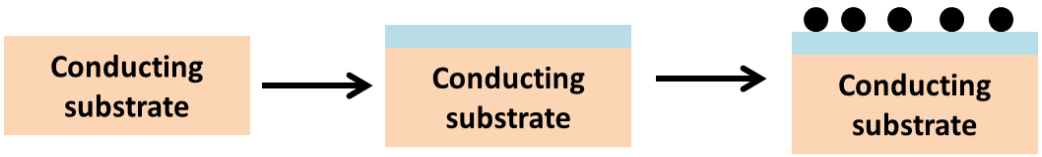

Figure 4.1: Representative schematic of model supported catalysts synthesis

Model catalysts have been introduced in the late 1960s with the development of UHV technology. Different model supported catalyst systems have been designed to understand the essential part of the catalytic systems [37, 46-49, 133]. One attractive method to make model supported catalysts is to deposit a thin layer of oxide (ideally epitaxial) on a conductive substrate, followed by the deposition of metal nanoparticles on

oxide support, as shown in Figure 4.1. The advantage of using the conductive substrate is that serious charging can be avoided even if the thin film support is an insulator, so various spectroscopic techniques such as XPS, AES, LEIS and SIMS can be used at their optimum resolution. More explanations of the characterization techniques can be found in the review articles [46, 48].

4.1.1 Synthesis of oxide thin films as model catalyst supports

Different methods have been applied to prepare the epitaxial oxide films. One way is to evaporate the bulk oxide material onto a clean well-ordered single crystal surface in a UHV system. This process is usually performed at high temperature with a low deposition rate in order to get good crystalline and stoichiometric films. MgO(111) films and ZnO(0001) films have both been obtained by this method on cleaved mica [134, 135]. Such films prepared at low temperature are highly non-stoichiometric and unstable upon annealing. An alternative method is to evaporate the metal at a partial pressure of oxygen (10^{-7}-10^{-6} Torr) at a proper temperature (200-600 K), followed by annealing at high temperature depending the oxide (600-1300 K). This method has been applied for the preparation of various oxide films, including MgO [136], NiO [137], Al_2O_3 [138-140], TiO_2 [140], SiO_2 [141, 142], etc. The annealed films are generally very stable at high temperature and there is no diffusion of the deposited metal observed below the annealing temperature. Besides the in situ evaporation/deposition method at UHV condition, thermal oxidation of a metal (or an alloy) single crystal substrate is another way to prepare epitaxial thin films. This method has been used successfully for preparing

variety of thin films, including NiO/Ni(111) [143], Al_2O_3/NiAl(110) [144, 145], Al_2O_3/Al(111) [146], TiO_2/Ti(0001) [147], ZnO/Zn(0001) [148] and MgO/Mg(0001) [149]. The films made this way are typically ultrathin (a few to ten layers) and well ordered (based on LEED measurement). The main limitation is that the metal deposits are not stable upon heating and they may diffuse during experiments. Increasing the film thickness may decrease the metal diffusion effect. The geometrical structure of the metal oxide film can be characterized via LEED, Small Angle X-ray Diffraction (SAX) or TEM (diffraction mode), and the surface morphology information can be obtained via SEM, AFM or STM.

4.1.2 Deposition of metal particles on thin film support as model catalyst

Once a suitable model support has been prepared, the catalytically active particles can be deposited onto the surface via different methods. Direct physical vapor deposition (PVD) of a metal onto the model support is the most convenient and most often used technique. The particle size is dependent of the nucleation and growth process, during which the metal flux, substrate structure (smooth, homogeneous or defects), substrate temperature and other parameters (such as heat of adsorption of the metal on the substrate) are important. Evaporating devices for vacuum application are commercially available or can be constructed relatively easily, and different model catalysts can be synthesized via PVD technique. The nucleation and growth of different metals, such as Rh, Pd, Co, Pt and V, has been documented in a review paper [133]. The concentration of deposited particles can be characterized by Rutherford Backscattering Spectroscopy (RBS), LEIS,

XPS or AES. The disadvantage of PVD method is that the particle size has a broad distribution, especially if the homogeneous nucleation mechanism occurs [46].

Another method to deposit metal particles is chemical vapor deposition (CVD), during which process the metal precursor (usually carbonyl or allyl complex of the metal) is evaporated and exposed to the substrate under vacuum condition. After exposure of the metal precursor, the model catalyst is usually heated in vacuum with hydrogen to remove the ligands and to reduce the metal particles. This method requires the metal precursor having a relative high vapor pressure at room temperature. It has been used to prepare several model supported catalysts, such as TiO_2 and Al_2O_3 supported rhodium [150, 151], Al_2O_3 supported cobalt [152, 153] and MgO supported rhenium [154]. Besides the PVD and CVD method, atomic layer deposition or lithography have been applied for model catalysts synthesis as well [46].

Last but not least, wet chemical impregnation, the widely accepted method used in industry, has also been applied to deposit metal particles onto model catalyst supports. This method is based on the chemical interaction of metal complex and hydroxyl groups on the oxide support surface. The model support is often carefully rinsed with solvent. Typically, after impregnation, drying, and calcination, the catalyst is further activated by reduction in hydrogen or sulfidation in H_2S for different applications. Various model catalysts have been synthesized using wet chemical method, including silica supported vanadia [155], iron oxide supported Pd [43], and alumina supported Pt [40] and Rh [45, 156] catalysts. As a well-known technique for the preparation of thin uniform films, spin coating has also been applied to prepare model supported catalysts, which was first recognized and developed by Kuipers and coworker [39]. Accurate prediction of the

deposited metal can be modeled straightforwardly for the spin coating process [39, 157, 158]. Langmuir-Blodgett (LB) method and Dip coating approach can also be used for the deposition of metal particle onto model oxide supports [159, 160]. Similarly, the concentration of metal particles on the model supports can be measured via RBS, XPS, AES or LEIS technique, and the morphology can be characterized using AFM or SEM when the particle size is sufficiently large. TEM can be applied to characterize model catalysts if one used specially prepared sample with windows such that they are sufficiently transparent to the electron beam [46]. Wet chemical impregnation is the most industrial-relevant approach and is highly valuable for model catalysts preparation for surface science studies. Better understanding of heterogeneous catalysis at atomic or molecular scale will be obtained via the investigation of surface reactions on model supported catalysts prepared using this method.

In this work, Ru nanoparticles of different sizes that are prepared via colloidal synthesis method are deposited onto Al_2O_3 thin film support via wet impregnation method as model supported catalysts. These model catalysts provide the opportunity to study the size effect of Ru particles on different reactions, such as CO oxidation and ammonia decomposition. Through the surface science studies on the model catalysts from UHV to elevated pressures in the PM-IRAS system, the surface chemistry of different reactions at more industrial-relevant conditions can be revealed.

4.2 Experimental methods

There are several considerations need to be addressed before the introduction of model catalyst synthesis: (1) the metal substrate need to be able to stand the heating process during the model catalyst synthesis and later-on experiments (ideally refractory metals, e.g. Mo), (2) the metal substrate need to be (nearly) inactive for the reaction studied such that the performance of active metal particles can be interpreted straightforwardly, (3) the Al_2O_3 film with defined structure (such as pure α-like or pure γ-like structure) are preferred since the catalytic activity of supported catalysts may change with the crystallography structure of Al_2O_3 crystallites, (4) IR reflectance of the model support need to be good enough for satisfactory measurements during experiments. Other parameters, such as the morphology and thickness of the oxide film, can also influence the model catalyst performance and need to be considered as well. The synthesis and characterization of Al_2O_3 thin film, Ru nanoparticles, and supported Ru/Al_2O_3 catalysts are introduced respectively.

4.2.1 Synthesis of aluminum oxide film

Aluminum oxide is widely used as catalyst support in technological applications. Different types of flat aluminum oxides have been applied as model supports: single crystal α-Al_2O_3 [152, 153, 161, 162]; thermally oxidized aluminum single crystals [146, 151, 163, 164], aluminum-based alloy [133, 144, 145, 165-167], aluminum foils [38, 41, 168-170], and evaporated films [171-174]; anodized films [175-177]; and films made by reactive evaporation [138, 178-180]. Single crystalline α-Al_2O_3 has been often used as

model catalyst support due to its high mechanical and thermal stability. Extensive studies have also been performed on the oxidation of aluminum substrate and some aspects of alumina thin film growth are still open to discussion. It is generally accepted that low temperature (< 650 K) oxidation in air or in UHV leads to the formations of amorphous alumina, and oxidation at temperatures of 700-1000 K leads to the formation of γ-Al_2O_3 crystals. Reactive evaporation of aluminum in oxygen environment is another method applied to grow Al_2O_3 films on different substrates. Typically, the films deposited in 10^{-7}-10^{-6} Torr O_2 environment are heated with or without O_2 to 870-1000 K to form γ-like alumina [139].

In this work, two different methods were utilized to make alumina thin films: reactive magnetron sputtering deposition and thermal oxidation. The synthesized alumina films are characterized by XRD, Raman, SEM, and TEM techniques.

4.2.1.1 Sputtering deposition of aluminum oxide film

Sputtering is a technique used to deposit thin films of a material onto a substrate. By first creating gaseous plasma and then accelerating the ions from this plasma into the target (e.g. Al), the target material is eroded by the arriving ions via energy transfer and is ejected in the form of neutral particles - either individual atoms, clusters of atoms or molecules. These ejected neutral particles will travel until they come into contact with something (other particles or a nearby surface). When a substrate is placed in the path of these ejected particles, the substrate will be coated by a thin film of the target material. When the sputtering deposition is performed in oxygen environment (referred as

"reactive sputtering"), oxide films will form on the substrate. Thin oxide films with desired structure can be made by tuning the deposition parameters, such as cathode voltage, oxygen flow rate, substrate temperature, and post deposition heating treatment. It needs to be pointed out that the same deposition parameters do not necessarily lead to the same deposition results on two different sputtering systems, due to the possible change of the chamber configuration (e.g. pumping configuration, gun arrangement, and temperature monitor system). Thus, it is quite important to establish the basic deposition parameters in each individual sputtering system before a routine deposition is applied for the deposition of desired films.

Sputter deposition of alumina has attracted much attention in coating technology area due to its high performance in wear and corrosion protection, diffusion barrier applications and microelectronics [181, 182]. It is often reported that PVD Al_2O_3 coatings are amorphous at low deposition temperatures, whereas high temperature around 700 - 1000 K leads to the formation of γ-Al_2O_3. In addition, α-Al_2O_3 can be deposited by RF sputtering technique at substrate temperature of 1373 K and by pulsed magnetron sputtering technique at much lower temperatures. Various types of sputtering techniques have been applied to investigate the deposition of aluminum oxide: balanced magnetron sputtering (RF/DC), pulsed magnetron sputtering (RF/DC), unbalanced magnetron sputtering, closed-field unbalanced magnetron sputtering [183]. However, there are very few applications of alumina films made via sputtering deposition in catalysis or surface science area. Fuchs *et al* investigated the stability of vapor grown Pd particles supported on amorphous alumina which was made via reactive sputtering, and it was suggested that the reliability of TEM analysis with respect to the determination of particle density and

particle sizes requires a fixing layer, such as SiO_x [184]. Similarly, Matolín *et al* studied the Pt-doped CeO_2 thin film catalysts prepared by magnetron sputtering technique and revealed that the oxidation state of Pt in the CeO_2 film catalysts is significantly influenced by the substrate [185].

In this work, reactive magnetron sputtering depositions of aluminum oxide films are performed in oxygen environment in an AJA International sputtering system. As shown in Figure 4.2, once the Ar ions are generated, they are pulled by the electric field toward the target surface (e.g. Al), and then target atoms are ejected and travel to the substrate forming the coated film. With oxygen in the environment, the target atoms will bond with oxygen atoms and form oxide film on the substrate. The structure of the film deposited is affected by the power, or the energetics of the ejected atoms, the oxygen concentration, and the substrate temperature, etc. In magnetron sputtering, a magnetic field configured parallel to the target surface can constrain secondary electron motion to the vicinity of the target. The magnets are arranged in such a way that one pole is positioned at the central axis of the target and the second pole is formed by a ring of magnets around the outer edge of the target. Trapping the electrons in this way substantially increases the probability of electron-atom collision occurring. The increased ionization efficiency of a magnetron results in a dense plasma in the target region. Thus, higher sputtering rate, therefore higher deposition rate can be achieved due to the increased ion bombardment of the target. In addition, the increased ionization efficiency in the magnetron mode allows the discharge to be maintained at lower operating pressures (typically, 10^{-3} mbar) and lower operating voltages (typically, 500V, compared to 2-3 kV) than is possible in the basic sputtering mode [183].

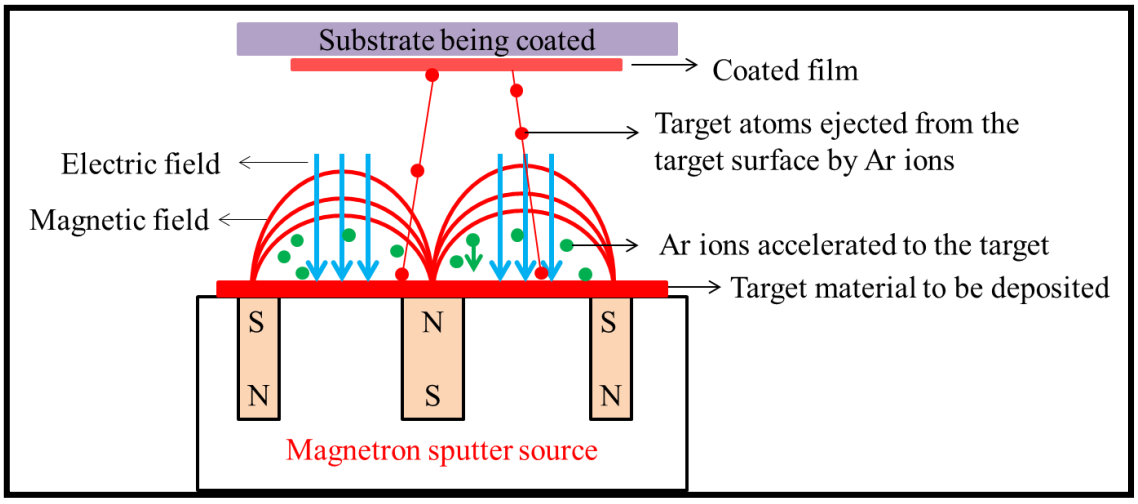

Figure 4.2: Schematic of magnetron sputter deposition

Following the work done by Goodman and Yates' group [136, 138, 141], Mo foil was chosen as the metal substrate on which alumina are to be deposited. Prior the deposition on Mo substrate, some preliminary tests were performed on Si(100) wafers. These experiments not only served as a benchmark of the reactive sputtering deposition process in AJA sputtering system, but also provided some basic understanding of the deposited films with different characterizations. The film thickness was measured by Filmetrics F20 thin film analyzer, which is based on the optical interference effects in the UV-visible spectrum originated from the in-phase or out-of-phase reflectance from the top and bottom interfaces of the thin film. The crystalline structure of the thin film was analyzed by XRD and Raman, and the surface morphology was characterized by SEM.

4.2.1.2 Thermal oxidation method for alumina film formation

Another method that is applied to make alumina thin film is thermal oxidation, following the work done by Ealet *et al* and Matolin et al. [170, 186]. Typically, the cleaned aluminum substrate was heated in air at 900 K for 12 h and cooled to room temperature, forming a thin layer (10-50 nm) of γ-like alumina. This method is simple and easy to apply, except that the surface is not as smooth as that from sputtering deposition. In this work, high-purity aluminum foil (99.998% Alfa Aesar) was cut into 1x1 cm^2 squares for sample preparation. The substrate was cleaned with NaOH solution and rinsed with DI water before to be heated at 900 K for 12 h. After thermal oxidation, the sample was characterized with XRD, Raman, SEM and TEM.

4.2.2 Colloidal synthesis of Ru nanoparticles

Ruthenium catalysts have been investigated extensively in the past due to its importance in different reactions, such as ammonia synthesis and decomposition, CO oxidation, and Fischer-Tropsch synthesis, etc [25, 187-191]. Colloid chemistry method has been applied successfully for the synthesis of Ru nanoparticles. For example, mono-dispersed Ru nanoparticles can be obtained by reduction of $RuCl_3$ or $Ru(NO)(NO_3)_3$ in glycols [192-196]. The glycol used, usually ethylene glycol (EG), can act as both a solvent for the metal salt and the reducing agent and growth medium for the metallic product. The steric or electrostatic stabilization is achieved in different ways, for instance by addition of polyvinylpyrrolidone (PVP) or by sodium acetate [197]. Generally, the metal precursors are mixed with the reducing agent, and the metal ions are reduced to

metallic state forming nanoparticles under proper heating treatment, during which process the stabilizing agent will prevent the undesired agglomeration and facilitate well dispersed metal nanoparticles, as shown in Figure 4.3.

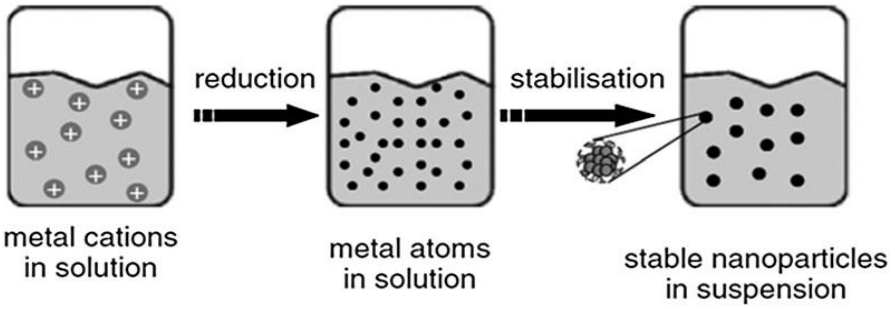

Figure 4.3: Formation of nanoparticle via reduction of metal salt precursors [198]

In this work, Ru nanoparticles were synthesized via $RuCl_3$ precursor which was dissolved and reduced in EG with PVP as the protective agent. Typically, appropriate amount of $RuCl_3$ (Strem Chemicals, Anhydrous) was dissolved in 15 mL EG (Sigma-Aldrich, 99.8% anhydrous) at room temperature, and 185 mg of PVP (Sigma-Aldrich, MW: 55,000) was added as the stabilizer before the solution was heated to the desired temperature (180 °C and 150 °C). The mixture was heated at the maximum temperature for 2 h under continuous stirring condition and then cooled to room temperature in air. Typically, high reduction temperature leads to fast formation of more metal nucleis, thus small nanoparticles. Another factor that influences the nanoparticle size is the polymer concentration: the high the polymer concentration thus the better the stabilization, the smaller are the metal nanoparticles [197]. The reduction temperature and concentration of $RuCl_3$ were changed to make size-varied Ru nanoparticles. In addition, Ru nanoparticles seeds were used to make large particles.

4.2.3 Deposition of Ru nanoparticle on aluminum oxide support

As mentioned, the model supported catalyst of Ru/Al_2O_3 was prepared via wet deposition of Ru nanoparticles onto the oxide support, followed by the cleaning procedure to remove the possible organics. In general, several drops of synthesized Ru nanoparticles were deposited on the oxide support followed by the addition of acetone to release the Ru particles from the protective agents, and then the sample was further cleaned in the UVO cleaner for 3 h before it was tested in the vacuum chamber. To alleviate the organic contamination from the synthesis solution, different cleaning procedures were also tried out before the Ru solution was dropped on to the support., including hot water cleaning [199], and acetone cleaning followed by UVO treatment [200]. For the hydrothermal method, the solvent was added to hot water (90 °C) under stirring condition and kept stirring for 2 h. The Ru nanoparticles were then extracted via sonication and centrifugation before they were redispersed in ethanol for use. In the UVO method, the Ru nanoparticles were mixed with acetone and sonicated for 1 h before their centrifugation. The extracted Ru nanoparticles were redispersed in ethanol and then deposited on the support, after which process 1 h UVO cleaning was performed. The synthesized model catalysts were characterized with XPS and tested with DRIFTS before it was loaded into the vacuum chamber for systematic studies.

4.3 Results and discussion

4.3.1 Sputtering deposition of aluminum oxide thin film

Alumina can exist in different crystal phases (e.g. γ-, δ-, θ-, α-), and γ-Al_2O_3 is used widely as a support due to its high specific surface area (100-300 m^2/g). It would be ideal to get pure γ-Al_2O_3 via sputtering deposition such that the model catalyst can represent the technical catalysts in a more relevant way. It has been reported that γ-Al_2O_3 can be deposited by magnetron sputtering techniques at various process conditions depending on the system utilized [182, 201-205]. The crystalline structure of the film is affected by different parameters, such as the process condition, the substrate temperature, and the post-deposition heat treatment, etc. According to the work done by Cremer *et al* [182, 201], both RF and DC magnetron sputtering of aluminum with optimal oxygen flow rate can achieve crystalline γ-Al_2O_3 films. At low oxygen flow rate, the deposited film will be composed of both metallic aluminum and γ-Al_2O_3, whereas high oxygen flow rates lead to the deposition of amorphous alumina. In addition, non-optimal conditions with high oxygen flow rates can cause possible target poisoning by forming an oxide layer on the target surface, which not only decreases the deposition rate but also results in possible arcing effect during deposition. Inverted cylindrical magnetron sputtering [202], ionized magnetron sputtering [203], dual magnetron sputtering [204], and pulsed RF magnetron sputtering [205] techniques were also applied to deposit γ-alumina thin films at different conditions. Considering the similarity of the sputtering system, the deposition conditions were chosen identical to that in the studies of Cremer *et al* [182, 201].

In the AJA International magnetron sputtering system, the depositions of γ-alumina films on Si wafer were performed in both DC and RF magnetron sputtering mode at room temperature and 500 °C. Typically the chamber pressure was controlled at 5 mTorr with Ar flow rate at 30 sccm. The O_2 flow rate was adjusted in the range of 2-5 sccm to achieve the optimal deposition condition. The film thickness was varied from several tens nanometers to several microns. Unfortunately, there was no satisfactory pure γ-alumina films deposited with the current magnetron sputter system based on the structure characterizations with XRD and Raman spectroscopy. The film was either a mixture of amorphous aluminum oxide and metallic aluminum or a mixture of meta-stable phase of aluminum oxide after sputter deposition. In addition, post-deposition heating treatment at temperature range 500-700 °C resulted in a mixture of amorphous alumina and γ- and δ- crystalline alumina phases. To avoid the possible experiment inconsistency that might generate from the alumina film without well-defined structure, the post-deposition heating treatment temperature was raised up to 1100 °C, at which temperature alumina could transfer from γ- or θ- phase into highly stable pure α- phase [204]. Even though α-alumina is not the widely used technical catalyst support, it is still a good candidate for model catalyst support, considering its high thermal stability and inertness to most catalytic reactions.

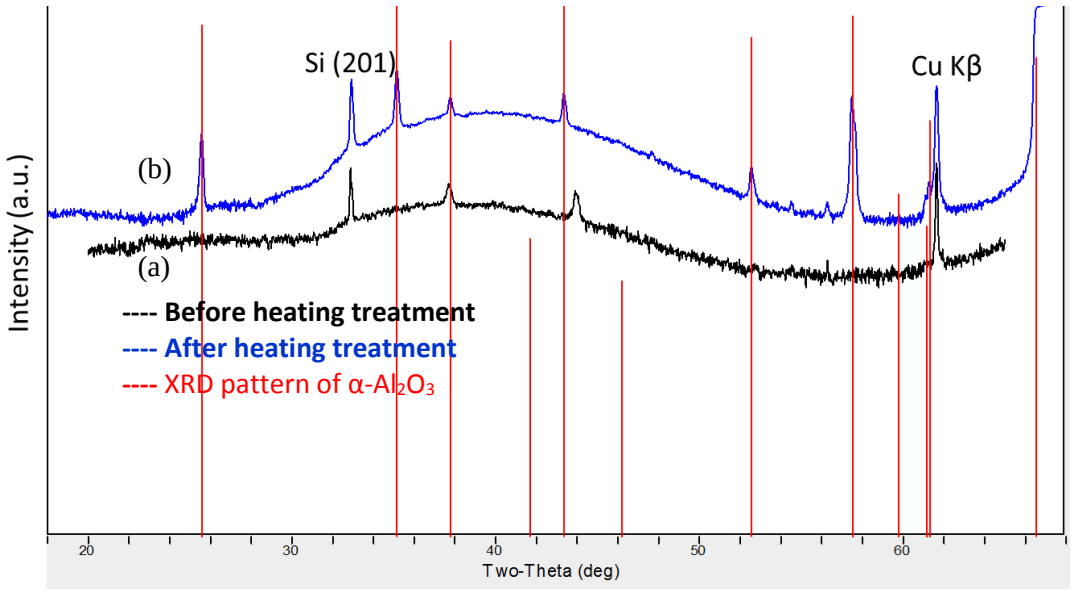

Figure 4.4: XRD patterns of 1.5 µm thick Al_2O_3 film deposited on Si wafer: (a) before heating treatment, (b) after heating treatment, and the reference pattern of α-Al_2O_3

As shown in Figure 4.4, amorphous alumina is observed from the XRD pattern without any crystalline peaks. After 12 h post-deposition heating treatment at 1100 °C, perfect pattern of α-Al_2O_3 is observed in the XRD spectra. Similarly, the fluorescence effect of α-Al_2O_3 was observed during Raman spectroscopy characterization of the sample after the heating treatment, as shown in Figure 4.5. It is clearly demonstrated that the post-deposition heating treatment can lead to the formation of α-Al_2O_3 on Si substrate. This procedure is also applied on the alumina thin film samples with Mo substrate and the results are discussed below.

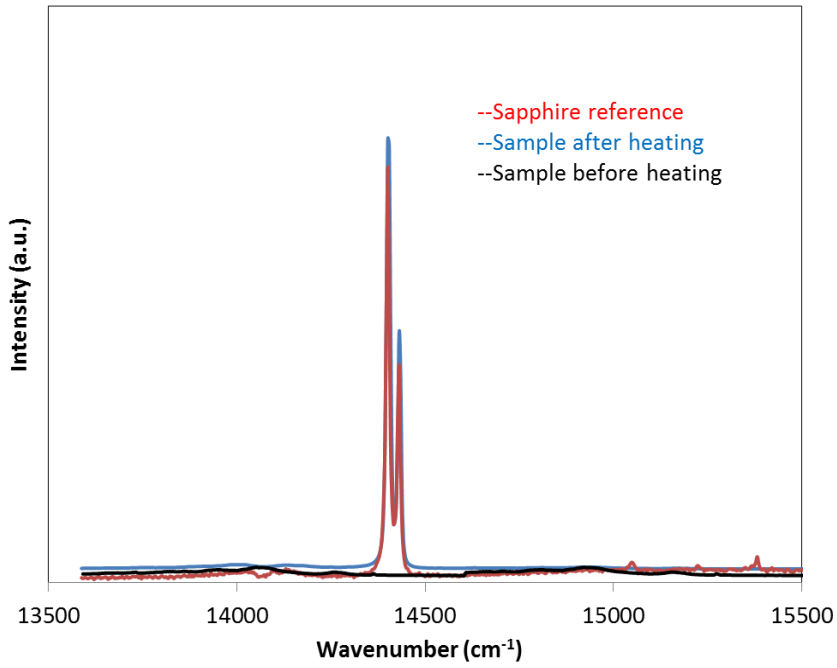

Figure 4.5: Fluorescence of 1.5 µm thick Al_2O_3 film and a sapphire reference sample

After the successful deposition of α-Al_2O_3 thin film on Si wafer, similar deposition condition and post-deposition heating treatment were applied to make α-Al_2O_3 film on Mo substrate. However, the sample vanished after the heating treatment in air at 1100 °C after 12 h. It was turned out that during the heating process Mo could be oxidized into MoO_3 at around 600 °C, which has a low melting point at 795 °C. After long time 1100 °C heating treatment, the sample just evaporated. It is possible to avoid this problem by annealing the sample in a vacuum chamber. However, the current sputter system cannot achieve temperature above 600 °C. An alternative way to solve this problem is to use a conductive substrate that can stand high temperature treatment in air.

Inconel 600 was chosen as the new substrate due to its high stability in the heating treatment in air. After Al_2O_3 thin film (500 nm) was deposited on Inconel substrate, the sample was heated in a tube furnace at 1100 °C for 12 h and clear diffraction peaks of α-Al_2O_3 were observed in the XRD spectra, as shown in Figure 4.6. In addition, peaks corresponding to Cr_2O_3 and Ni from the substrate were also observed in the XRD pattern. This is not surprising because X-ray has a big penetration depth (up to several microns) and the alumina thin film is only 500 nm thick. Raman spectra as shown in Figure 4.7 also indicated that α-Al_2O_3 was formed on the Inconel substrate. The reflectance of the sample was checked with DRIFTS instrument and the signal was comparable to that with original mirror in the instrument, indicating its good reflectivity suitable for PM-IRAS experiments. After these characterizations, the synthesized model catalyst support α-Al_2O_3/Inconel was loaded into the vacuum chamber for preliminary test--ammonia adsorption test.

Figure 4.6 presents the XRD patterns of α-Al_2O_3/Inconel sample before and after the ammonia adsorption experiment in the vacuum chamber. It is obvious that the peaks corresponding to α-Al_2O_3 are significantly attenuated after the experiment (including annealing, sputtering and exposure to ammonia), while the peaks assigned to Cr_2O_3 become dominant. However, α-Al_2O_3 still exists on the sample surface, supported by the fluorescence signal in the Raman spectra shown in Figure 4.7.

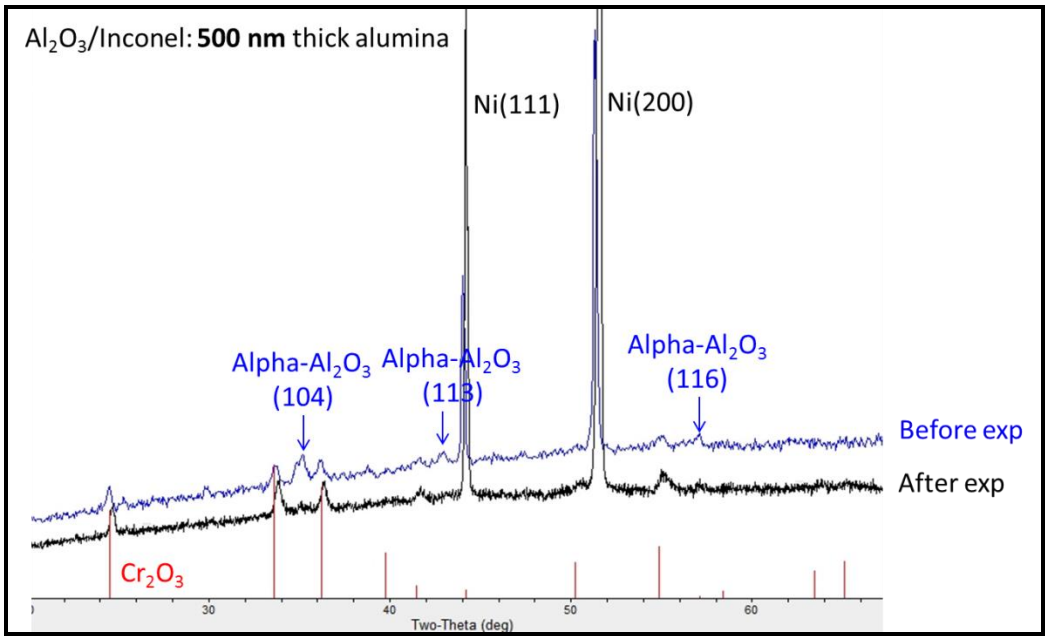

Figure 4.6: XRD pattern of Al_2O_3/Inconel sample before and after the ammonia adsorption experiment in the vacuum chamber (alumina signal attenuated)

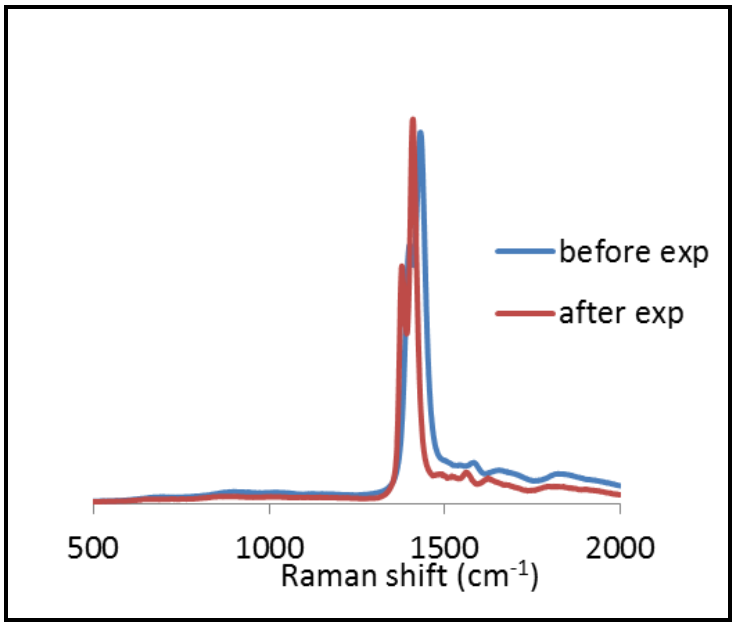

Figure 4.7: Raman spectra of α-Al_2O_3/Inconel sample before and after ammonia adsorption test in vacuum chamber (clear fluorescence signal of α-Al_2O_3 on both sample)

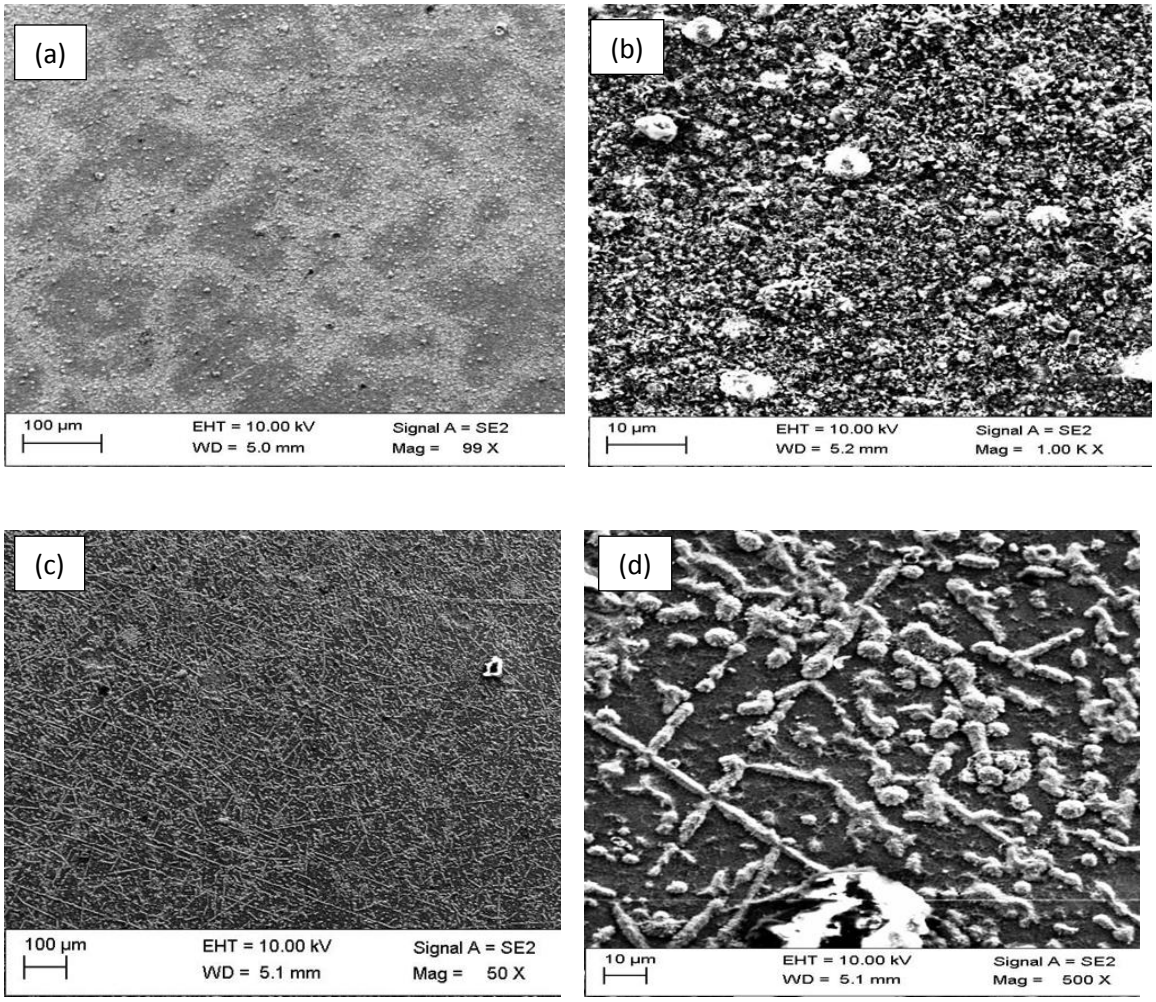

Figure 4.8: SEM images of α-Al_2O_3/Inconel sample before (a)(b) and after (c)(d) ammonia adsorption test in vacuum chamber

To understand what happened on the sample, SEM/EDX characterizations were performed before and after the sample were tested in the vacuum chamber. From the SEM images in Figure 4.8, it is noted that, the sample surface looks homogeneous before the experiments (Figure 4.8 (a)(b)), while rod-like and spherical particles appeared on the surface after the experiments (Figure 4.8 (c)(d)). To identify these new generated particles, EDX mapping were performed and the results are shown in Figure 4.9. It is

clear that these new rod-like and spherical features are due to the aggregation of Cr oxide species on the surface. It is known that Cr- species are highly volatile and can diffuse to the surface of Cr-containing materials at high temperature [206]. It has been reported that the Cr- species can be extracted to the surface under reducing environment [207]. Therefore, these new particles are possibly formed during the annealing process or the ammonia adsorption test.

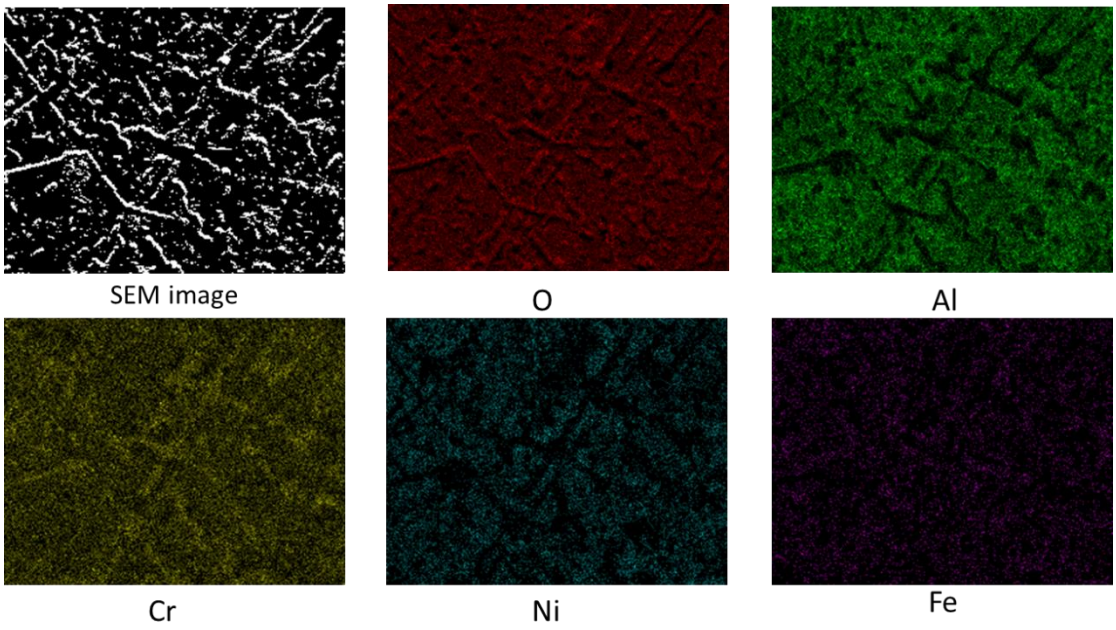

Figure 4.9: EDX mapping of the α-Al_2O_3/Inconel sample after vacuum chamber test

To prevent this Cr diffusion problem, thicker alumina films were deposited on Inconel substrate. A layer of aluminum metal was also deposited between the Inconel substrate and the Al_2O_3 thin film to mitigate the possible diffusion. However, after the heating treatment, severe cracks were observed on the sample surface, as shown in Figure 4.10. Slow heating and cooling rate (2 °C/min) for the heating treatment process did not

improve the result. This is probably due to the mismatch of the lattice of the Al_2O_3 thin film and the Inconel substrate. A proper substrate would help mitigate this cracking issue.

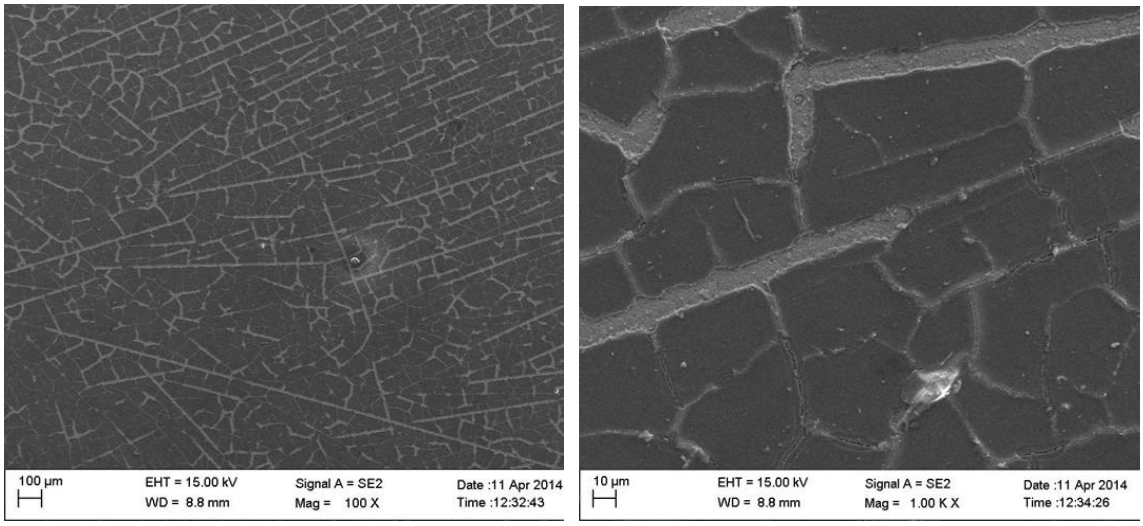

Figure 4.10: SEM images of 2µm thick alumina deposited on Inconel after heating treatment (black area is Al_2O_3)

In summary, there are some challenges in making pure γ–Al_2O_3 thin film directly from the current magnetron sputter system with/without post-deposition heating treatment. More experiments are required to find the optimal sputter deposition condition for success deposition of γ–Al_2O_3. On the other hand, with post-deposition heating treatment, it is possible to get pure α–Al_2O_3 thin film. The big challenge for making α–Al_2O_3 thin film is to prevent possible film cracking or diffusion of the element in the substrate during the high temperature heating treatment. This would require a good lattice match of the substrate and the alumina film. A single crystal substrate such as NiAl(110) would be the potential candidate [144, 145].

4.3.2 Aluminum oxide film formation via thermal oxidation

While complicated issues exist in the deposition of pure-phase alumina thin film through magnetron sputtering deposition technique, thermal oxidation method was also applied following the work by Ealet *et al* and Matolin *et al* [170, 186]. After thermal oxidation, the sample was characterized with XRD, Raman, SEM and TEM.

As expected, there was no diffraction pattern of alumina observed in the XRD spectra, since the film thickness is only about 10-50 nm. Interestingly, the preferential orientation of the aluminum substrate was observed after the thermal treatment. As shown in Figure 4.11, the original substrate has major planes of (111) and (200), while the planes of (200) becomes dominant after the thermal treatment due to the reconstruction of aluminum substrate [208]. Raman spectra showed no signal of the oxide thin film, which is consistent with literature report of Raman spectra of γ-alumina [209]. The SEM images in Figure 4.12 show the surface of the sample is not ideally smooth. To confirm the structure of the thin oxide film, TEM is applied to check the diffraction pattern of the thin film after it is etched off from the substrate. As shown in Figure 4.13, the mean grain size of the film is in the range of 50-100 nm, which is well suited for selected area diffraction. The diffraction pattern is shown in Figure 4.14, and the rings are indexed by measuring their radial distance, R, from the caustic spot (center of the image). The equation for d-spacing in a crystalline lattice is:

$$d_{hkl} = \frac{\lambda * L}{R_{hkl}}$$

Where λ is the wavelength of the electrons and L is the camera length. There is a well agreement between the measured d-spacing and the calculated d-spacing, indicating that γ-alumina is formed after thermal oxidation of aluminum substrate. The reflectance of the thin film was tested with DRIFTS instrument and it was confirmed that the thin film support is good for IR reflectance measurement.

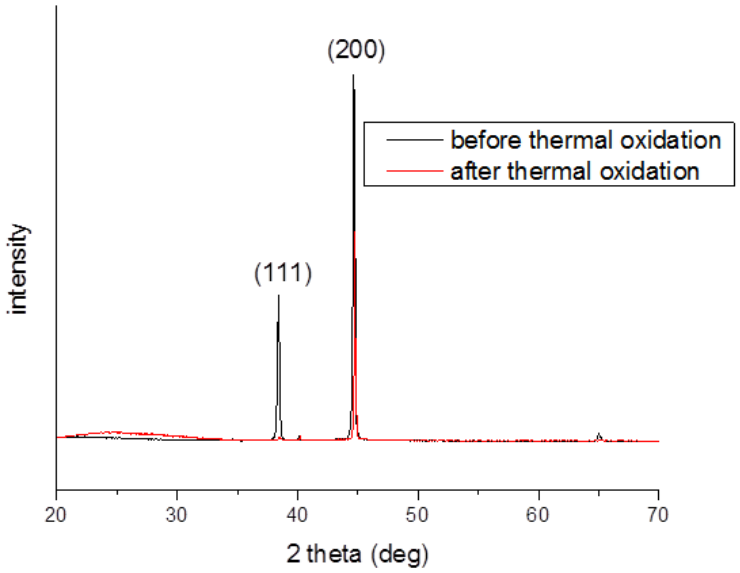

Figure 4.11: XRD pattern of Al substrate before and after thermal oxidation

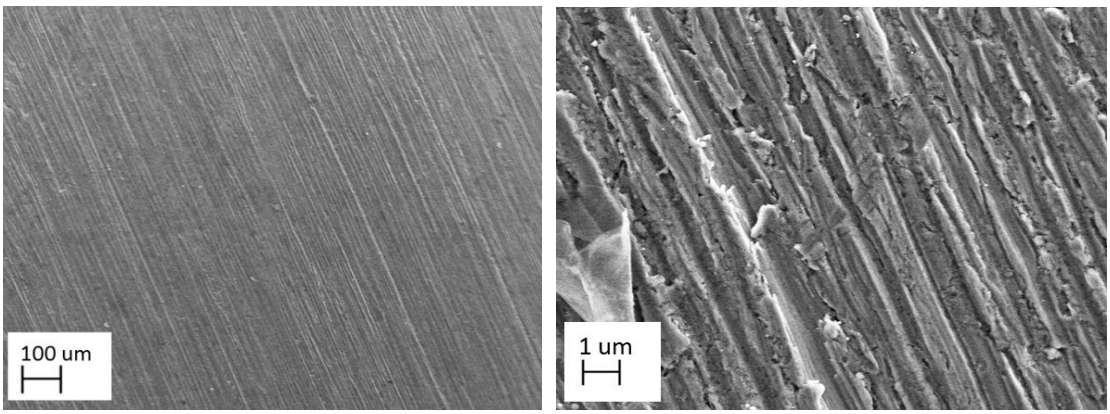

Figure 4.12: SEM images of Al_2O_3/Al after thermal oxidation of aluminum substrate

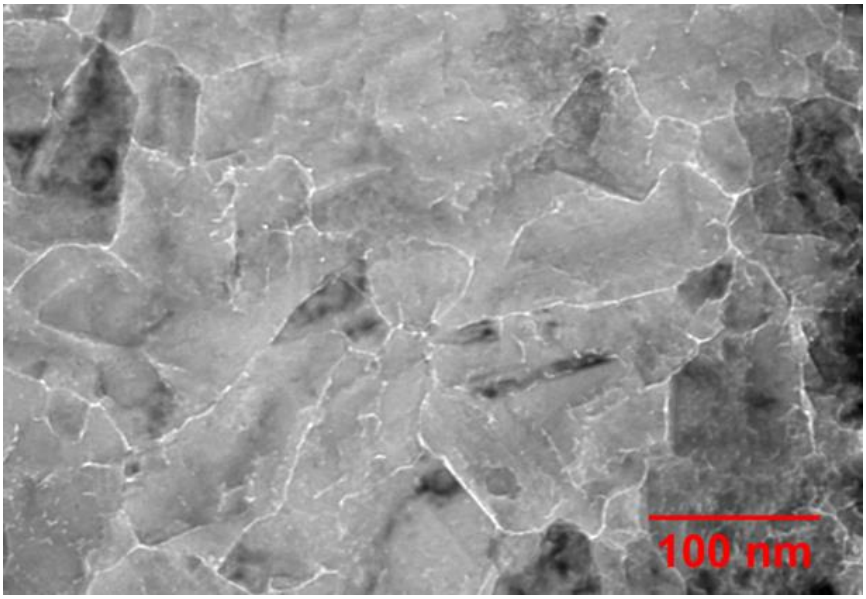

Figure 4.13: TEM image of alumina film etched off from the aluminum substrate

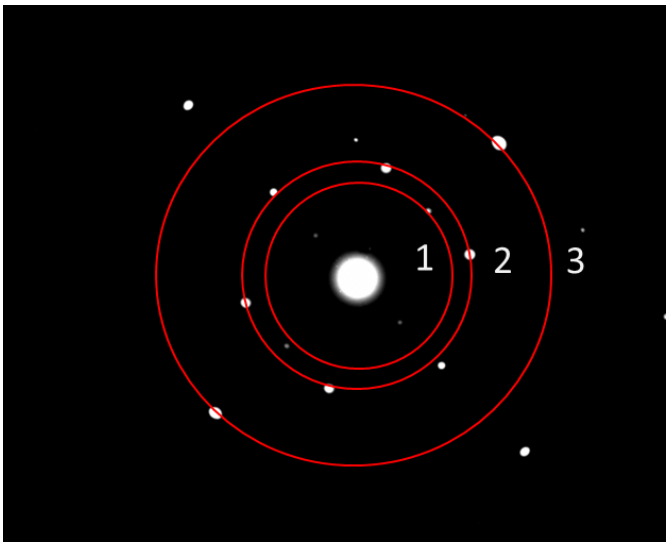

Ring number	Indexed hkl	Measured d-spacing	Calculated d-spacing
1	111	1.16	1.14
2	220	1.39	1.4
3	222	2.31	2.28

Figure 4.14: Selected area diffraction patterns of the alumina thin film (γ–Al_2O_3)

It has been demonstrated that thermal oxidation of aluminum substrate could achieve γ–Al_2O_3 thin film. This method is easy to apply and the synthesized Al_2O_3/Al is suitable for IR reflectance measurement. Some preliminary experiments will be performed on the model supported Ru/Al_2O_3 catalyst with this thin film support.

4.3.3 Colloidal synthesis of Ru nanoparticles

The synthesized Ru nanoparticles were characterized with TEM and the results are summarized in Table 4.1. As expected, higher $RuCl_3$ concentration leads to larger Ru particles and higher reduction temperature leads to smaller Ru particles [195]. The synthesized Ru particle size ranged from 1.5 nm to 5.4 nm. The addition of Ru seeds could significantly increase the particle size. Figure 4.15 and Figure 4.16 shows the TEM images of Ru nanoparticles as synthesized and it indicates that mono-dispersed Ru nanoparticles were successfully synthesized via colloid method.

Table 4.1 Summary of Ru nanoparticle size at different synthesis conditions

Catalyst #	Temperature (C)	Ru concentration (mM)	Ru nanoparticle size (nm)
a	180	1.28	1.5±0.7
b	180	7.7	2±0.7
c	180	1.28 (*with seeds)	2.5±1.5
d	180	7.7 (*with seeds)	4±2.5
e	150	1.28	3±1.3
f	150	7.7	3.6±1.4
g	150	1.28 (*with seeds)	4.5±1.5
h	150	7.7 (*with seeds)	5.4±1.6
*With 1.5 nm Ru nanoparticles as seeds			

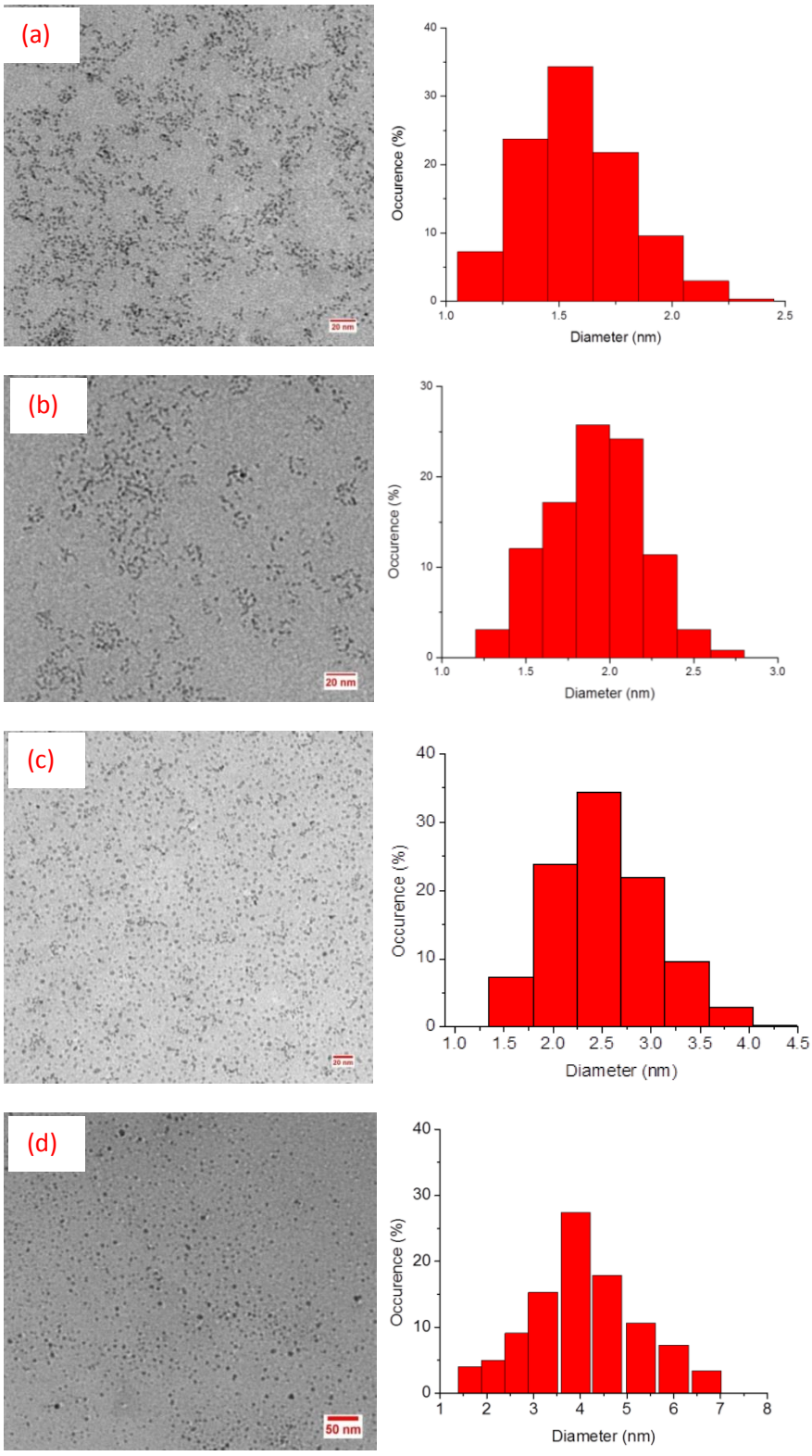

Figure 4.15: TEM images and size distribution of Ru nanoparticles as synthesized with reduction temperature of 180 °C

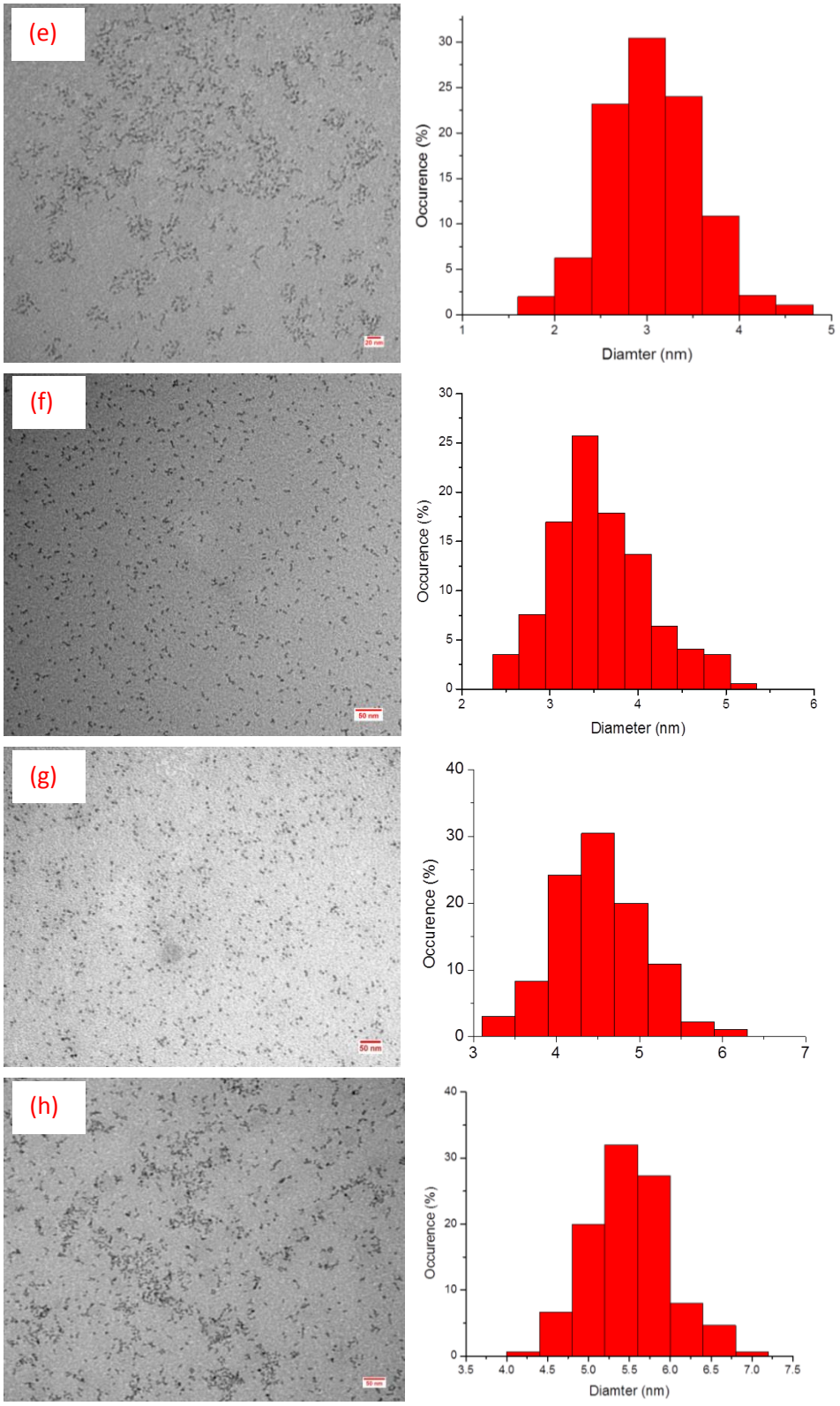

Figure 4.16: TEM images and size distribution of Ru nanoparticles as synthesized with reduction temperature of 150 °C

4.3.4 Model supported Ru/Al_2O_3 catalyst characterization

After the successful synthesis of Ru nanoparticle and aluminum oxide support, wet impregnation method was applied to make the model supported catalyst $Ru/Al_2O_3/Al$. The Ru nanoparticles as synthesized were dropped on Al_2O_3/Al support followed by the addition of acetone to remove the protective agent. After several times of drop and dry, the sample was treated in a UVO cleaner for 3 h to remove residual organics prior the adsorption test in the vacuum chamber. Figure 4.17 shows the IR spectra of the model catalyst $Ru/Al_2O_3/Al$ under vacuum condition. It is clear that the sample surface was covered with residual PVP [200, 210].

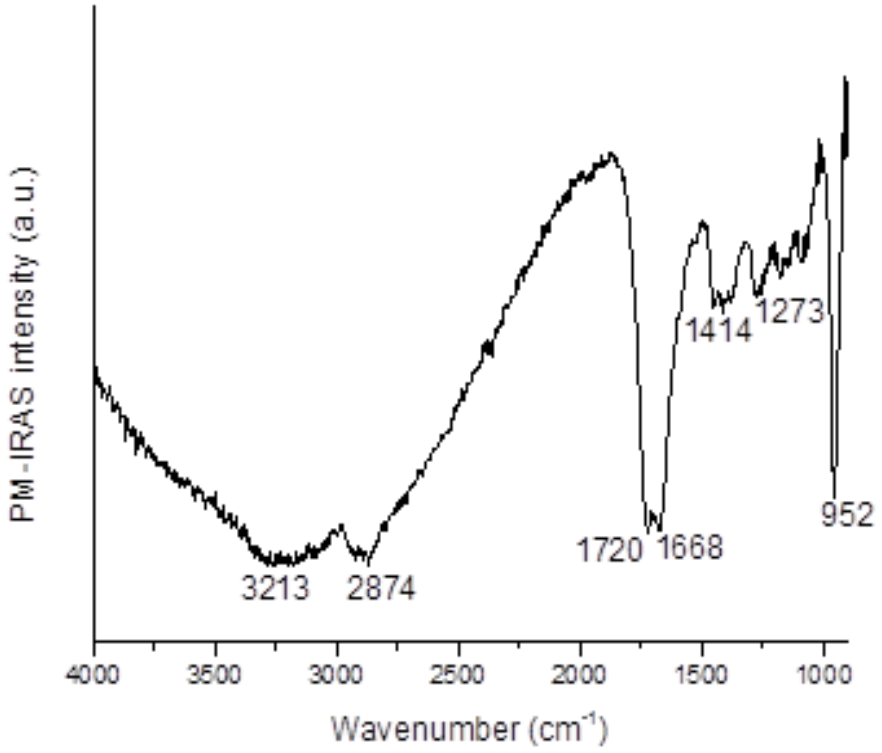

Figure 4.17: PM-IRA spectra of $Ru/Al_2O_3/Al$ under vacuum condition (10^{-9} Torr)

To remove the undesired organics, oxidation process was performed at 10^{-6} Torr O_2 partial pressure in the vacuum chamber. It turned out the oxidation at 500 K for 30 min did remove some of the organic on the surface, as seen in Figure 4.18. However, further oxidation at 500 K and 600 K did not make any improvement. Sputter cleaning with Ar^+ and oxidation at elevated temperatures were also attempted to remove the organic residuals, but the results were not satisfactory. The sample was taken out of the chamber and characterized with Raman spectroscopy. As shown in Figure 4.19, the sample surface was covered with significant carbon species [211]. It would be better to remove the organics completely before Ru nanoparticles were deposited onto the support.

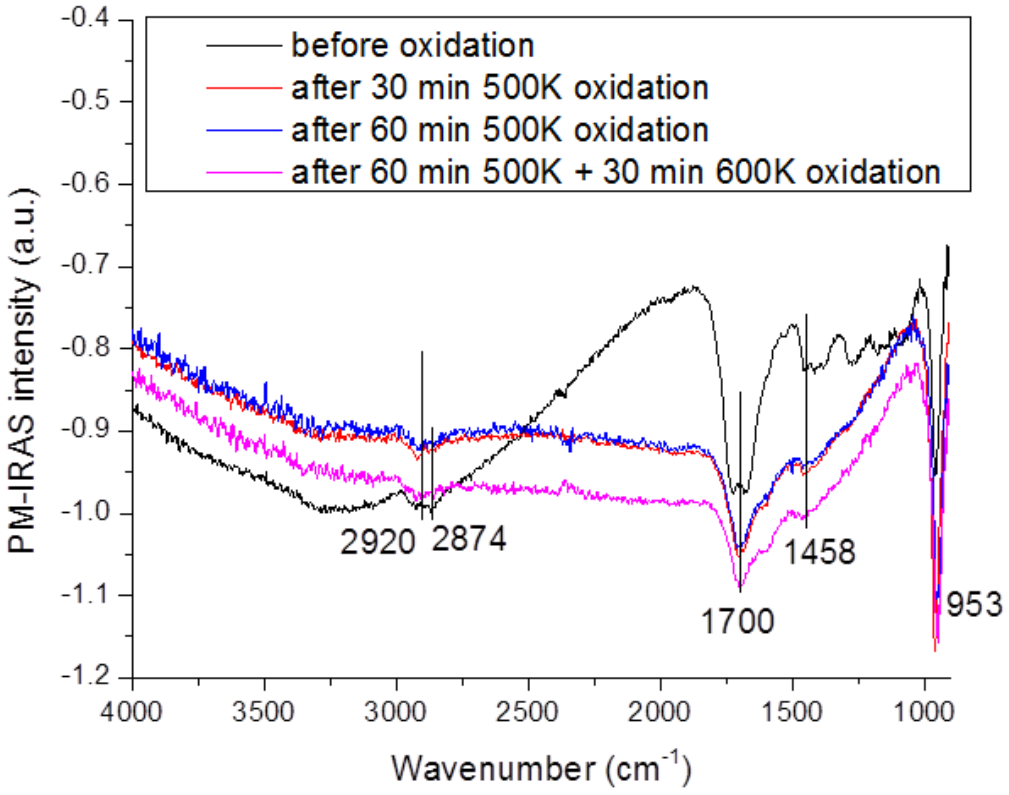

Figure 4.18: PM-IRA spectra of $Ru/Al_2O_3/Al$ sample after different treatment

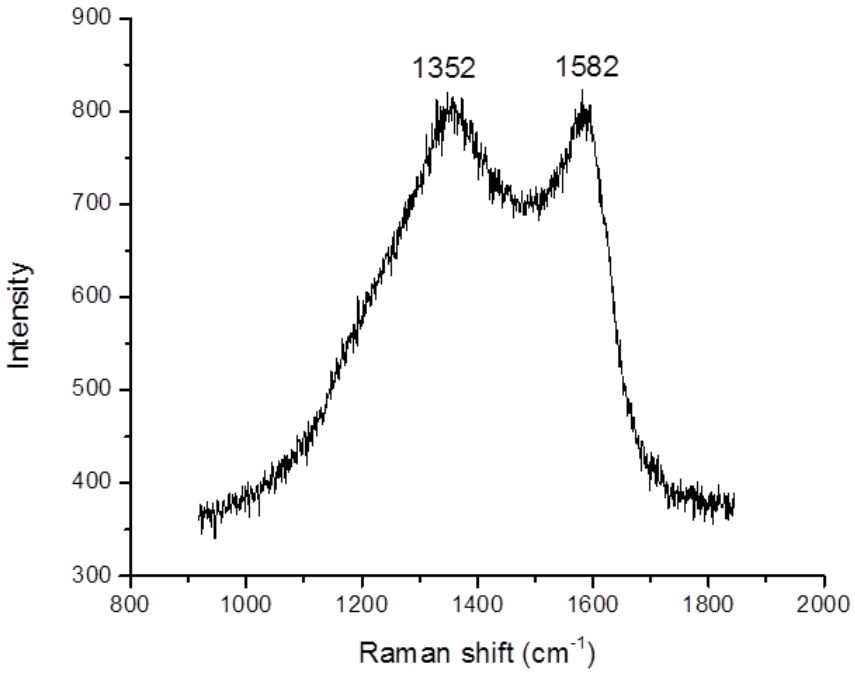

Figure 4.19 Raman spectra of $Ru/Al_2O_3/Al$ sample after different treatment

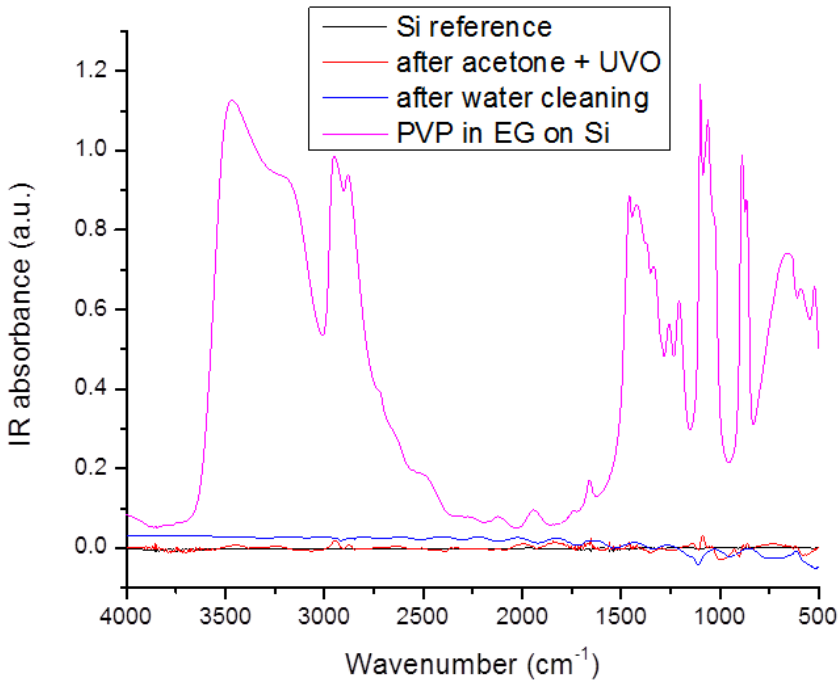

Figure 4.20: DRIFT spectra of Ru deposited on Si after different cleaning process

To avoid possible organic residuals on the model catalyst from the solvent, Ru nanoparticles were extracted from the solvent and cleaned before they were deposited on the support. Figure 4.20 presents the DRIFT spectra of Ru solution deposited on Si wafer after different cleaning processes. Comparing to the reference spectra of PVP/EG, both hydrothermal method and UVO cleaning method showed good performance in removing PVP form Ru nanoparticles while the latter one is relatively better. Thus acetone cleaning followed by UVO treatment was applied to clean Ru nanoparticles prior their deposition on the model support Al_2O_3/Al in this work.

Before the model catalyst of Ru/Al_2O_3 was loaded into the PM-IRAS chamber, the sample was characterized with XPS and tested with DRIFTS instrument. From the XPS spectra shown in Figure 4.21, it was noted that Ru atomic percent was about 0.67%, and there were some other elements on the sample surface including Ca, Si, and Na, etc. These trace elements were probably from the alumina support since the chemical used in Ru nanoparticles synthesis did not contain these elements. Further XPS analysis was performed on the Al_2O_3/Al sample right after the thermal oxidation of the aluminum substrate, and these elements were clearly observed in the spectra as shown in Figure 4.22. It need to be pointed out that, to eliminate the possible contamination in atmosphere, the Al_2O_3/Al sample was sputter cleaned with Ar in the XPS chamber for several hours and the signal of Ca, Si and C did not attenuate much (less than 10%). More detailed analysis would be required for surface characterization of the model catalysts before it is to be studied in the vacuum chamber in the future.

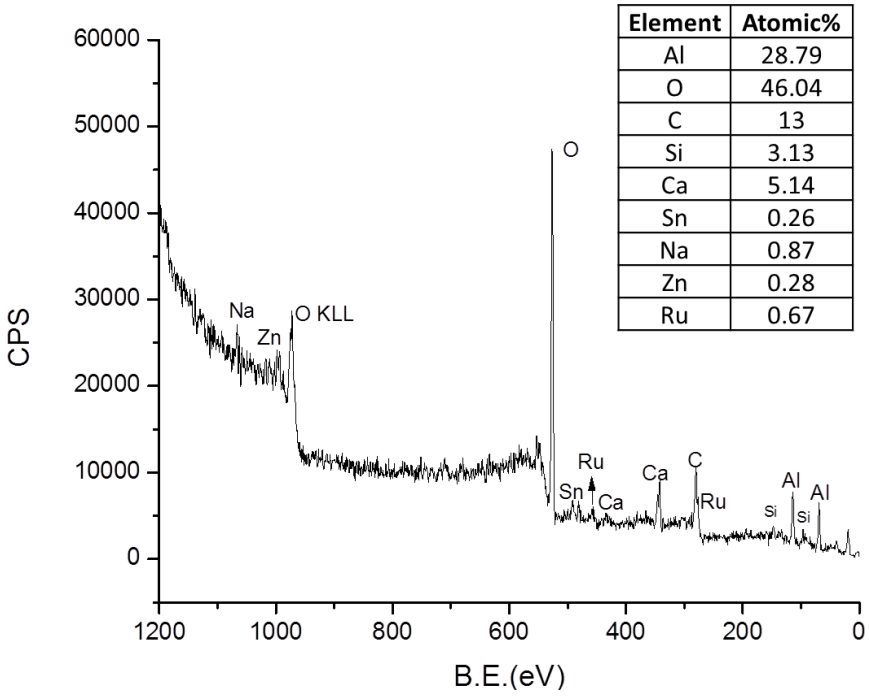

Figure 4.21: XPS spectra of model supported catalyst Ru/Al_2O_3

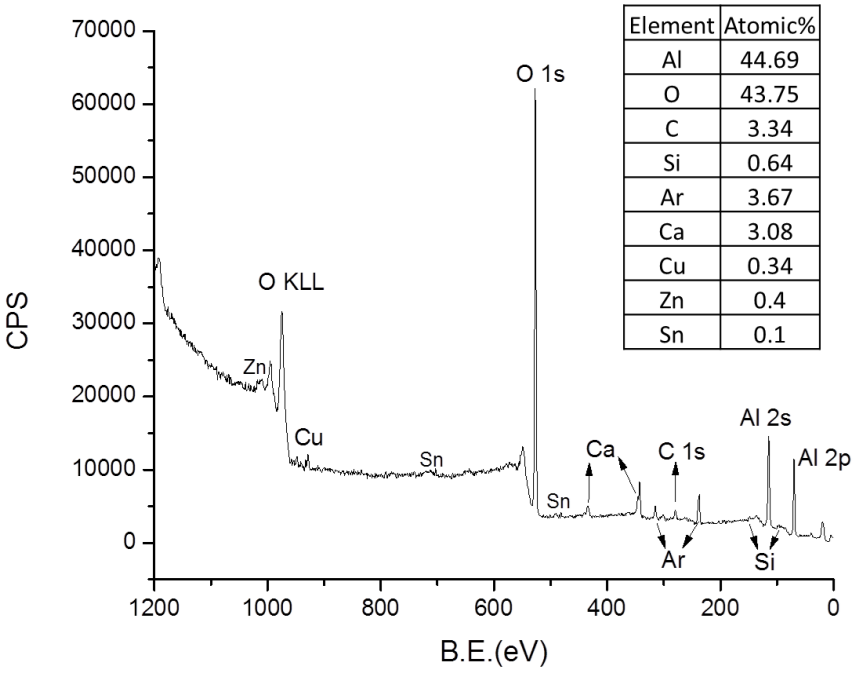

Figure 4.22: XPS spectra of Al_2O_3/Al after sputter cleaning in XPS chamber

4.3.5 Preliminary test on supported Ru/Al_2O_3 model catalyst

After deposition of Ru nanoparticles onto the alumina support, the Ru/Al_2O_3 model catalyst was tested with DRIFTS instrument for CO adsorption at room temperature. The sample was reduced with 5% H_2/He at 300 °C for 2 h and then purged with He at room temperature for 1 h before it was exposed to 5% CO/He for 1h. After CO exposure, the reaction cell was purged with He during which process the DRIFT spectra were acquired continuously.

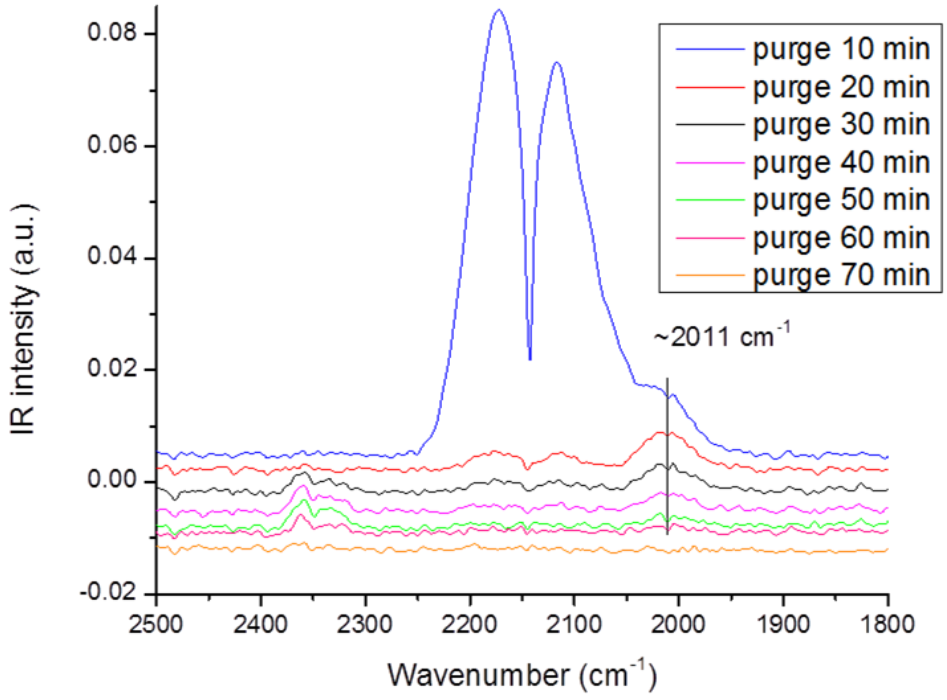

Figure 4.23: DRIFT spectra of CO adsorption on Ru/Al_2O_3 during He purging

As shown in Figure 4.23, both the gas phase signal (2143 cm^{-1}) and the signal of surface adsorbed CO molecules (2011 cm^{-1}) decreased significantly during the He

purging process. After 1 h purging, both the gas phase signal and the surface signal disappeared in the IR spectra. It is reasonable to observe the attenuation of gas phase signal, but the disappearance of surface adsorbed CO molecules is unexpected. It was suspected that residual oxygen from the He gas line was introduced to the reaction cell and reacted with surface adsorbed CO molecules. However, gas purity check with MS indicated undetectable oxygen in He gas, and repeated CO adsorption experiments showed the same results. The possible explanation is that after long time He purging, the remaining adsorbed CO molecules rearranged on the Ru nanoparticles and the concentration is below the detection limit of the DRIFTS instrument.

4.4 Conclusions and summary

It has been demonstrated that model supported catalyst Ru/Al_2O_3 can be made via wet deposition of mono-dispersed Ru nanoparticles on alumina thin film support. The γ-like alumina thin film can be made via thermal oxidation of aluminum substrate at 900 K for 12 h. Even though it is challenging to make crystalline alumina thin film via magnetron sputter deposition method, it would be beneficial to run more experiments to find the optimal deposition condition for the synthesis of γ-Al_2O_3 or to use a single crystal substrate that can stand high temperature annealing to make α-Al_2O_3. Mono-dispersed Ru nanoparticles of different size can be synthesized via colloid method using PVP as the protective agent, which can be removed from Ru nanoparticles with acetone/ethanol cleaning plus UVO treatment. The model supported Ru/Al_2O_3 catalyst was tested with CO adsorption in DRIFTS instrument and more studies are required

before the sample is to be tested in the PM-IRAS system. With the demonstrated model catalyst synthesis method, various desired model catalysts can be prepared and be investigated in the PM-IRAS system to bridge the “pressure gap” and “material gap” at the same time. Especially, mono-dispersed nanoparticles via colloidal method could be utilized to study the size effect of catalysts on different reactions.

CHAPTER 5

Particle Size Effect on Selective NO Reduction with Propene in Excess Oxygen over Pt/Al_2O_3 Catalysts

Catalytic reduction of NO has been a hot topic in catalysis community due to its importance in environmental- and industrial- related process. This chapter will cover the main findings of selective catalytic reduction of NO with propene in excess oxygen on Pt/Al_2O_3 catalysts with different particles sizes. It was found, on Pt catalysts with larger particle size, both higher NO conversions and isocyanate/cyanide surface species ratios were observed during the reaction. The isocyanate species are proposed to be important intermediate species for NO reduction, and the activation of propene by oxygen is a crucial step for the formation of isocyanate species. Larger Pt particles, which have more terrace sites other than corner or edge sites, can facilitate NO dissociation to provide oxygen for propene activation. A plausible mechanism was proposed for the reaction of NO with propene on Pt/Al_2O_3 catalyst.

5.1 Introduction

Nitrogen oxides (NO_x) emitted from stationary and mobile sources can lead to various environmental and human health problems: the formation of acid rain,

photochemical smog and respiratory diseases [2, 5]. Traditional three-way catalytic convertors (TWC) have been employed to control the automobile exhaust emissions (NO_x, CO and hydrocarbons) since 1970s. However, the TWC technology is not effective at removing NO_x from the oxygen-rich exhausts from lean-burn engines and diesel vehicles. Right now, Environmental Protection Agency (EPA) is putting more stringent regulations on the NO_x emissions from transportation vehicle due to their significant contributions to the total NO_x emissions comparing to other sources, as shown in Figure 5.1. The U.S. EPA is finalizing an important rule designed to reduce air pollution from passenger cars and trucks. The estimated emission reduction of NO_x from the Final Tier 3 Standards is 10% (264,369 tons) by 2018, and 25% (328,509 tons) by 2030. The need to meet the stringent regulations has sparked investigations of several technologies for NO_x reduction, including NO_x decomposition, NO_x storage-reduction (NSR), and selective catalytic reduction of NO_x with hydrocarbons.

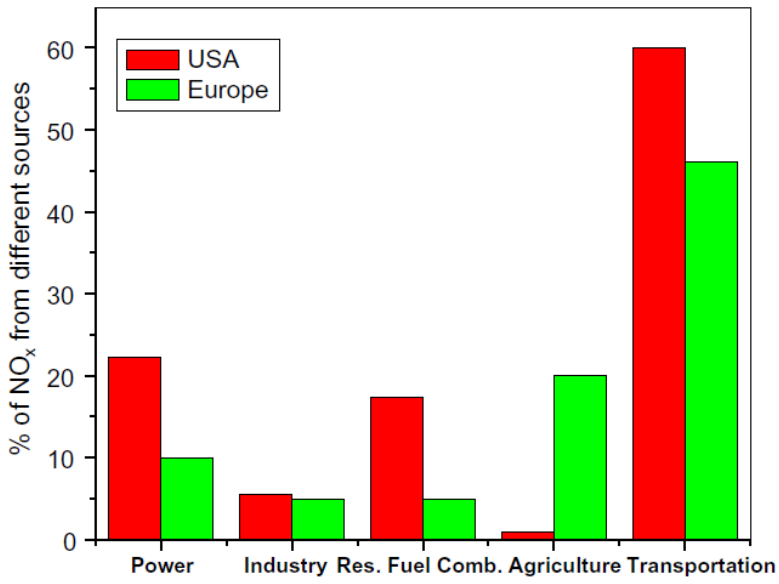

Figure 5.1: Comparison of different sources contributing to the NOx emissions in US and Europe, figure adapted from Ref [4]

The direct decomposition of nitric oxide to nitrogen and oxygen is one of the most attractive methods because this reaction is thermodynamically favorable and does not need any reductants. However, different problems are preventing the practical applications of various materials. Briefly, single crystal metals are not suitable for direct NO dissociation because the dissociated oxygen can either oxidize the metal surface to metal oxides or form an oxygen adlayer on the surface that hinders the dissociation process. The problem in using metal oxides to dissociate NO is that it requires high temperature (500-800 °C) and the excess oxygen in the exhaust will compete for the surface sites with NO, causing "self-poisoning" effect. The decomposition of NO over Cu-exchanged zeolites has been studied extensively since the pioneering work of Iwamoto et al [212]. Even though Cu-ZSM 5 catalyst showed good activity for NO dissociation, this type of material has very low hydrothermal stability which makes their practical application difficult [2, 4, 5].

NO_x storage-reduction catalysis, or lean-NO_x trap, is another possible method for NO reduction. The most accepted reaction pathway is consisted of two steps: NO_x storage at lean-burn conditions (air rich), and NO_x reduction at normal condition with stoichiometric air to fuel ratio (14.5:1). As shown in Figure 5.2, during the lean-burn stage, NO is oxidized to NO_2 and stored in a barium-based material in the form of nitrate (NO^{3-}). With plenty of oxygen present, the unburned HC, CO and hydrogen are readily oxidized to water and carbon dioxide. When the engine is switched to normal operation mode, the exhaust becomes comparatively oxygen-deficient, in which HC, CO and H_2 remain unoxidized. So the nitrate will react with these reducing agents and form harmless nitrogen, water, and carbon dioxide [213]. The major problem with NSR technology is

that the catalyst gets deactivated by the sulfur oxides in the exhaust. Two possible mechanisms are responsible for the deactivation: aluminum sulfate formation which covers the surface of alumina support or plug the pore of alumina support, and barium sulfate formation which is more stable than barium nitrate thus reduce the storage capacity of the catalysts.

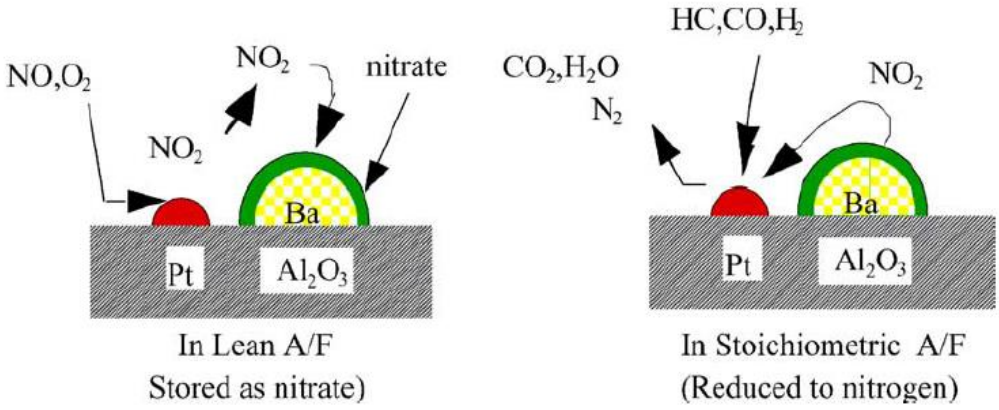

Figure 5.2: Representative schematic of NO_x storage-reduction on NSR catalyst [213]

In comparison, Selective catalytic reduction (SCR) of NO by hydrocarbons (HC) has shown good activity at low temperature region (200-350 °C) with superior resistance to water and sulfur components in the exhaust [2]. Extensive investigation on HC-SCR for NO reduction has been performed on different types of catalysts, including metal oxides, zeolites and supported metal nanoparticles (mainly platinum group metals). It was found that base oxides (e.g. Al_2O_3, MgO, TiO_2, ZrO_2) and these oxides promoted by different elements (e.g. Co, Ni, Cu, Fe, Sn, Ga, In) are active for HC-SCR reaction [2, 5]. However, the operational temperature on these oxide catalysts is typically high above 673 K, and the activity is low at high space velocity [2, 5]. In addition, these metal oxides get

deactivated fast with sulfur dioxide and/or water present. Hydrothermal deactivation due to loss of specific surface area is another issue for this type of catalysts. Zeolites catalysts showed very high performance on HC-SCR, but the low hydrothermal stability is a major obstacle for its application. Supported precious metal catalysts, especially supported Pt catalysts, show high stability and high tolerance to sulfur oxides and water vapor. They showed very high activity (60-80 % NO conversion) at low temperature (200-250 °C), but the non-selective nitrous oxide production is a drawback. Alkali promoters are found to increase both the NO conversion and N_2 selectivity during the reaction on supported Pt catalysts, probably due to the modification of the bond strength for different reactants adsorbed on the surface [15, 18, 214, 215].

Due to its great performance for NO_x abatement in excess oxygen, supported Pt catalyst has received considerable attention in the catalysis community [2, 5, 7-11]. Significant efforts have been put into the investigation of HC-SCR reaction on Pt catalysts with various oxide supports, different Pt loading and dispersion, and different promoters [7-21]. As a result of these efforts, two distinct reaction mechanisms have been proposed for NO reduction by propene in excess oxygen on alumina-supported Pt catalysts: (1) NO decomposition and subsequent oxygen removal by the hydrocarbon reductant [7-11]; (2) formation of an intermediate isocyanate surface species [18-21].

The first mechanism was proposed by Burch and coworkers based on their detailed studies with temporary analysis of product (TAP) technique [7]. In their work, TAP data indicated the crucial role of reduction of the platinum surface. Over a completely reduced Pt/Al_2O_3 surface, very little nitrious oxide (N_2O) is produced, because NO dissociation leading to nitrogen as the main product takes place

preferentially on these platinum sites. On oxidized surfaces, most NO molecules adsorb and desorb without dissociation. When the temperature is increased, both adsorption and dissociation of NO are easier and adsorbed nitrogen atoms become more mobile and recombine to form N_2. The mechanism proposed also explains why propene shows the best activity for HC-SCR comparing to other reducing agents such as carbon monoxide and hydrogen.

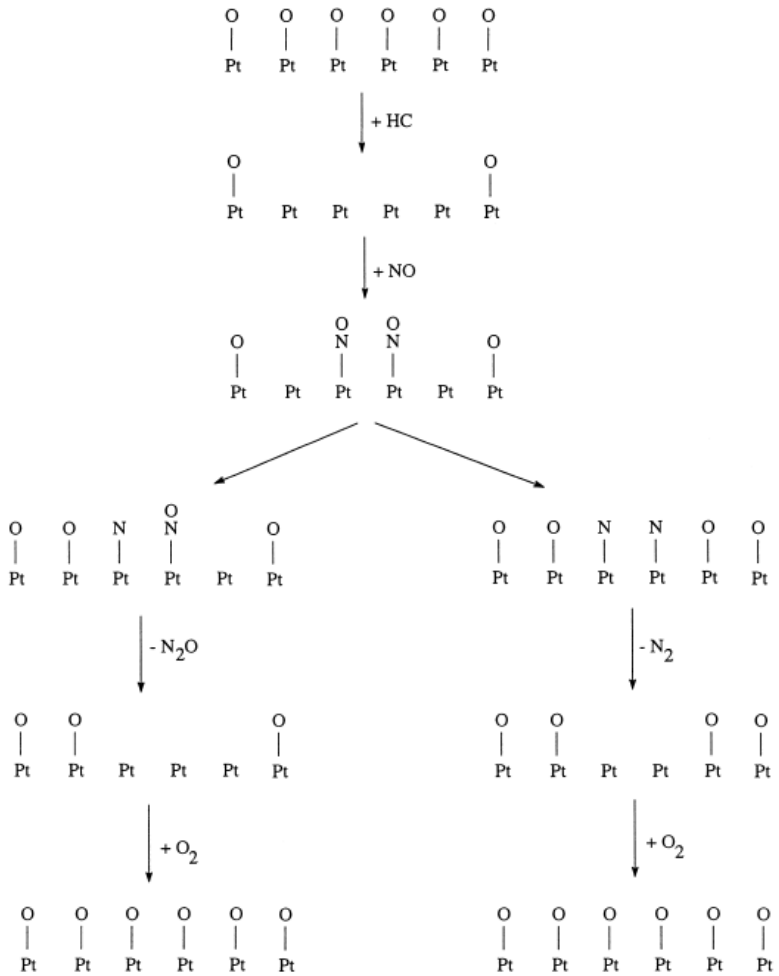

Figure 5.3: Schematic of direct decomposition-reduction mechanism, from Ref [7]

It is believed that oxygen can compete for the reduced platinum sites with NO and the reductant is in charge of cleaning off the oxygen atoms on platinum surface. One propene molecule can remove nine oxygen atoms while hydrogen and CO can only remove one oxygen atom, making propene a better reducing agent. As shown in Figure 5.3, the predominant mechanism is proposed as two steps: reduction of platinum sites by the hydrocarbon, followed by the decomposition of NO (to generate nitrogen and adsorbed oxygen) over the reduced platinum sites. However, there was another argument that the platinum remained fully oxidized during the reaction and the hydrocarbon is unable to reduce it [7, 216].

The second mechanism involved the isocyanate intermediates was mainly supported by Bamwenda et al [19] and Captain et al [20, 21] based on their FTIR measurements and kinetic studies. In these studies, abundant isocyanate species were observed under reaction conditions. These species were weakly adsorbed on the catalyst surface, and could easily react with oxygen or nitrogen oxides. It was suggested that iscoyanate species formed after the reaction between NO and adsorbed organic species, and the activation of propene by oxygen was really important based on their kinetic studies with different oxygen concentration [20].

According to the first mechanism, the metal particle size would play a significant role during NO reduction with propene, since NO decomposition was reported to take place more easily on Pt catalyst with larger particles [217]. However, the particle size effect is uncertain for the second mechanism, where the activation of propene with oxygen is proposed an important step for the formation of intermediate isocyanate species. Several studies have been performed to understand the effect of metal dispersion and

particle size for NO reduction on Pt catalysts. For example, Burch et al [9] reported that there was a significant effect of metal dispersion for silica-supported catalysts but little effect for alumina-supported catalysts. On Pt/SiO_2 catalysts, the maximum NO conversion fell from about 80% to 50% and the temperature for optimum activity shifted from 210 °C to 250 °C as the dispersion decreased from 39% to 1.8%. On the other hand, there was no obvious change in NO conversion on Pt/Al_2O_3 catalysts. However, the turnover frequencies (TOFs) for NO reduction on Pt/Al_2O_3 catalysts with 10% metal dispersion (11 nm) are almost twice those with 40% dispersion (3 nm). Similarly, Xue et al [218] investigated the oxidation of NO on Pt catalysts with different supports and claimed that the particle size effect was significant over silica-supported Pt catalysts but less significant on alumina-supported catalyst. Lee et al [12] also revealed that the total conversion of NO on Pt/Al_2O_3 catalyst was almost not affected by metal dispersion while the oxidation of NO was over 100 times higher on the catalyst with low dispersion (4.4%) than high dispersion (82%). Based on their results, the TOFs for NO reduction on Pt/Al_2O_3 catalyst with low dispersion was about 12 times of that with high dispersion at 245 °C. Contrarily, Denton et al [219] showed that the intrinsic activity of different supported Pt catalysts increased with decreasing dispersion, and this effect becomes stronger as the dispersion decreased below 18%. Furthermore, García-Cortés et al [220] investigated NO reduction on Pt-beta catalysts with different metal dispersion and concluded that the catalysts with larger particles obtained higher NO conversion with lower optimum temperature, and there was a linear correlation between the particle size and the TOFs for NO reduction. Unfortunately, among the studies presented, there was no *in situ* spectroscopic characterization of the surface species during the reaction. The

surface chemistry remains to be revealed on catalysts with different particle sizes. Most importantly, how does the particle size influence the reactive intermediates under reaction conditions as well as the overall catalyst activity?

To answer this question, *in situ* DRIFTS and mass spectrometry were applied to investigate the HC-SCR reaction on Pt/Al_2O_3 catalysts with different particle sizes. By changing the heating rate, calcination temperature and time, Pt catalysts with a wide range of particle sizes, from 2 nm to 27.5 nm were prepared. The catalyst activity was tested in a DRIFTS cell and the NO conversion was analyzed using a mass spectrometer. The surface species under different reaction conditions were monitored with a DTGS detector in the DRIFTS instrument. The effect of particle size on the active surface species, as well as NO reduction efficiency, will be discussed.

5.2 Experimental methods

5.2.1 Pt/Al_2O_3 catalyst preparation and characterization

The Pt/Al_2O_3 catalysts were prepared by wetness impregnation of the γ-Al_2O_3 support (Alfa Aesar) with an aqueous solution of tetraammineplatinum (II) chloride monohydrate $Pt(NH_3)_4Cl_2 \bullet H_2O$ (Alfa Aesar). The support was dried overnight at 120 °C prior the impregnation. Following wet impregnation, the sample was dried at 120 °C for 12 h and then calcined at different conditions. The average Pt particle size was adjusted by varying the heating rate (2 °C/min vs. 10 °C/min), calcination temperature (500-700 °C) and calcination time (3-48 h). The nominal Pt loading was determined as 1 wt%

by inductive coupled plasma-optical emission spectroscopy (ICP-OES) (PerkinElmer Optima 2000 DV), and the particle size and dispersion of Pt was determined by H_2 chemisorption using a Chemisorption Analyzer (Micromeritics AutoChem II). The particle size was further characterized by scanning transmission electron microscopy (STEM) (JEOL 2100 F).

5.2.2 Catalyst performance studies

The SCR reactivity of Pt catalysts with different sizes was tested in a DRIFTS cell capable of heating and cooling samples to the desired temperature. Prior to each experiment, the catalysts were pretreated at 250 °C for two hours in a continuous flow of 3.3% O_2 in He and then purged with He flow at 250 °C for 30 min. After pretreatment, the sample was cooled to the reaction temperature of interest, and a gas mixture of 2000 ppm NO, 2000 ppm C_3H_6, and 2% O_2 in He was introduced to the reaction cell at a flow rate of 50 cm^3/min. Certified analyzed gas mixtures of 1% NO/He (Praxair), 1% C_3H_6/He (Praxair), 99.999% O_2 (Airgas) and 99.999% He (Airgas) as a carrier gas were used to make desired mixtures. Catalyst activities were investigated at 200-450 °C on Pt/Al_2O_3 with different sizes, and the gas products were analyzed by a mass spectrometer (Hiden HAL IV RC). The TOFs (molecules/active site/second) on various Pt catalysts were calculated using the following equation:

$$TOF\ (s^{-1}) = (Q/60*0.2\%*V_A*N_A*C_{NO}/100) / (SA*m/\theta*10^{20})$$

Where Q is the flow rate of the gas mixture (50 cm^3/min), V_A is the ideal gas molar volume (22465 cm^3/mole), N_A is the Avogadro constant $6.022*10^{23}$, C_{NO} is the NO

conversion (%) based on the concentration change of NO in the inlet and outlet gas mixture, SA (m^2/g) is the total surface area of Pt metals per gram catalyst measured from the chemisorption experiments, θ is the cross-sectional area of Pt atom (8.0 $Å^2$ per atom), and m is the weight of loaded catalysts for experiments (0.03 g).

5.2.3 Surface species investigation with *in situ* DRIFTS measurement

Diffuse reflectance IR spectra were collected on a Bruker FTIR instrument (EQUINOX 55) equipped with a DTGS detector. During spectra acquisition the external optics were purged with CO_2-free dry air generated from a purge gas generator (Parker 75-62 FTIR purge gas generator). IR spectra were acquired in the range of 400-4000 cm^{-1} by averaging 300 scans with a nominal resolution of 4 cm^{-1}. Surface species information were obtained with DRFITS measurements at steady state reaction conditions over the temperature range of 200-450 °C, and the spectra taken at 250 °C were shown for comparison since the IR bands for isocyanate and cyanide species were well resolved at this temperature. Three different types of DRIFTS experiments were performed: (1) reaction with excess oxygen (2000 ppm NO + 2000 ppm C_3H_6 + 2% O_2) on oxygen-pretreated Pt catalysts (3.3% O_2/He at 250 °C for 1h followed by He purge for 30 min at 250 °C); (2) reaction without oxygen (2000 ppm NO + 2000 ppm C_3H_6) on oxygen-pretreated Pt catalysts(3.3% O_2/He at 250 °C for 1h followed by He purge for 30 min at 250 °C); (3) reaction without oxygen (2000 ppm NO + 2000 ppm C_3H_6) on hydrogen-pretreated Pt catalysts (10% H_2/He at 400 °C for 2h followed by He purge for 1h at

400 °C). All spectra were acquired after the band intensities reached the steady-state at the desired temperature.

5.3 Results and discussion

5.3.1 Pt catalysts with various dispersion and particle size

As shown in Table 5.1, the Pt dispersion and particle size changed significantly with calcination conditions. The dispersion of Pt varied from 55% to 4% after the calcination temperature and time increased. In the meantime, the average size of Pt particles increases from 2(±0.3) nm to 27.5(±5.5) nm, which was close to the average particle size characterized with STEM from 2.5(±1.8) nm to 20.2(±5.9) nm. More than 20 STEM images were taken for each sample and the size distribution of Pt particles were counted with more than 100 particles from the STEM images. The representative STEM images and particle size distribution of fresh Pt catalysts are shown Figure 5.4. It is clear that the particles grow bigger with longer calcination time or at higher calcination temperature. After the reaction at 200-450 °C, the catalysts were characterized again with chemisorption and STEM and the results were summarized in Table 5.2. In comparison to the fresh catalysts, the particle size of all five Pt catalysts after reaction increased due to the possible sintering during the reaction, and the size increase is more obvious for the catalysts with small particles. The representative images of each catalyst after reaction were shown in Figure 5.5. The catalytic activities of Pt catalysts with different sizes were evaluated in DRIFTS instrument and the results are discussed below.

Table 5.1 Dispersion and particle size of Pt catalysts after different calcination process

Fresh catalyst	Heating rate (C/min)	Calcination temperature (C)	Calcination time (h)	Pt dispersion (%)	Pt size (nm)	Pt surface area (m2/g)	STEM (nm)
Pt-1	2	500	3	55±8	2±0.3	1.35	2.5±1.8
Pt-2	2	500	10	34±6.5	3.2±0.6	0.83	4.6±3.3
Pt-3	10	500	10	25±5	4.4±0.9	0.61	5.8±3.3
Pt-4	10	600	10	9.4±2	12±2.6	0.23	12.6±5.8
Pt-5	10	700	48	4±0.8	27.5±5.5	0.10	20.2±5.9

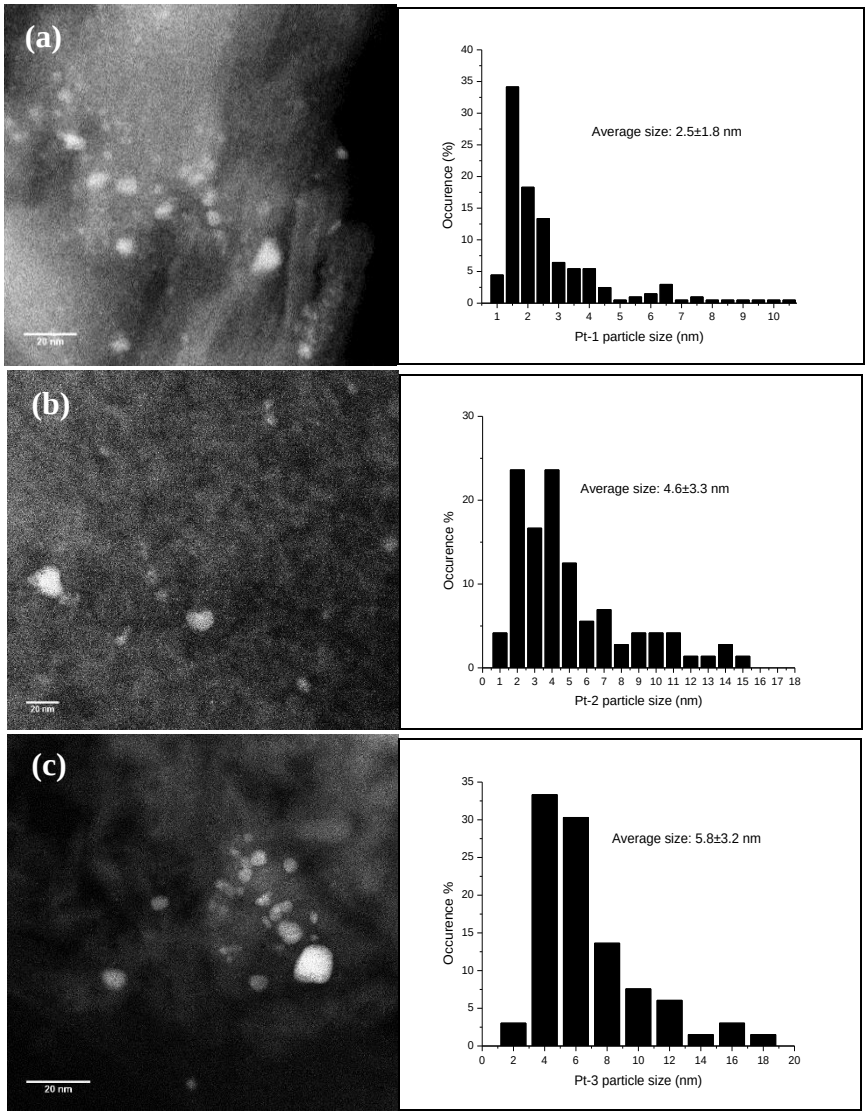

Figure 5.4: Representative STEM images of Pt/Al_2O_3 catalysts with different particle sizes: (a) Pt-1, (b) Pt-2, (c) Pt-3, (d) Pt-4, and (e) Pt-5.

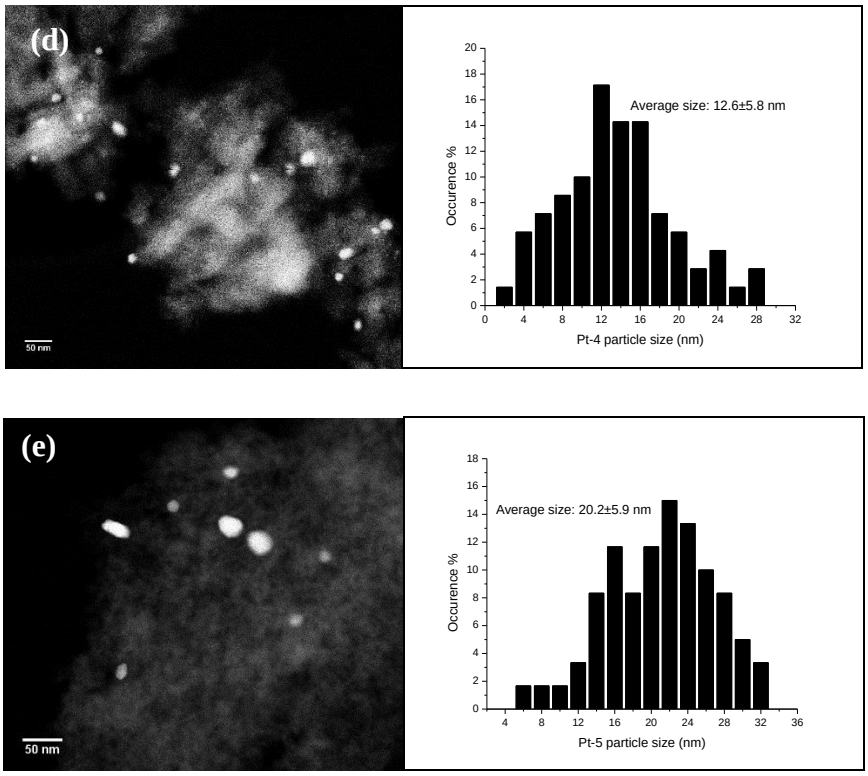

Figure 5.4: Representative STEM images of Pt/Al_2O_3 catalysts with different particle sizes: (a) Pt-1, (b) Pt-2, (c) Pt-3, (d) Pt-4, and (e) Pt-5.

Table 5.2 Dispersion and particle size of Pt catalysts after reaction

Catalyst after reaction	Pt dispersion (%)	Pt size (nm)	Pt surface area (m2/g)	STEM (nm)
Pt-1	31.5±5	3.6±0.6	0.78	4±1.9
Pt-2	18±4	6.3±1.4	0.44	6.3±2.1
Pt-3	16±3	7.1±1.3	0.39	7.9±2.5
Pt-4	6.8±2	16.7±4.9	0.17	15.4±4.7
Pt-5	3.8±1	28.8±7.6	0.09	21.6±5.7

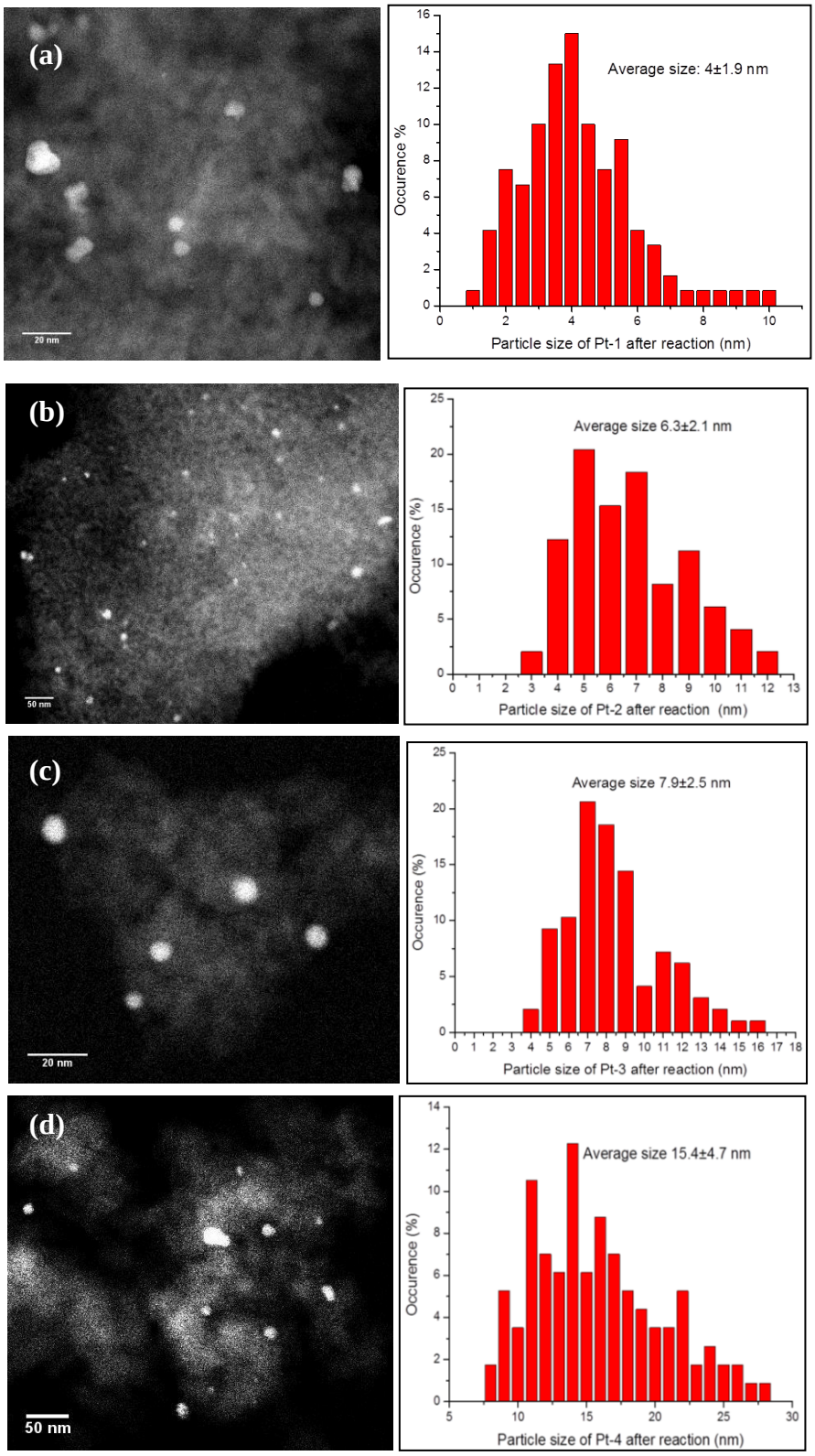

Figure 5.5: Representative STEM images of Pt/Al_2O_3 catalysts after reaction: (a) Pt-1, (b) Pt-2, (c) Pt-3, (d) Pt-4, and (e) Pt-5.

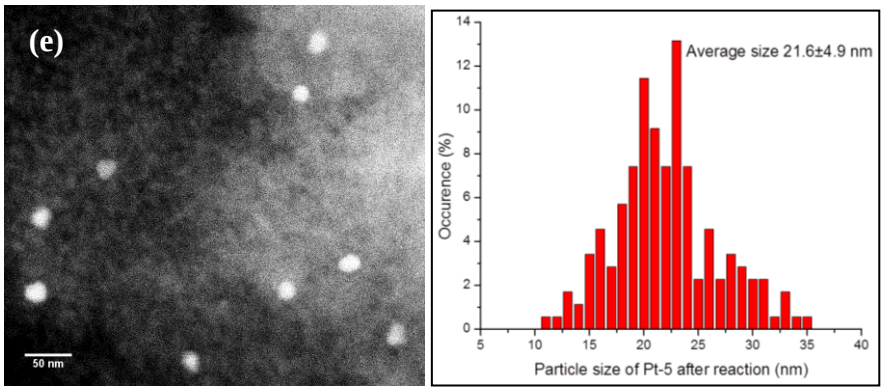

Figure 5.5: Representative STEM images of Pt/Al_2O_3 catalysts after reaction: (a) Pt-1, (b) Pt-2, (c) Pt-3, (d) Pt-4, and (e) Pt-5.

5.3.2 Pt particle size effect on the catalyst activity

The activity of Pt catalysts was investigated at the temperature range of 200-450 °C, and it was noted that NO conversion reached a maximum at around 300 °C and decreased at higher temperature for all catalysts. As shown in Figure 5.6, the catalysts had low activity at 200 °C with NO conversion around 8%. The NO conversion increased to 10-20% at 250 °C and reached maximum around 45-55% at 300 °C. Further temperature increase lead to a decrease in the catalyst activity and NO conversion was below 10% at 450 °C. These results agreed with the temperature effect reported in previous studies on this reaction: NO reduction decreases above the temperature at which complete oxidation of propene occurs, due to the preferential reaction of C_3H_6 with O_2 rather than NO [9, 20, 21]. The TOFs were compared at low NO conversion conditions for Pt catalysts with different average particle sizes. As shown in Figure 5.7, there was a linear correlation between the TOF and Pt particle size, and the TOFs for catalyst Pt-5

(0.24 s^{-1}) was about 24 times of that for catalyst Pt-1 (0.01 s^{-1}). Similar observation was reported for NO reduction with propene over Pt-beta zeolite catalysts [220]. The TOFs on Pt-beta catalyst with large particles (~27 nm) was almost 10 times of that measured for catalysts with small particles (~2.5 nm). It was proposed that the corner and edge sites could bind oxygen atoms more strongly than terrace sites, which may decrease the reactivity of oxygen on the surface. In addition, the authors proposed that the phase transition from Pt-(hex) to Pt-(1x1) might occur on (100) facets, which could lead to high TOF on the catalyst with large particles, because the Pt-(1x1) surface phase is more active for NO dissociation. [220]. The higher activity on larger Pt particles could also be attributed to its better NO dissociation ability on terrace sites rather than corner or edge sites [217, 221-223]. It has been reported that NO dissociation occurs more easily on Pt(211) and Pt(100) than on Pt(111) and Pt(110) with the latter orientations almost inactive, due to the change in the availability of four-fold hollow sites with no metal atom sharing between N and O adatoms suitable for catalyzing NO dissociation [221-223]. The importance of NO dissociation for the formation of active intermediates, such as isocyanate species, was also supported by the DRIFTS studies at different reaction conditions, which will be discussed below.

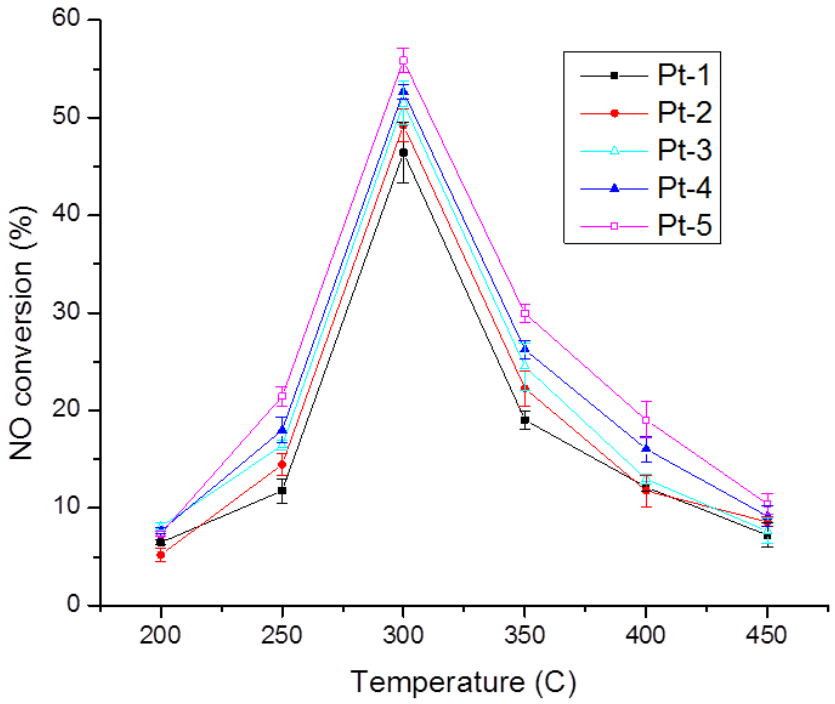

Figure 5.6 NO conversion on Pt catalysts with different sizes

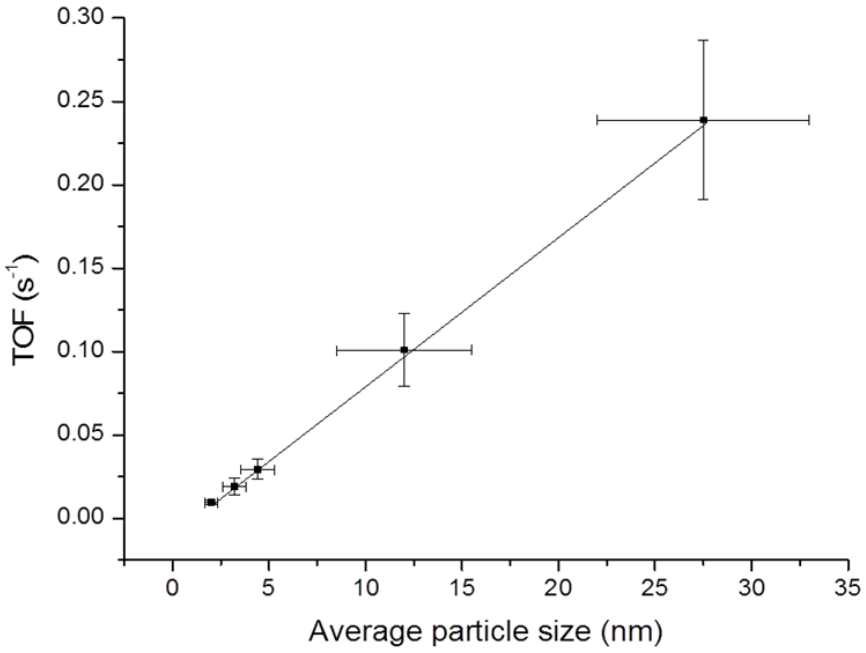

Figure 5.7: TOFs on Pt/Al_2O_3 catalysts with different particle sizes at 250 °C

5.3.3 Pt particle size effect on the formation of surface species at different reaction conditions

The influence of Pt particle size on the surface species was first investigated with *in situ* IR on oxygen-pretreated Pt catalysts at steady state reaction conditions with excess oxygen (2000 ppm NO, 2000 ppm C_3H_6 and 2% O_2). Similar surface species such as adsorbed hydrocarbon fragments (2904 cm^{-1}, 2998 cm^{-1}), isocyanate (2240 cm^{-1}), cyanide (2140 cm^{-1}), nitrates (1225-1305 cm^{-1}), nitrites (1225-1305 cm^{-1}) and carbonates species (1370-1600 cm^{-1}) were observed on all catalysts [18, 19, 21, 224, 225]. The IR bands observed in this work and the corresponding assignments were summarized in Table 5.3.

Table 5.3 IR bands position and corresponding assignment of surface species

IR band position (cm^{-1})	**Assignment**	**Reference**
1225-1305	Nitrite ($-NO_2^-$)	[19, 21, 224, 225]
~1588, ~1394, ~1376	Formate ($-COO^-$, -CH)	[19, 21, 224, 225]
~1570, ~1450	Acetate ($-COO^-$)	[18, 21, 224, 225]
~1672, ~1490	Nitrate ($-NO_3^-$)	[18, 21]
~1736	Nitrosium (-NO)	[18, 21]
2110-2180	Cyanide (-CN)	[18, 19, 21, 225]
~2180, 2232-2254	Isocyanate (-NCO)	[18, 19, 21, 225]

In several previous studies on NO reduction with propene in excess oxygen, both isocyanate and cyanide species were observed during the reaction on Pt/Al_2O_3 catalysts. Isocyanate species has been proposed as the reactive intermediates, while cyanide species was considered a spectator during the reaction [19-21]. It was confirmed based on observations during different gas (e.g. O_2/He, NO_2/He) flushing experiments over catalysts with pre-adsorbed isocyanate and cyanide species: with gas flowing, the cyanide species was stable (inactive) while iscoyanate species reacted with O_2 or NO_2 and disappeared eventually [21]. Similar flushing experiments were performed in this work and the same phenomenon was observed. After isocyanate species reached its maximum intensity during the reaction on Pt-2 at 250 °C, the sample was exposed to 3% O_2/He gas and the isocyanate species were observed decreased sharply during the purge while cyanide species hardly decreased, as shown in Figure 5.8. Meanwhile, at reaction conditions, the IR band intensity of the isocyanate species was almost constant after the reaction started (<5 min) while the band intensity of cyanide species continued to increase until the reaction reached steady state (>30 min), as shown in Figure 5.9, which also indicates that isocyanate species is an active intermediates and cyanide species is a spectator. It is well known that reaction intermediates species stays constant due to its continuous consumption and generation, while spectators accumulate as reaction goes. Thus, the ratio of isocyanate to cyanide species (NCO/CN) was calculated based on the integral area of each species and used as an indicator of the catalyst activity for comparison purposes in this work.

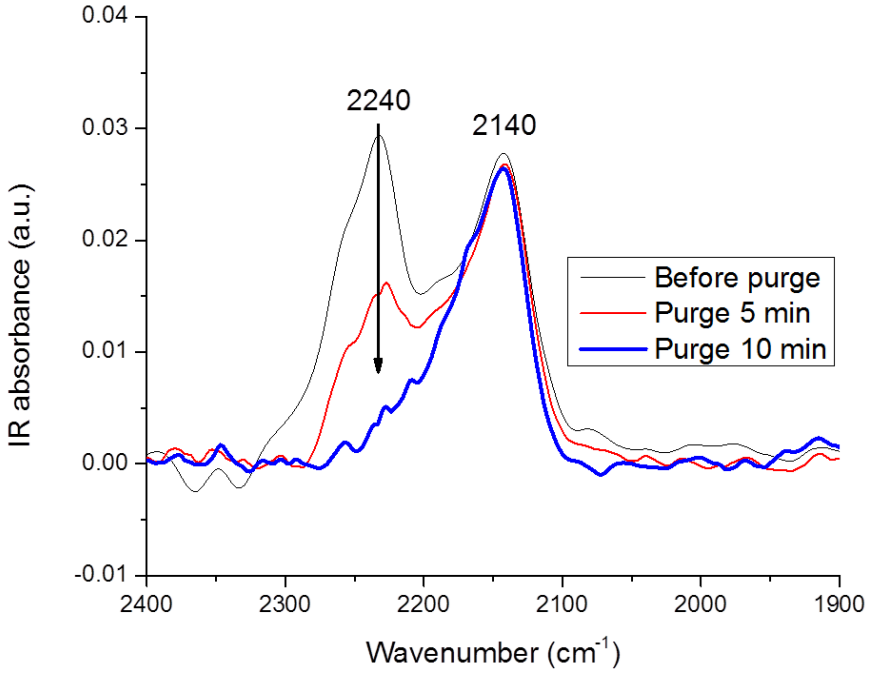

Figure 5.8: The IR spectra of isocyanate (2240 cm^{-1}) and cyanide (2140 cm^{-1}) species during the purge of 3% O_2/He after steady state reaction on Pt-2 at 250 °C

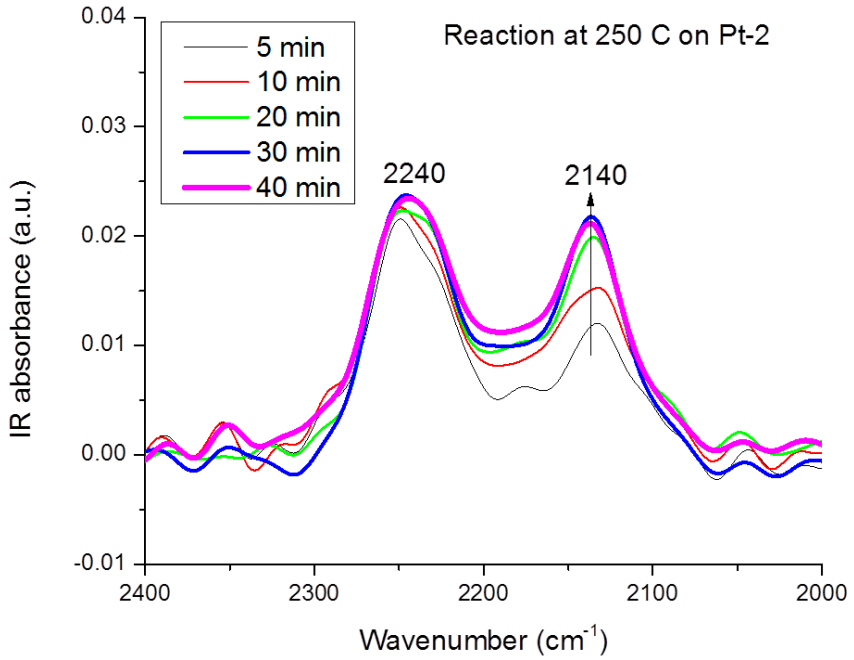

Figure 5.9: The IR spectra of isocyanate and cyanide species during the reaction on Pt-2 at 250 °C until steady state

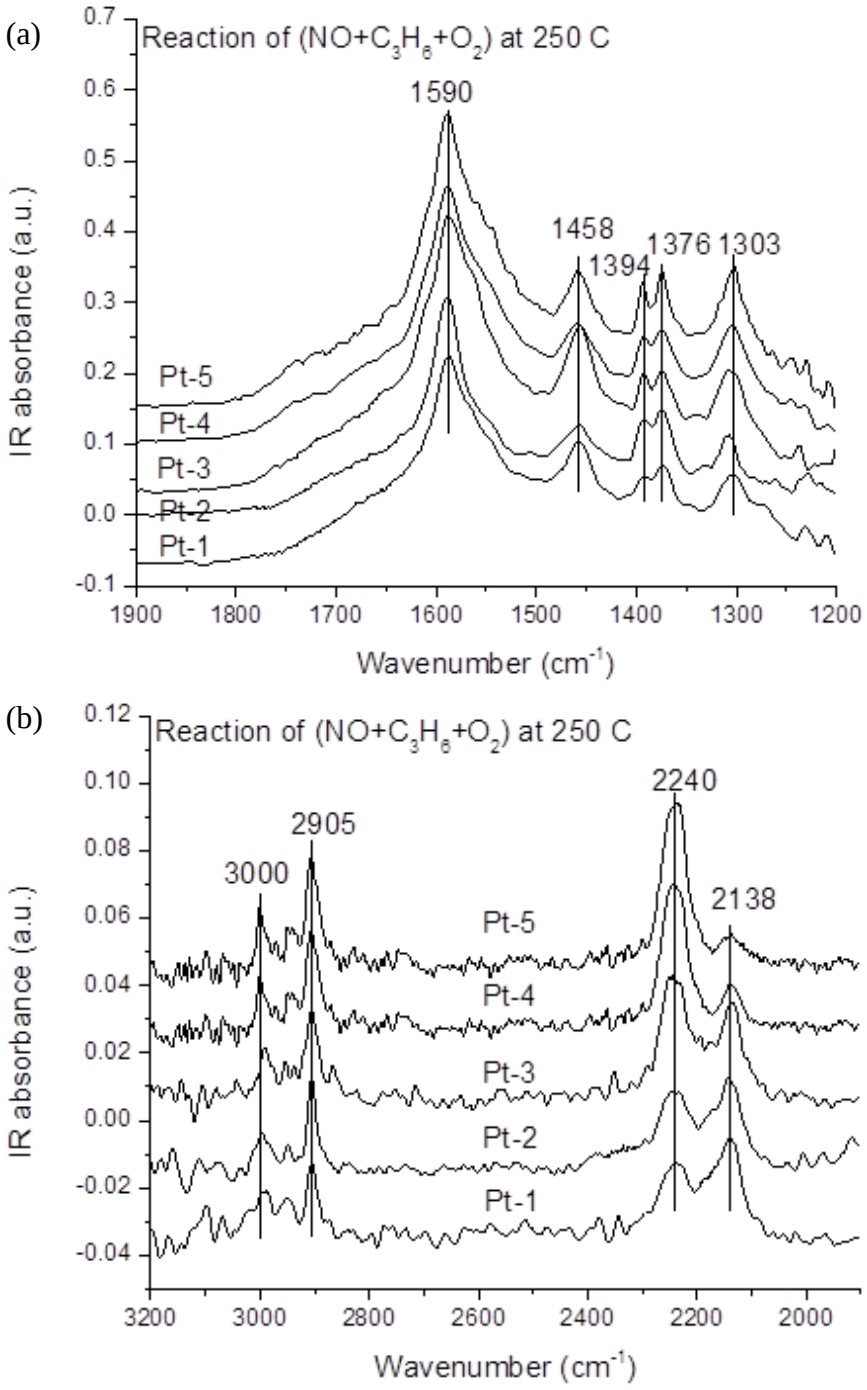

Figure 5.10: DRIFT spectra at steady state reaction of ($NO+C_3H_6+O_2$) on oxygen-pretreated Pt/Al_2O_3 catalysts at 250 °C, (a) IR region of nitrate and carbonate species, (b) IR region of hydrocarbon fragments, isocyanate and cyanide species

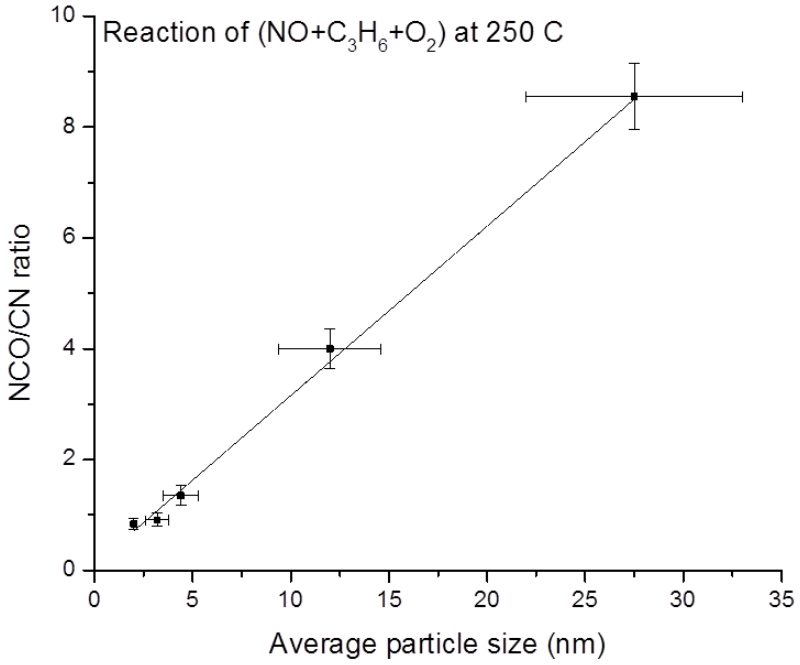

Figure 5.11: The calculated NCO/CN ratio as a function of particle size at steady-state reaction of ($NO+C_3H_6+O_2$) on Pt/Al_2O_3 catalysts

Based on the DRIFT spectra during the reaction of ($NO+C_3H_6+O_2$), it was noted that there was no obvious change for the band position and intensity of nitrate and carbonate species on different Pt catalysts, as shown in Figure 5.10 (a). However, the relative intensity of isocyanate (2240 cm^{-1}) compared to cyanide species (2138 cm^{-1}) clearly increased as the particle size increased, as shown in Figure 5.10 (b). Figure 5.11 shows the NCO/CN ratio based on the integral IR area. On catalyst Pt-1 with the smallest average particle size, the NCO/CN ratio was calculated as ~0.84 based on the integral IR peak area. While on catalyst Pt-5 with the largest average particle size, this ratio increased to 8.55. It was obvious that larger Pt particles significantly enhanced the formation of isocyanate species, which are the reactive intermediates for the HC-SCR of NO reaction. The hydrocarbon fragment species were also observed on all catalysts, as

shown in Figure 5.10 (b), and the intensity difference of these species on Pt catalysts was negligible.

Previously, it has been reported that these carbonyl species could prevent the adsorption of NO and further NO reduction [19-21, 226]. Apparently, under current reaction condition (2% O_2) the effect of carbonyl species was mitigated and the catalyst activity was not affected by these carbonyl species. Instead, the activity of Pt catalysts was mainly influenced by the particle size. Even though the surface area of the catalysts with large particle (Pt-4, Pt-5) were much lower than those with small particle (Pt-1, Pt-2 and Pt-3), the NO conversion was higher on the former ones. Furthermore, the TOFs of NO reduction on Pt catalysts with large particles were significantly higher than those with small particles (more than two orders of magnitude). More analysis of the effect of hydrocarbon fragments, specifically the activation of hydrocarbon species with oxygen, will be discussed later.

Indeed, based on systematic studies under different reaction conditions on Pt catalysts with the DRIFTS instrument, obvious difference of the surface species were observed due to the effect of hydrocarbon species. These observations and the contribution of oxygen species in the activation of hydrocarbons will be discussed during the reaction of ($NO+C_3H_6$) without oxygen on hydrogen-pretreated Pt catalysts and oxygen-pretreated Pt catalysts.

Figure 5.12 shows the DRIFT spectra of steady-state reaction experiments performed on hydrogen-pretreated Pt catalysts without oxygen in the feed gas mixture (2000 ppm NO, 2000 ppm C_3H_6 in He). The carbonate species (1300-1600 cm^{-1}) and

nitrite species (below 1300 cm^{-1}) were observed on all catalysts. From figure 5.12 (a), it is evident that the cyanide species was much more abundant than the isocyanate species on catalysts with smaller particles, including Pt-1, Pt-2 and Pt-3. In contrast, on Pt-4 and Pt-5 with much larger Pt particles, the isocyanate species was more pronounced than the cyanide species. More interestingly, there were more hydrocarbon fragments observed on the catalysts with small particle sizes, as shown in Figure 5.12 (a). In addition, in Figure 5.12 (b), the band around 1736 cm^{-1} corresponding to surface nitrosium (-NO) was observed on catalysts Pt-1, Pt-2 and Pt-3, but totally absent on catalyst Pt-4 and Pt-5. This demonstrates that, without oxygen, the isocyanate species cannot form easily on the catalyst surface, except in the case of catalyst Pt-4 and Pt-5 with large Pt particles. The NCO/CN ratio was calculated and presented in Figure 5.13. It is obvious that on catalysts with larger particles, there was a significant increase in the NCO/CN ratio. Especially, on catalysts Pt-4 and Pt-5, the NCO/CN was 1.5 and 3, respectively, indicating the formation of abundant isocyanate species on the catalyst surface.

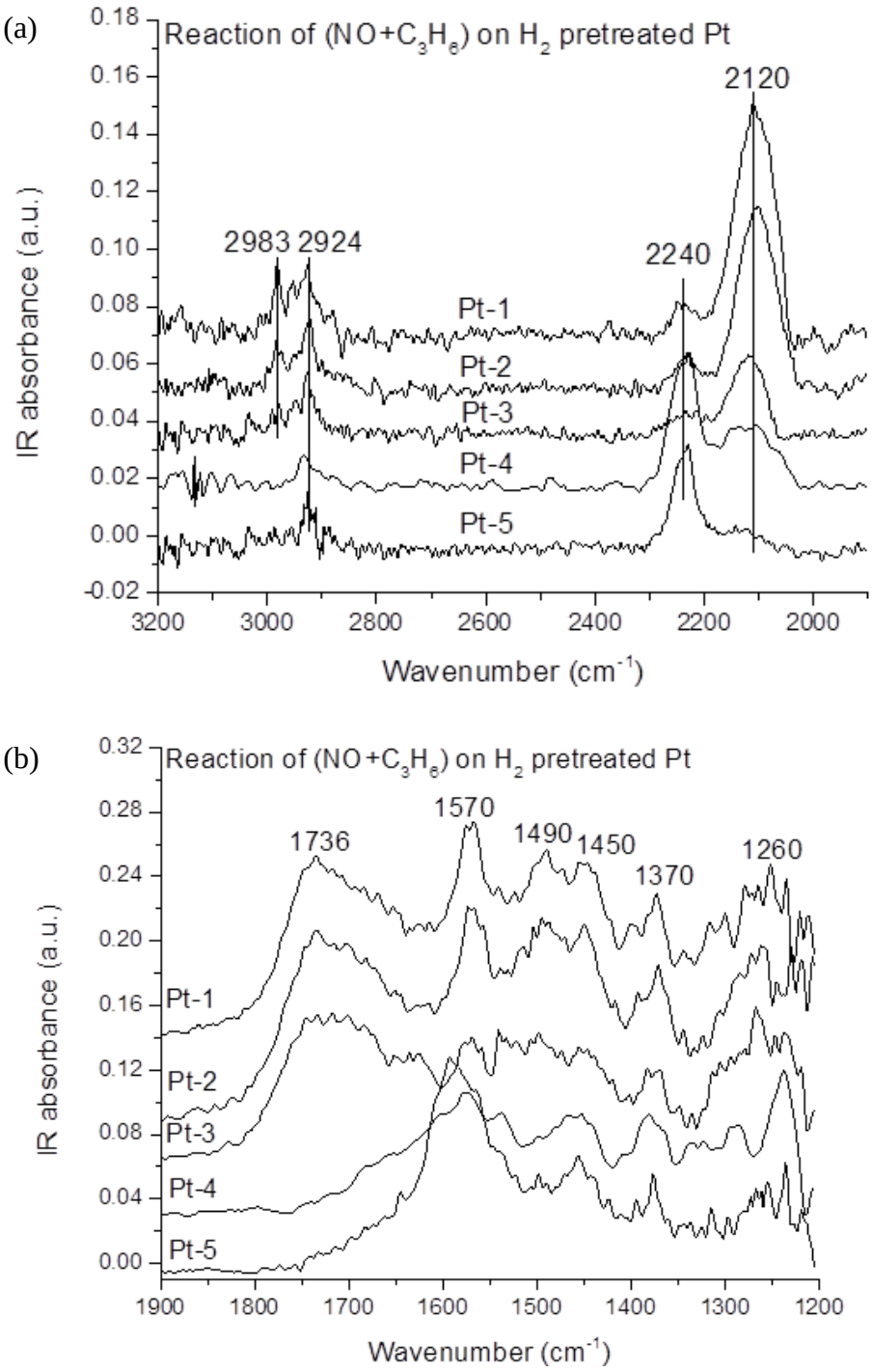

Figure 5.12: DRIFT spectra during ($NO+C_3H_6$) reaction on hydrogen-pretreated Pt/Al_2O_3 catalysts, (a) IR region of nitrate and carbonate species, (b) IR region of hydrocarbon fragments, isocyanate and cyanide species

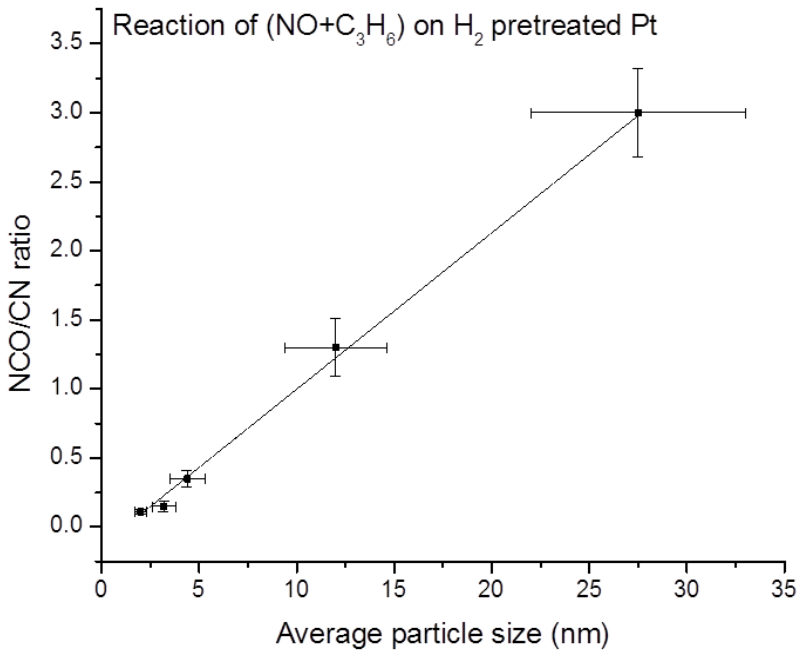

Figure 5.13: The calculated NCO/CN ratio as a function of particle size at steady-state reaction of ($NO+C_3H_6$) on hydrogen pretreated Pt/Al_2O_3 catalysts

It has been reported that catalyst surface can be poisoned by the hydrocarbon fragments or carboxylates, and that oxygen is in charge of "cleaning off" these species or "activating" them for further reaction [19-21, 226]. In Figure 5.12(a), relatively more hydrocarbon fragments (2900-3000 cm^{-1}) were observed on Pt catalysts with smaller particles, which could prevent NO dissociation. Indeed, NO turned to adsorb molecularly on the surface. So it is quite possible that lack of oxygen on the hydrogen-pretreated catalysts lead to surface poisoning by hydrocarbon fragments, resulting in less isocyanate formation. The reason we observed abundant isocyanate species on catalyst Pt-4 and Pt-5 is because NO dissociation occurred facilely on these catalysts, which could provide both O* for hydrocarbon activation and N* source for the formation of isocyanate species.

However, on catalysts with smaller Pt particles, NO could not dissociate easily enough to provide oxygen for hydrocarbon activation.

The results demonstrated here suggests that the formation of isocyanate species requires simultaneous hydrocarbon activation by oxygen (for $C_xH_yO_z^*$ formation) and NO dissociation (for N* formation) at the same time. On the other hand, the cyanide species were produced significantly on catalysts with smaller Pt particles. It is possible that the formation of the cyanide species requires neither NO dissociation or hydrocarbon activation [20]. For example, the cyanide species could be formed after the reaction between adsorbed NO* (or gas phase NO) and hydrocarbon fragments (e.g. C_xH_y).

A comparative study was performed on oxygen-pretreated Pt/Al_2O_3 catalysts without oxygen in the feed gas mixture (2000 ppm NO, 2000 ppm C_3H_6 in He), and the corresponding DRIFT spectra is shown in Figure 5.14. As expected, nitrate and carbonate species (see Figure 5.14 (a)) were observed on all catalysts. In contrast to the species on hydrogen-pretreated catalysts, distinct isocyanate species were observed on all oxygen-pretreated catalysts, including the catalysts with small Pt particles Pt-1, Pt-2 and Pt-3. The hydrocarbon species were observed on all catalysts without obvious different in the IR intensity. In addition, surface nitrosium was not observed on any catalyst.

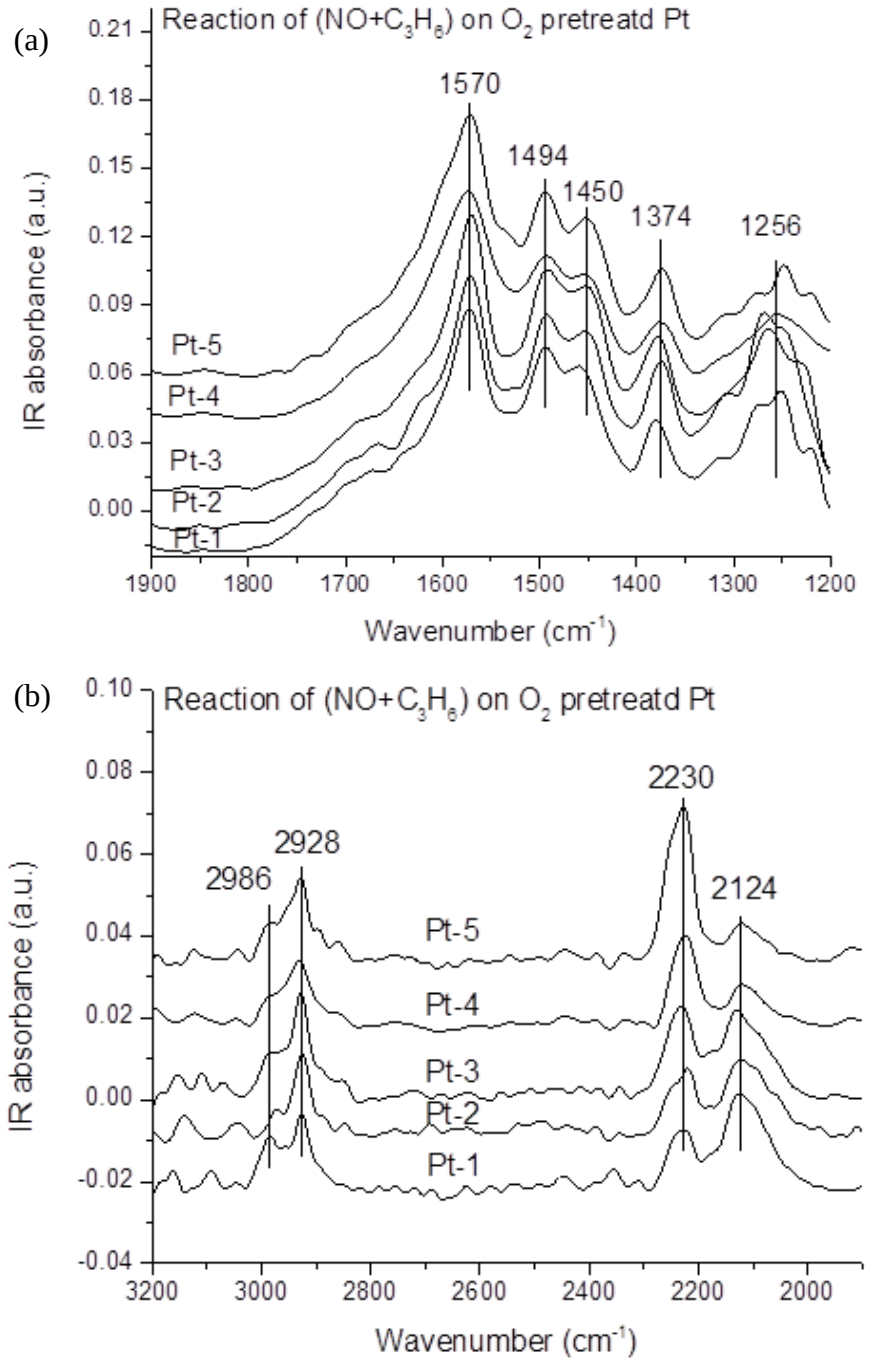

Figure 5.14: DRIFT spectra during ($NO+C_3H_6$) reaction on oxygen-pretreated Pt/Al_2O_3 catalysts, (a) IR region of nitrate and carbonate species, (b) IR region of hydrocarbon fragments, isocyanate and cyanide species

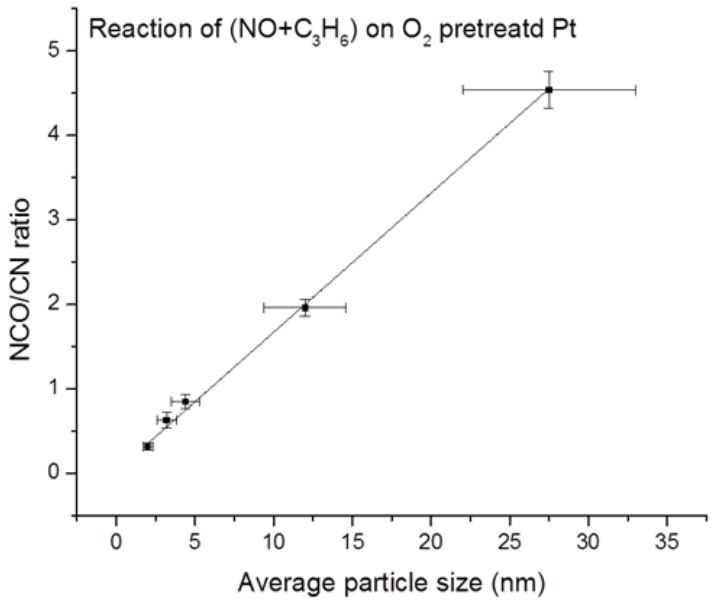

Figure 5.15: The calculated NCO/CN ratio as a function of particle size at steady-state reaction of ($NO+C_3H_6$) on oxygen-pretreated Pt/Al_2O_3 catalysts

Apparently, the surface oxygen on oxygen-pretreated catalysts enhanced the formation of isocyanate species during the ($NO+C_3H_6$) reaction. As pointed out before, this could be due to the activation of surface hydrocarbons species with oxygen favoring isocyanate formation. There are two possible reasons for the absence of nitrosium species. The first possibility is that NO molecules dissociated on Pt and then reacted with the activated hydrocarbons forming isocyanate species, which was clearly observed from the IR spectra in Figure 5.14(b). The second possibility is that NO facilely reacted with the abundant surface oxygen forming nitrogen dioxides, which could be easily reduced back to NO molecules in the presence of propene [12]. Since there were abundant isocyanate species appeared in the IR spectra, it is more likely that NO molecules dissociated on Pt surface after the surface oxygen was consumed during the hydrocarbon activation. Again, catalyst Pt-5 with the largest particles produced significant amount of isocyanane species and showed the highest NCO/CN ratio among all catalysts. As shown in Figure 5.15, the

NCO/CN ratio increased form 0.32 for catalyst Pt-1 to 4.54 for catalyst Pt-5. In comparison to the NCO/CN ratio on the corresponding catalysts with hydrogen pretreatment, the NCO/CN ratio was always bigger on the catalysts with oxygen pretreatment.

Figure 5.16 shows the comparison of NCO/CN ratio during the reaction of NO and propene with or without oxygen on different catalysts after different pretreatments (oxygen-pretreated vs. hydrogen-pretreated). Regardless of the reaction conditions and catalyst pretreatment, a relative higher NCO/CN ratio was always observed on the catalysts with larger particles, especially on Pt-5 with the largest Pt particles. Higher NCO/CN ratio during the reaction and better activity for NO reduction on the catalysts with larger particles can be attributed to their superior activity toward NO dissociation, which is proposed to be an important step for the formation of isocyanate. In addition, the DRIFTS measurements during the reaction ($NO+C_3H_6$) without oxygen on hydrogen-pretreated catalysts clearly showed that the surface oxygen also played an important role during the formation of isocyanate species, probably due to its active role in the hydrocarbon activation process.

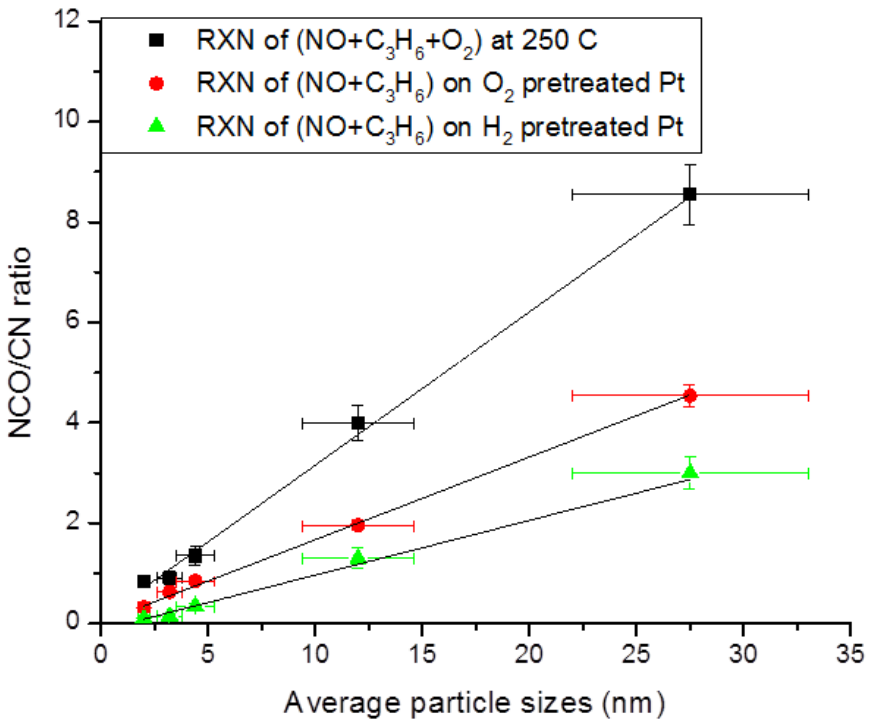

Figure 5.16: Comparison of NCO/CN ratio at steady state with different reaction conditions and different catalyst pretreatments

5.3.4 Proposed reaction mechanism for NO reduction on Pt/Al_2O_3

Based on the analysis above, it is proposed that the reduction of NO with propene in excess oxygen proceeds as following steps:

1) $O_2 \rightarrow 2O^*$

2) $NO \rightarrow NO^*$

3) $C_3H_6 \rightarrow C_xH_y^*$

4) $NO^* \rightarrow N^* + O^*$

5) $C_xH_y^* + O^* \rightarrow C_xH_yO_z^*$

6) $NO^*/NO + C_xH_y^* \rightarrow CN^* + H_2O$

7) $N^* + C_xH_yO_z^* \rightarrow NCO^* + H_2O$

8) $C_xH_y/C_xH_yO_z^* + O^*/O_2 \rightarrow CO_2 + H_2O$

9) $NCO^* + O^*/O_2/NOx \rightarrow N_2 + N_2O + CO_2$

As shown in the steps, NO molecules are reduced to nitrogen via the formation of isocyanates species, which requires two important steps: (4) NO dissociation on Pt surface, and (5) activation of hydrocarbon species by oxygen. Apparently, activated hydrocarbons play a really important role in the whole process, which agrees well with the mechanism proposed by Bamwenda et al [19] and Captain et al [20, 21]. Without the activation by oxygen, the hydrocarbon fragments could cover the catalysts surface and prevent NO adsorption and reduction. In the meantime, the dissociation of NO molecules is another factor that affects the catalyst activity. This step not only can provide the N* source for isocyanate species formation, but also can provide active O* atoms for hydrocarbon activation. It is believed that catalysts with larger particles have better activity for NO dissociation and can facilitate isocyanate formation, resulting in higher efficiency for NO reduction.

5.4 Conclusions and summary

It has been shown that Pt particle size played an important role in the HC-SCR reaction. Higher NO conversions and TOFs were obtained on the catalysts with larger Pt particles, on which a relative higher NCO/CN ratio was observed during in situ spectroscopic measurements under reaction conditions. It is proposed that larger Pt particles, which have more terrace sites than corner or edge sites, have better activity for NO dissociation, which can enhance the formation of reactive intermediates such as isocyanate during the reaction. In addition, the activation of the hydrocarbon species by oxygen is believed to be a crucial step in the formation of the isocyanate species, thus can influence the catalyst activity for NO reduction.

CHAPTER 6

Conclusions and Outlook

In this thesis, in situ IR spectroscopic techniques, including PM-IRAS and DRIFTS, were applied to study the surface reactions related to the auto-exhaust emissions with the combination of mass spectroscopy. It was demonstrated that valuable information of the species existing on catalysts surface under reaction conditions could be obtained using this approach. PM-IRAS has been shown to be highly effective for detecting adsorbed surface species at elevated pressure conditions, and it can be applied to bridge the "pressure gap" between surface science and realistic industrial catalysis by performing experiments from UHV to elevated pressures conditions. In addition, the thin film supported nanoparticle catalyst which is suitable for IR spectroscopic studies was successfully made via wet deposition method, and it could be used to perform systematic studies in the PM-IRAS system to bridge the "materials gap". Furthermore, the influence of metal particle size on the surface species formed on the catalyst surface and the catalyst activity during reaction conditions was determined using in situ DRIFT spectroscopy combined with mass spectroscopy.

For CO adsorption and dissociation on Pt surface, detailed investigations were performed in the PM-IRAS system from UHV to elevated pressures. It was shown that

the saturation coverage of CO on the Pt(100) was larger than 0.85 at the pressure range of 10^{-4}-300 Torr, which is much greater than the reported saturation surface coverage (0.75) under high vacuum conditions (10^{-6} Torr). As the sample temperature increased, a red shift of the C-O stretching band was observed due to weaker dipole coupling of fewer molecules on the surface. Heating and cooling cycles performed at pressures above 2 Torr revealed a cyclic adsorption behavior of CO due to the carbon deposition on the surface. A series of CO adsorption experiments were carried out on the sample after it was annealed at temperatures above 775 K in 100 Torr CO. Both TPD and PM-IRA spectra collected after 100 L CO exposure on the annealed sample indicated that the amount of adsorbed CO molecule decreased with increasing annealing time. Interestingly, the C-O stretching band was found to remain at the same vibrational frequency during these experiments, due to the formation close-packed CO islands on different annealed samples with similar local interactions. Dipole coupling simulations were performed to simulate the effect of adsorbate geometries on the absorbance band positions. It was clear that vibrational frequency of CO increased linearly with the surface coverage in the random adsorption geometry. For the island geometry though, the vibrational frequency showed a steep jump up to 10% coverage and then increased slowly as the surface approached saturation. The agreement between the experimental data and the island geometry simulation results indicated that CO molecules adsorbed as islands with similar local interactions on the annealed sample with different carbon depositions. These findings can provide an insight into carbon deposition effects on the activity of Pt catalysts operating at high temperatures in a CO environment. In the future, different surface reaction studies can be performed in a similar way in the PM-IRAS system to

understand the surface chemistries on different metal surfaces: such as NO reduction with hydrocarbons on Pt surface and CO_2 hydrogenation on Ni surface.

For the model catalyst synthesis, it has been demonstrated that thin film supported catalyst Ru/Al_2O_3 can be made via wet deposition of mono-dispersed Ru nanoparticles on alumina thin film support. Thermal oxidation of aluminum substrate at 900 K could achieve γ-alumina thin film, which is applicable as a model catalyst support. On the other hand, it is challenging to make crystalline alumina thin film via magnetron sputter deposition method. Mono-dispersed Ru nanoparticles were successfully synthesized via colloid method using PVP as the protective agent, which can be removed from Ru nanoparticles with acetone/ethanol cleaning plus UVO treatment. Finally, wet deposition of Ru nanoparticles on alumina thin film support lead to the formation of model supported Ru/Al_2O_3 catalyst, which could potentially be used to study the particle size effect or metal-support interaction at a molecular level. Based on the preliminary test, this model catalyst is suitable for PM-IRAS measurements, and more experiments will be required to carry out in DRIFTS instrument before the sample is loaded into the PM-IRAS system. For future work, it will be beneficial to run more experiments to find the optimal deposition condition for the synthesis of γ-Al_2O_3 in the magnetron sputter system. An alternative method is to use a single crystal substrate that can stand high temperature annealing to make α-Al_2O_3. The colloidal method can be applied to synthesize other metal nanoparticles, such as Pt and Pd. Thus the wet deposition method can be used to prepare various model supported catalysts, and systematic reaction studies over these model catalysts in the PM-IRAS system will provide the opportunity to bridge the "pressure gap" and "material gap" at the same time.

Based on in situ DRIFTS studies over Pt/Al_2O_3 catalysts at different reaction conditions, the effect of Pt particles size on the formation of surface species and catalyst activity was revealed. Higher NO conversions with much higher TOFs were obtained on the catalysts with larger Pt particles, on which a relative higher NCO/CN ratio was observed during in situ spectroscopic measurements at reaction conditions. From the systematic studies on Pt catalysts with different pretreatments, it was proposed that better activity on catalysts with larger Pt particles were attributed to the more abundant terrace sites rather than corner or edge sites on larger Pt particles. These terrace sites have better activity for NO dissociation, thus can enhance the formation of reactive intermediates such as isocyanate during the reaction. In addition, it was found that the activation of the hydrocarbon species by oxygen was a crucial step toward the formation of the isocyanate species, thus could influence the catalyst activity for NO reduction. For HC-SCR over Pt catalyst, future research should focus on exploring the elemental reaction steps over a model catalyst surface at a molecular level with well-controlled parameters. Several questions remain to be answered: specifically, how does the surface species formed on the catalyst surface step by step? Is there any interaction between the metal particles and the support? By performing systematic in situ spectroscopic investigation on model catalysts, such as Pt single crystal and thin film supported Pt nanoparticles, further understanding of this reaction becomes possible.

REFERENCES

[1] J.M. Thomas, W.J. Thomas, Principles and Practice of Heterogeneous Catalysis, VCH, Weiheim, 1997.
[2] A. Fritz, V. Pitchon, Applied Catalysis B: Environmental 13 (1997) 1-25.
[3] M.V. Twigg, Applied Catalysis B: Environmental 70 (2007) 2-15.
[4] S. Roy, M.S. Hegde, G. Madras, Applied Energy 86 (2009) 2283-2297.
[5] V.I. Pârvulescu, P. Grange, B. Delmon, Catalysis Today 46 (1998) 233-316.
[6] M.D. Amiridis, T. Zhang, R.J. Farrauto, Applied Catalysis B: Environmental 10 (1996) 203-227.
[7] R. Burch, P.J. Millington, A.P. Walker, Applied Catalysis B: Environmental 4 (1994) 65-94.
[8] R. Burch, J.P. Breen, F.C. Meunier, Applied Catalysis B: Environmental 39 (2002) 283-303.
[9] R. Burch, P.J. Millington, Catalysis Today 26 (1995) 185-206.
[10] R. Burch, D. Ottery, Applied Catalysis B: Environmental 13 (1997) 105-111.
[11] R. Burch, P.J. Millington, Catalysis Today 29 (1996) 37-42.
[12] J.H. Lee, H.H. Kung, Catalysis Letters 51 (1998) 1-4.
[13] I.V. Yentekakis, M. Konsolakis, R.M. Lambert, N. Macleod, L. Nalbantian, Applied Catalysis B-Environmental 22 (1999) 123-133.
[14] M. Konsolakis, I.V. Yentekakis, Journal of Catalysis 198 (2001) 142-150.
[15] M. Konsolakis, I.V. Yentekakis, Applied Catalysis B-Environmental 29 (2001) 103-113.
[16] T. Tanaka, T. Okuhara, M. Misono, Applied Catalysis B: Environmental 4 (1994) L1-L9.
[17] E. Joubert, X. Courtois, P. Marecot, C. Canaff, D. Duprez, Journal of Catalysis 243 (2006) 252-262.
[18] M. Konsolakis, I.V. Yentekakis, Topics in Catalysis 56 (2013) 165-171.
[19] G.R. Bamwenda, A. Ogata, A. Obuchi, J. Oi, K. Mizuno, J. Skrzypek, Applied Catalysis B: Environmental 6 (1995) 311-323.
[20] D.K. Captain, C. Mihut, J.A. Dumesic, M.D. Amiridis, Catalysis Letters 83 (2002) 109-114.
[21] D.K. Captain, M.D. Amiridis, Journal of Catalysis 184 (1999) 377-389.
[22] T. Engel, G. Ertl, in: H.P. D.D. Eley, B.W. Paul (Eds.), Advances in Catalysis, Academic Press, 1979, pp. 1-78.
[23] G. Ertl, Catalysis, Science and Technology, Springer, Berlin, 1983.
[24] D.W. Goodman, C.H.F. Peden, M.S. Chen, Surface Science 601 (2007) L124-L126.
[25] F. Gao, D.W. Goodman, Physical Chemistry Chemical Physics 14 (2012) 6688-6697.
[26] X. Su, P.S. Cremer, Y.R. Shen, G.A. Somorjai, Journal of the American Chemical Society 119 (1997) 3994-4000.
[27] D. Stacchiola, H. Molero, W.T. Tysoe, Catalysis Today 65 (2001) 3-11.
[28] K. Honkala, A. Hellman, I.N. Remediakis, A. Logadottir, A. Carlsson, S. Dahl, C.H. Christensen, J.K. Nørskov, Science 307 (2005) 555-558.
[29] J. Shi, Chemical Reviews 113 (2013) 2139-2181.

[30] A. Satsuma, K. Osaki, M. Yanagihara, J. Ohyama, K. Shimizu, Applied Catalysis B: Environmental 132–133 (2013) 511-518.
[31] T.A. Jachimowski, J. Lauterbach, Review of Scientific Instruments 69 (1998) 2757-2761.
[32] D.F. Ogletree, H. Bluhm, G. Lebedev, C.S. Fadley, Z. Hussain, M. Salmeron, Review of Scientific Instruments 73 (2002) 3872-3877.
[33] A. Ludviksson, J. Yoshihara, C.T. Campbell, Review of Scientific Instruments 66 (1995) 4370-4374.
[34] E. Laegsgaard, L. Osterlund, P. Thostrup, P.B. Rasmussen, I. Stensgaard, F. Besenbacher, Review of Scientific Instruments 72 (2001) 3537-3542.
[35] A.L. Cabrera, N.D. Spencer, E. Kozak, P.W. Davies, G.A. Somorjai, Review of Scientific Instruments 53 (1982) 1888-1893.
[36] G.A. Somorjai, G. Rupprechter, The Journal of Physical Chemistry B 103 (1999) 1623-1638.
[37] D.W. Goodman, Surface Science 299–300 (1994) 837-848.
[38] E. Gillet, S. Channakhone, V. Matolin, Journal of Catalysis 97 (1986) 437-447.
[39] E.W. Kuipers, C. Laszlo, W. Wieldraaijer, Catalysis Letters 17 (1993) 71-79.
[40] A. Timénez-González, D. Schmeisser, Journal of Catalysis 130 (1991) 332-346.
[41] I. Stará, V. Matolín, Surface Science 313 (1994) 99-106.
[42] T. Lear, R. Marshall, E.K. Gibson, T. Schutt, T.M. Klapotke, G. Rupprechter, H.-J. Freund, J.M. Winfield, D. Lennon, Physical Chemistry Chemical Physics 7 (2005) 565-567.
[43] H.-F. Wang, W.E. Kaden, R. Dowler, M. Sterrer, H.-J. Freund, Physical Chemistry Chemical Physics 14 (2012) 11525-11533.
[44] G.A. Somorjai, C. Aliaga, Langmuir 26 (2010) 16190-16203.
[45] H.J. Borg, L.C.A. van den Oetelaar, L.J. van Ijzendoorn, J.W. Niemantsverdriet, Journal of Vacuum Science & Technology A 10 (1992) 2737-2741.
[46] P.L.J. Gunter, J.W. Niemantsverdriet, F.H. Ribeiro, G.A. Somorjai, Catalysis Reviews 39 (1997) 77-168.
[47] P.C. Thüne, J.W. Niemantsverdriet, Surface Science 603 (2009) 1756-1762.
[48] C.R. Henry, Surface Science Reports 31 (1998) 231-325.
[49] C.T. Campbell, Surface Science Reports 27 (1997) 1-111.
[50] P. Bernard, K. Peters, J. Alvarez, S. Ferrer, Review of Scientific Instruments 70 (1999) 1478-1480.
[51] P.L. Hansen, J.B. Wagner, S. Helveg, J.R. Rostrup-Nielsen, B.S. Clausen, H. Topsøe, Science 295 (2002) 2053-2055.
[52] S. Helveg, C. Lopez-Cartes, J. Sehested, P.L. Hansen, B.S. Clausen, J.R. Rostrup-Nielsen, F. Abild-Pedersen, J.K. Norskov, Nature 427 (2004) 426-429.
[53] G. Somorjai, X. Su, K. McCrea, K. Rider, Topics in Catalysis 8 (1999) 23-34.
[54] G. Rupprechter, T. Dellwig, H. Unterhalt, H.J. Freund, Topics in Catalysis 15 (2001) 19-26.
[55] R. Günther, W. Christian, Journal of Physics: Condensed Matter 20 (2008) 184019.
[56] T. Buffeteau, B. Desbat, D. Blaudez, J.M. Turlet, Appl. Spectrosc. 54 (2000) 1646-1650.
[57] B.L. Frey, R.M. Corn, S.C. Weibel, Handbook of Vibrational Spectroscopy, John Wiley & Sons, Ltd, 2006.
[58] H. Oosterbeek, Physical Chemistry Chemical Physics 9 (2007) 3570-3576.
[59] E. Ozensoy, B.K. Min, A.K. Santra, D.W. Goodman, Journal of Physical Chemistry B 108 (2004) 4351-4357.
[60] G. Rupprechter, Advances in Catalysis 51 (2007) 133-263.
[61] J. Saccani, T. Buffeteau, B. Desbat, D. Blaudez, Appl. Spectrosc. 57 (2003) 1260-1265.
[62] J.E. Bedenbaugh, Model Catalysts for High-pressure Spectroscopic Investigations, Chemical Engineering, University of Delaware, Fall 2009.
[63] T.P. Lele, T.D. Pletcher, J. Lauterbach, Aiche Journal 47 (2001) 1418-1424.

[64] B.D. Cullity, S.R. Stock, Elements of X-ray Diffraction, 3rd ed., Prentice Hall, Upper Saddle River, NJ, 2001.
[65] P.R. Grittiths, J.A. de Haseth, Fourier transform infrared spectroscopy, Second ed., John Wiley & Sons, Ltd, 2006.
[66] W.D. Perkins, Journal of Chemical Education 63 (1986) A5.
[67] W.D. Perkins, Journal of Chemical Education 64 (1987) A269.
[68] G.A. Somorjai, Introduction to Surface Chemistry and Catalysis, John Wiley & Sons, Inc., 1994.
[69] F.M. Hoffmann, Surface Science Reports 3 (1983) 107-192.
[70] F. Zaera, H. Hoffmann, P.R. Griffiths, Journal of Electron Spectroscopy and Related Phenomena 54 (1990) 705-715.
[71] F.M. Hoffmann, M.D. Weisel, Journal of Vacuum Science & Technology A 11 (1993) 1957-1963.
[72] H. Hoffmann, P.R. Griffiths, F. Zaera, Surface Science 262 (1992) 141-150.
[73] C. Weilach, S.M. Kozlov, H.H. Holzapfel, K. Föttinger, K.M. Neyman, G. Rupprechter, The Journal of Physical Chemistry C 116 (2012) 18768-18778.
[74] F. Zaera, Chemical Society Reviews 43 (2014) 7624-7663.
[75] F. Gao, Y. Wang, D.W. Goodman, The Journal of Physical Chemistry C 114 (2010) 4036-4043.
[76] G.A. Beitel, C.P.M. deGroot, H. Oosterbeek, J.H. Wilson, Journal of Physical Chemistry B 101 (1997) 4035-4043.
[77] B.J. Barner, M.J. Green, E.I. Saez, R.M. Corn, Analytical Chemistry 63 (1991) 55-60.
[78] T. Buffeteau, B. Desbat, J.M. Turlet, Applied Spectroscopy 45 (1991) 380-389.
[79] Q. Li, R. He, J.-A. Gao, J.O. Jensen, N.J. Bjerrum, Journal of The Electrochemical Society 150 (2003) A1599-A1605.
[80] S.F. Yin, B.Q. Xu, X.P. Zhou, C.T. Au, Applied Catalysis A: General 277 (2004) 1-9.
[81] M. Ojeda, R. Nabar, A.U. Nilekar, A. Ishikawa, M. Mavrikakis, E. Iglesia, Journal of Catalysis 272 (2010) 287-297.
[82] S. Shetty, R.A. van Santen, Catalysis Today 171 (2011) 168-173.
[83] Q. Zhang, K. Cheng, J. Kang, W. Deng, Y. Wang, ChemSusChem 7 (2014) 1251-1264.
[84] R.A. van Santen, I.M. Ciobica, E. van Steen, M.M. Ghouri, in: B.C. Gates, H. Knozinger (Eds.), Advances in Catalysis, Vol 54, 2011, pp. 127-187.
[85] Z.P. Liu, P. Hu, Journal of the American Chemical Society 124 (2002) 11568-11569.
[86] H. Schulz, Applied Catalysis A: General 186 (1999) 3-12.
[87] B. Hammer, Y. Morikawa, J. Nørskov, Physical Review Letters 76 (1996) 2141-2144.
[88] T. Fink, R. Imbihl, G. Ertl, Journal of Chemical Physics 91 (1989) 5002-5010.
[89] R. Imbihl, S. Ladas, G. Ertl, Faceting in an oscillatory surface reaction: the catalytic CO oxidation on Pt(110), 34th National Symposium of the American Vacuum Society, 2-6 Nov. 1987, 3 ed., USA, 1988, pp. 877-878.
[90] R.J. Behm, P.A. Thiel, P.R. Norton, G. Ertl, Journal of Chemical Physics 78 (1983) 7437-7447.
[91] P.A. Thiel, R.J. Behm, P.R. Norton, G. Ertl, Journal of Chemical Physics 78 (1983) 7448-7458.
[92] R. Imbihl, M.P. Cox, G. Ertl, Journal of Chemical Physics 84 (1986) 3519-3534.
[93] R. Imbihl, M.P. Cox, G. Ertl, H. Muller, W. Brenig, Journal of Chemical Physics 83 (1985) 1578-1587.
[94] M. Sander, R. Imbihl, G. Ertl, Journal of Chemical Physics 95 (1991) 6162-6170.
[95] T. Fink, J.P. Dath, R. Imbihl, G. Ertl, Surface Science 251-52 (1991) 985-989.
[96] M. Eiswirth, P. Moller, K. Wetzl, R. Imbihl, G. Ertl, Journal of Chemical Physics 90 (1989) 510-521.

[97] S.J. Lombardo, M. Slinko, T. Fink, T. Loeher, H.H. Madden, F. Esch, R. Imbihl, G. Ertl, Surface Science 260-70 (1992) 481-487.
[98] M. Sander, M.R. Bassett, R. Imbihl, G. Ertl, Vacuum 41 (1990) 272-274.
[99] J. Lauterbach, R.W. Boyle, M. Schick, W.J. Mitchell, B. Meng, W.H. Weinberg, Surface Science 350 (1996) 32-44.
[100] P.T. Fanson, W.N. Delgass, J. Lauterbach, Journal of Catalysis 204 (2001) 35-52.
[101] G.P. Van Der Laan, A.A.C.M. Beenackers, Catalysis Reviews 41 (1999) 255-318.
[102] H.-J. Freund, G. Meijer, M. Scheffler, R. Schlögl, M. Wolf, Angewandte Chemie International Edition 50 (2011) 10064-10094.
[103] R.W. McCabe, L.D. Schmidt, Surface Science 66 (1977) 101-124.
[104] G. Brodén, G. Pirug, H.P. Bonzel, Surface Science 72 (1978) 45-52.
[105] A. Crossley, D.A. King, Surface Science 95 (1980) 131-155.
[106] M.A. Barteau, E.I. Ko, R.J. Madix, Surface Science 102 (1981) 99-117.
[107] R. Martin, P. Gardner, A.M. Bradshaw, Surface Science 342 (1995) 69-84.
[108] F. Tao, S. Dag, L.-W. Wang, Z. Liu, D.R. Butcher, H. Bluhm, M. Salmeron, G.A. Somorjai, Science 327 (2010) 850-853.
[109] K. McCrea, J.S. Parker, P.L. Chen, G. Somorjai, Surface Science 494 (2001) 238-250.
[110] C. Minot, Catalysis Today 89 (2004) 357-362.
[111] K. Baron, D.W. Blakely, G.A. Somorjai, Surface Science 41 (1974) 45-66.
[112] T. Zecho, A. Horn, J. Biener, J. Küppers, Surface Science 397 (1998) 108-115.
[113] X.Q.D. Li, T. Radojicic, R. Vanselow, Surface Science 225 (1990) L29-L32.
[114] B. Lang, Surface Science 53 (1975) 317-329.
[115] M. Mundschau, R. Vanselow, Surface Science 160 (1985) 23-36.
[116] T.A. Land, T. Michely, R.J. Behm, J.C. Hemminger, G. Comsa, Surface Science 264 (1992) 261-270.
[117] D.E. Starr, E.M. Pazhetnov, A.I. Stadnichenko, A.I. Boronin, S.K. Shaikhutdinov, Surface Science 600 (2006) 2688-2695.
[118] L. Nilsson, M. Andersen, J. Bjerre, R. Balog, B. Hammer, L. Hornekær, I. Stensgaard, Surface Science 606 (2012) 464-469.
[119] F.M. Hoffmann, The Journal of Chemical Physics 90 (1989) 2816-2823.
[120] F.M. Hoffmann, J.L. Robbins, Journal of Electron Spectroscopy and Related Phenomena 45 (1987) 421-428.
[121] B.N.J. Persson, R. Ryberg, Physical Review B 32 (1985) 3586-3596.
[122] M. Trenary, K.J. Uram, F. Bozso, J.T. Yates Jr, Surface Science 146 (1984) 269-280.
[123] H. Aizawa, S. Tsuneyuki, Surface Science 399 (1998) L364-L370.
[124] G. Blyholder, The Journal of Physical Chemistry 68 (1964) 2772-2777.
[125] D. Curulla, A. Clotet, J.M. Ricart, Surface Science 460 (2000) 101-111.
[126] G.D. Mahan, A.A. Lucas, The Journal of Chemical Physics 68 (1978) 1344-1348.
[127] M. Scheffler, Surface Science 81 (1979) 562-570.
[128] W.F. Banholzer, R.I. Masel, Surface Science 137 (1984) 339-360.
[129] C.M. Kim, C.W. Yi, D.W. Goodman, The Journal of Physical Chemistry B 109 (2005) 1891-1895.
[130] K. Christmann, Introduction to surface physical chemistry, Steinkopff Verlag Darmstadt Springer-Verlag New York, 1991.
[131] D.W. Goodman, C.H.F. Peden, M.S. Chen, Surface Science 601 (2007) 5663-5665.
[132] K.R. McCrea, J.S. Parker, G.A. Somorjai, Journal of Physical Chemistry B 106 (2002) 10854-10863.
[133] M. Bäumer, H.-J. Freund, Progress in Surface Science 61 (1999) 127-198.
[134] C.R. Henry, H. Poppa, Thin Solid Films 189 (1990) 303-312.
[135] S. Giorgio, H. Graoui, C. Chapon, C.R. Henry, Materials Science and Engineering: A 229 (1997) 169-173.

[136] M.-C. Wu, J.S. Corneille, C.A. Estrada, J.-W. He, D. Wayne Goodman, Chemical Physics Letters 182 (1991) 472-478.
[137] C.M. Truong, M.C. Wu, D.W. Goodman, The Journal of Chemical Physics 97 (1992) 9447-9453.
[138] P.J. Chen, M.L. Colaianni, J.T. Yates, Physical Review B 41 (1990) 8025-8032.
[139] P.J. Chen, D.W. Goodman, Surface Science 312 (1994) L767-L773.
[140] C. Xu, D.W. Goodman, Chemical Physics Letters 263 (1996) 13-18.
[141] J.W. He, X. Xu, J.S. Corneille, D.W. Goodman, Surface Science 279 (1992) 119-126.
[142] X. Xu, D.W. Goodman, Applied Physics Letters 61 (1992) 774-776.
[143] F. Rohr, K. Wirth, J. Libuda, D. Cappus, M. Bäumer, H.J. Freund, Surface Science 315 (1994) L977-L982.
[144] G. Ceballos, Z. Song, J.I. Pascual, H.P. Rust, H. Conrad, M. Bäumer, H.J. Freund, Chemical Physics Letters 359 (2002) 41-47.
[145] R.M. Jaeger, H. Kuhlenbeck, H.J. Freund, M. Wuttig, W. Hoffmann, R. Franchy, H. Ibach, Surface Science 259 (1991) 235-252.
[146] J.G. Chen, J.E. Crowell, J.T. Yates Jr, Surface Science 187 (1987) 243-264.
[147] D.N. Belton, Y.M. Sun, J.M. White, Journal of Catalysis 102 (1986) 338-347.
[148] C.A. Leighton, A.J. Swift, J.C. Vickerman, Surface Science 253 (1991) 220-232.
[149] X.D. Peng, M.A. Barteau, Applied Surface Science 44 (1990) 87-95.
[150] P.B. Smith, S.L. Bernasek, J. Schwartz, G.S. McNulty, Journal of the American Chemical Society 108 (1986) 5654-5655.
[151] D.N. Belton, S.J. Schmieg, Applied Surface Science 32 (1988) 173-192.
[152] M. Shirai, K. Asakura, Y. Iwasawa, Catalysis Letters 15 (1992) 247-254.
[153] M. Shirai, T. Inoue, H. Onishi, K. Asakura, Y. Iwasawa, Journal of Catalysis 145 (1994) 159-165.
[154] S.K. Purnell, X. Xu, D.W. Goodman, B.C. Gates, The Journal of Physical Chemistry 98 (1994) 4076-4082.
[155] J. Nickl, R. Schlögl, A. Baiker, H. Knözinger, G. Ertl, Catalysis Letters 3 (1989) 379-387.
[156] H.J. Borg, L.C.A. van den Oetelaar, J.W. Niemantsverdriet, Catalysis Letters 17 (1993) 81-95.
[157] R.M. van Hardeveld, P.L.J. Gunter, L.J. van Ijzendoorn, W. Wieldraaijer, E.W. Kuipers, J.W. Niemantsverdriet, Applied Surface Science 84 (1995) 339-346.
[158] E.W. Kuipers, C. Doornkamp, W. Wieldraaijer, R.E. van den Berg, Chemistry of Materials 5 (1993) 1367-1369.
[159] H. Song, F. Kim, S. Connor, G.A. Somorjai, P. Yang, The Journal of Physical Chemistry B 109 (2005) 188-193.
[160] E. Stathatos, P. Lianos, F. Del Monte, D. Levy, D. Tsiourvas, Langmuir 13 (1997) 4295-4300.
[161] J.M. Rickard, L. Genovese, A. Moata, S. Nitsche, Journal of Catalysis 121 (1990) 141-152.
[162] H. Poppa, D. Fargues, L. Kieken, D. Neiman, R. Savoy, Vacuum 41 (1990) 485-488.
[163] J.G. Chen, J.E. Crowell, J.T. Yates Jr, Surface Science 185 (1987) 373-393.
[164] D.N. Belton, S.J. Schmieg, Journal of Vacuum Science & Technology A 6 (1988) 859-860.
[165] K. Wolter, O. Seiferth, H. Kuhlenbeck, M. Bäumer, H.J. Freund, Surface Science 399 (1998) 190-198.
[166] M. Heemeier, S. Stempel, S.K. Shaikhutdinov, J. Libuda, M. Bäumer, R.J. Oldman, S.D. Jackson, H.J. Freund, Surface Science 523 (2003) 103-110.
[167] C. Weilach, C. Spiel, K. Föttinger, G. Rupprechter, Surface Science 605 (2011) 1503-1509.
[168] H.H. Madden, D.W. Goodman, Surface Science 150 (1985) 39-46.

[169] V. Matolin, E. Gillet, S. Channakhone, Journal of Catalysis 97 (1986) 448-455.
[170] B. Ealet, M.H. Elyakhloufi, E. Gillet, M. Ricci, Thin Solid Films 250 (1994) 92-100.
[171] L.H. Dubois, P.K. Hansma, G.A. Somorjai, Applications of Surface Science 6 (1980) 173-184.
[172] J. Sotola, Z. Knor, Journal of Catalysis 145 (1994) 501-507.
[173] E.I. Altman, R.J. Gorte, Surface Science 172 (1986) 71-80.
[174] S.D. Bischke, D.W. Goodman, J.L. Falconer, Surface Science 150 (1985) 351-357.
[175] T. Wang, C. Lee, L.D. Schmidt, Surface Science 163 (1985) 181-197.
[176] T.F. Hayden, J.A. Dumesic, Journal of Catalysis 103 (1987) 366-384.
[177] Y.F. Chu, E. Ruckenstein, Journal of Catalysis 55 (1978) 281-298.
[178] H. Glassl, K. Hayek, R. Kramer, Journal of Catalysis 68 (1981) 397-405.
[179] R. Kramer, H. Zuegg, Journal of Catalysis 80 (1983) 446-456.
[180] B. Tesche, E. Alizo Delgado, H. Knözinger, Catalysis Letters 10 (1991) 171-180.
[181] R. Cremer, K. Reichert, G. Erkens, D. Neuschutz, High Temp. Mater. Process 14 (2010) 321-332.
[182] R. Cremer, M. Witthaut, D. Neuschütz, G. Erkens, T. Leyendecker, M. Feldhege, Surface and Coatings Technology 120–121 (1999) 213-218.
[183] P.J. Kelly, R.D. Arnell, Vacuum 56 (2000) 159-172.
[184] G. Fuchs, D. Neiman, H. Poppa, Thin Solid Films 207 (1992) 65-70.
[185] V. Matolín, I. Matolínová, M. Václavů, I. Khalakhan, M. Vorokhta, R. Fiala, I. Piš, Z. Sofer, J. Poltierová-Vejpravová, T. Mori, V. Potin, H. Yoshikawa, S. Ueda, K. Kobayashi, Langmuir 26 (2010) 12824-12831.
[186] V. Matolín, V. Johánek, I. Stará, N. Tsud, K. Veltruská, Surface Science 507–510 (2002) 803-807.
[187] I.M. Ciobica, A.W. Kleyn, R.A. Van Santen, The Journal of Physical Chemistry B 107 (2002) 164-172.
[188] A. Hellman, K. Honkala, I.N. Remediakis, Á. Logadóttir, A. Carlsson, S. Dahl, C.H. Christensen, J.K. Nørskov, Surface Science 603 (2009) 1731-1739.
[189] D.E. Starr, H. Bluhm, Surface Science 608 (2013) 241-248.
[190] A. Hellman, K. Honkala, I.N. Remediakis, Á. Logadóttir, A. Carlsson, S. Dahl, C.H. Christensen, J.K. Nørskov, Surface Science 600 (2006) 4264-4268.
[191] S.B. Vendelbo, M. Johansson, J.H. Nielsen, I. Chorkendorff, Physical Chemistry Chemical Physics 13 (2011) 4486-4493.
[192] G. Viau, R. Brayner, L. Poul, N. Chakroune, E. Lacaze, F. Fiévet-Vincent, F. Fiévet, Chemistry of Materials 15 (2003) 486-494.
[193] M. Zawadzki, J. Okal, Materials Research Bulletin 43 (2008) 3111-3121.
[194] A. Miyazaki, I. Balint, K.-i. Aika, Y. Nakano, Journal of Catalysis 204 (2001) 364-371.
[195] Y. Chen, K.Y. Liew, J. Li, Materials Letters 62 (2008) 1018-1021.
[196] J. Shen, X. Yin, D. Karpuzov, N. Semagina, Catalysis Science & Technology 3 (2013) 208-221.
[197] C.-J. Jia, F. Schuth, Physical Chemistry Chemical Physics 13 (2011) 2457-2487.
[198] L.D. Pachón, G. Rothenberg, Applied Organometallic Chemistry 22 (2008) 288-299.
[199] J.A. Lopez-Sanchez, N. Dimitratos, C. Hammond, G.L. Brett, L. Kesavan, S. White, P. Miedziak, R. Tiruvalam, R.L. Jenkins, A.F. Carley, D. Knight, C.J. Kiely, G.J. Hutchings, Nat Chem 3 (2011) 551-556.
[200] Y. Borodko, S.E. Habas, M. Koebel, P. Yang, H. Frei, G.A. Somorjai, The Journal of Physical Chemistry B 110 (2006) 23052-23059.
[201] R. Cremer, K. Reichert, D. Neuschütz, G. Erkens, T. Leyendecker, Surface and Coatings Technology 163–164 (2003) 157-163.
[202] A. Khanna, D.G. Bhat, Surface and Coatings Technology 201 (2006) 168-173.

[203] M. Sridharan, M. Sillassen, J. Bøttiger, J. Chevallier, H. Birkedal, Surface and Coatings Technology 202 (2007) 920-924.
[204] J. Musil, J. Blažek, P. Zeman, Š. Prokšová, M. Šašek, R. Čerstvý, Applied Surface Science 257 (2010) 1058-1062.
[205] I.N. Reddy, V.R. Reddy, N. Sridhara, V.S. Rao, M. Bhattacharya, P. Bandyopadhyay, S. Basavaraja, A.K. Mukhopadhyay, A.K. Sharma, A. Dey, Ceramics International 40 (2014) 9571-9582.
[206] C. Collins, J. Lucas, T.L. Buchanan, M. Kopczyk, A. Kayani, P.E. Gannon, M.C. Deibert, R.J. Smith, D.S. Choi, V.I. Gorokhovsky, Surface and Coatings Technology 201 (2006) 4467-4470.
[207] S. Khaddar-Zine, A. Ghorbel, C. Naccache, Journal of Molecular Catalysis A: Chemical 150 (1999) 223-231.
[208] P.A. Beck, P.R. Sperry, Journal of Applied Physics 21 (1950) 150-152.
[209] A. Aminzadeh, H. Sarikhani-fard, Spectrochimica Acta Part A: Molecular and Biomolecular Spectroscopy 55 (1999) 1421-1425.
[210] D. Thi My Dung, L. Thi Thu Tuyet, F.-B. Eric, D. Mau Chien, Advances in Natural Sciences: Nanoscience and Nanotechnology 3 (2012) 035004.
[211] F. Tuinstra, J.L. Koenig, The Journal of Chemical Physics 53 (1970) 1126-1130.
[212] M. Iwamoto, H. Furukawa, Y. Mine, F. Uemura, S.-i. Mikuriya, S. Kagawa, Journal of the Chemical Society, Chemical Communications (1986) 1272-1273.
[213] S.i. Matsumoto, Catalysis Today 90 (2004) 183-190.
[214] P. Vernoux, A.Y. Leinekugel-Le-Cocq, F. Gaillard, Journal of Catalysis 219 (2003) 247-257.
[215] I.V. Yentekakis, A. Palermo, M.S. Tikhov, N.C. Filkin, R.M. Lambert, in: N. Kruse, A. Frennet, J.M. Bastin (Eds.), Catalysis and Automotive Pollution Control Iv, 1998, pp. 255-264.
[216] V. Pitchon, A. Fritz, Journal of Catalysis 186 (1999) 64-74.
[217] K. Otto, H.C. Yao, Journal of Catalysis 66 (1980) 229-236.
[218] E. Xue, K. Seshan, J.R.H. Ross, Applied Catalysis B: Environmental 11 (1996) 65-79.
[219] P. Denton, A. Giroir-Fendler, H. Praliaud, M. Primet, Journal of Catalysis 189 (2000) 410-420.
[220] J.M. García-Cortés, J. Pérez-Ramírez, J.N. Rouzaud, A.R. Vaccaro, M.J. Illán-Gómez, C. Salinas-Martínez de Lecea, Journal of Catalysis 218 (2003) 111-122.
[221] W.F. Banholzer, J.M. Gohndrone, G.H. Hatzikos, J.F. Lang, R.I. Masel, Y.O. Park, K. Stolt, Journal of Vacuum Science & Technology a-Vacuum Surfaces and Films 3 (1985) 1559-1560.
[222] Q. Ge, M. Neurock, Journal of the American Chemical Society 126 (2004) 1551-1559.
[223] J.M. Gohndrone, R.I. Masel, Surface Science 209 (1989) 44-56.
[224] K.-i. Shimizu, H. Kawabata, A. Satsuma, T. Hattori, The Journal of Physical Chemistry B 103 (1999) 5240-5245.
[225] W. Schießer, H. Vinek, A. Jentys, Applied Catalysis B: Environmental 33 (2001) 263-274.
[226] M. Sasaki, H. Hamada, Y. Kintaichi, T. Ito, Catalysis Letters 15 (1992) 297-304.